

# Investigation of Defects on MgO Films grown on Ag(001) - A Combined Dynamic Force and Scanning Tunneling Microscopy Study

Eingereicht an der  
Fakultät II - Mathematik und Naturwissenschaften  
der  
Technischen Universität Berlin

zur Erlangung des akademischen Grades  
doctor rerum naturalium  
(Dr. rer. nat.)  
im Fach Physik

Genehmigte Dissertation von

Herrn Dipl.-Phys. Thomas König  
geboren am 18.12.1980 in Münster

Promotionsausschuss:

Vorsitzender: Prof. Dr. Michael Lehmann

Gutachter: Prof. Dr. Hans-Joachim Freund

Gutachter: Prof. Dr. Christian Thomsen

Gutachter: Prof. Dr. Gianfranco Pacchioni

Tag der wissenschaftlichen Aussprache: 1. Juli 2010

Berlin 2010

D 83

## II

Diese Dissertation wurde von September 2006 bis März 2010 in der Abteilung Chemische Physik am Fritz-Haber-Institut der Max-Planck-Gesellschaft unter der Anleitung von Herrn Professor Dr. Hans-Joachim Freund angefertigt.

Für meine Familie.



# Zusammenfassung

In dieser Arbeit wurden mittels hochauflösender Rasterkraft- und Rastertunnelmikroskopie verschiedene Eigenschaften des Modellsystems MgO/Ag(001) untersucht. Der Vorteil des verwendeten Setups ist die Integration der beiden Mikroskoptypen in einen Sensor. Magnesiumoxid auf Silber (001) ist ein weit verbreitetes Modellsystem aufgrund seiner einfachen Struktur und des guten epitaktischen Wachstums. Modellsysteme haben im Bereich der heterogenen Katalyse eine große Bedeutung, da sie es erlauben, Strukturen sowohl geometrischer als auch elektronischer Art sowie chemische Reaktionen unter wohldefinierten Bedingungen stattfinden zu lassen und zu untersuchen. Somit lässt sich der Parameterraum für katalytische Reaktionen reduzieren, denn häufig ist er unter industriellen Bedingungen zu groß, um ein detailliertes Verständnis zu erlangen.

Vor diesem Hintergrund wurde der Einfluss der MgO-Dünnschichten auf die Austrittsarbeit des Ag(001) untersucht. Die Austrittsarbeit ist ein wichtiger Parameter, um Elektronenladungen zwischen dem Silber und möglichen Adsorbaten auf dem MgO-Film auszutauschen. Der Ladungstransfer kann das chemische Verhalten eines Adsorbates signifikant beeinflussen.

Insbesondere wurden Sauerstofffehlstellen in der MgO-Oberfläche untersucht. Diese Sauerstofffehlstellen können eine unterschiedliche Anzahl von Elektronen fangen und somit verschiedene Ladungszustände einnehmen. Die Identifikation der Ladungszustände der Defekte gelang erstmalig mit einem Rasterkraftmikroskop. Da das Rasterkraftmikroskop sensitiv auf interatomare Kräfte reagiert, wurde auch die Wechselwirkung eines Metallclusters (Messspitze) mit den Sauerstofffehlstellen untersucht. An der Defektposition wird eine hohe attraktive Wechselwirkung registriert. Daraus lässt sich schließen, dass Defektstellen bevorzugte Adsorptionstellen für Metalladsorbate sind und daher präferierte Positionen für chemische Reaktionen bilden.

Den Messungen liegt eine detaillierte Betrachtung der elektrostatischen Spitze-Probe-Wechselwirkung zugrunde, die daher in dieser Arbeit ausführlich in ihrem Parameterraum untersucht wurde.



# Summary

In this work, different properties of the MgO/Ag(001) model system have been investigated by high resolution dynamic force and scanning tunneling microscopy. The advantage of the setup employed is the implementation of both microscopy types in one sensor. Magnesium oxide on silver (001) is a widely used model system due to its simple structure and well defined epitaxial growth. Model systems play an important role in heterogeneous catalysis, since they allow investigations of structural and electronic factors, as well as the chemical reactivity under well defined conditions. Therefore, the parameter space for catalytic reactions, which is usually too large in industrial applications, can be reduced and thus knowledge can be gained.

On this basis, the influence of MgO thin films on the Ag(001) work function has been investigated. The work function is an important parameter for electron exchange between the silver support and adsorbates on top of the MgO thin films. The charge transfer can have a significant impact on the chemical reactivity of the adsorbate.

Furthermore, oxygen vacancies on the MgO surface have been investigated. Oxygen vacancies can trap up to two electrons, and can therefore have different charge states. The identification of the charge states has been performed by dynamic force microscopy for the first time. Since the dynamic force microscope is sensitive to interatomic forces, the interaction of a metal cluster (tip) with oxygen vacancies has been investigated. At the defects' positions, a high attractive interaction was found. The defects are therefore preferred adsorption sites for metal adsorbates and are thus sites for chemical reactions.

The measurements are based on a detailed investigation of the electrostatic tip-sample interaction, which has been analyzed extensively in its parameter space.



# Contents

<b>Zusammenfassung</b>	<b>V</b>
<b>Summary</b>	<b>VII</b>
<b>List of Figures</b>	<b>XI</b>
<b>List of Tables</b>	<b>XIII</b>
<b>1 Introduction and Motivation</b>	<b>1</b>
<b>2 Methods and Experimental Setup</b>	<b>3</b>
2.1 Overview . . . . .	3
2.2 Setup: Dual Mode DFM/STM . . . . .	4
2.3 Dynamic Force Microscopy . . . . .	8
2.3.1 Frequency Modulation Dynamic Force Microscopy . . . . .	8
2.3.2 Potentials and Forces in DFM . . . . .	9
2.3.3 Theoretical Approach to FM-DFM . . . . .	19
2.3.4 Calculating the Force between Tip and Sample . . . . .	22
2.4 Scanning Tunneling Microscopy . . . . .	25
2.4.1 STM Operation Principle . . . . .	25
2.4.2 Theoretical Approach . . . . .	25
2.4.3 Contrast Formation in High Resolution STM . . . . .	27
2.4.4 Scanning Tunneling Spectroscopy . . . . .	30
2.4.5 Field Emission Resonances . . . . .	31
<b>3 MgO on Ag(001)</b>	<b>35</b>
3.1 General MgO Aspects . . . . .	35
3.2 MgO Properties . . . . .	36
3.3 Characteristics of MgO Thin Films on Ag(001) . . . . .	40
3.4 Defects in MgO . . . . .	43
3.5 Preparation of MgO Thin Films on Ag(001) . . . . .	55

<b>4</b>	<b>Ag(001) Work Function Shift Induced by the MgO film</b>	<b>57</b>
4.1	Motivation . . . . .	57
4.2	Preliminary Considerations . . . . .	58
4.3	Measurement Procedure . . . . .	61
4.4	Results and Discussion . . . . .	62
4.5	Conclusion . . . . .	69
<b>5</b>	<b>Identification and Characterization of Color Centers</b>	<b>71</b>
5.1	Motivation . . . . .	71
5.2	Results and Discussion . . . . .	72
5.3	Conclusion . . . . .	78
<b>6</b>	<b>Attractive Interaction on <math>F^0</math> Color Centers</b>	<b>79</b>
6.1	Motivation . . . . .	79
6.2	Results and Discussion . . . . .	79
6.3	Conclusion . . . . .	84
<b>7</b>	<b>Conclusions and Outlook</b>	<b>85</b>
	<b>Bibliography</b>	<b>87</b>
<b>A</b>	<b>Abbreviations</b>	<b>109</b>
<b>B</b>	<b>Publications and Conferences</b>	<b>111</b>

# List of Figures

1.1	Schematic of a model catalyst. . . . .	2
2.1	Cryostat for low temperature (5 K) investigations. . . . .	5
2.2	Walker unit of the microscope. . . . .	6
2.3	Tuning fork sensor carrier. . . . .	7
2.4	Setup of a dual mode FM-DFM/STM. . . . .	9
2.5	Capacities between tip and sample. . . . .	12
2.6	Contact potential formation. . . . .	13
2.7	Electrostatic force in parameter space. . . . .	14
2.8	Comparison of interaction potentials. . . . .	18
2.9	Test of FM-DFM theory. . . . .	24
2.10	Schematic picture of the tunneling junction. . . . .	27
2.11	Potential energy scheme of the tunneling process. . . . .	28
2.12	Tip-sample energy levels for FER. . . . .	32
2.13	Example of field emission resonances. . . . .	33
3.1	Phase diagram of MgO. . . . .	36
3.2	Ball-structure model of the MgO lattice. . . . .	37
3.3	MgO band structure. . . . .	39
3.4	Tasker nomenclature for surfaces. . . . .	40
3.5	Growth model of MgO on Ag(001). . . . .	41
3.6	Different surface sites on MgO. . . . .	45
3.7	Explanation of ionization and relaxation energies. . . . .	48
3.8	Lattice relaxation effects at vacancies. . . . .	49
3.9	Energy level of $F^0$ and $F^+$ centers. . . . .	52
3.10	EELS of defects. . . . .	54
3.11	LEED images of Ag(001) and 3 ML MgO/Ag(001). . . . .	55
4.1	Contributions to the work function shift. . . . .	59
4.2	STM images of different MgO film thicknesses. . . . .	63
4.3	CPD measurements on Ag(001) and 3 ML MgO/Ag(001). . . . .	64

4.4	Tunneling current vs distance relation. . . . .	65
4.5	Field emission resonance data . . . . .	66
4.6	Work function shift vs $z$ displacement. . . . .	67
5.1	FM-DFM images of defects. . . . .	72
5.2	STM images at different voltages of point defects on MgO. . .	73
5.3	FM-DFM results of color centers. . . . .	74
5.4	Charge density distributions of defects. . . . .	76
5.5	STS results of color centers. . . . .	77
6.1	Constant height linescans across an $F^0$ defect. . . . .	81
6.2	Metal cluster defect interaction. . . . .	83

# List of Tables

3.1	MgO layer distances with respect to the Ag(001) surface. . . .	42
3.2	Ionization, relaxation energies and electron affinities. . . . .	47
3.3	Formation energies and lattice relaxations for defects. . . . .	51
3.4	Assignment of EELS features. . . . .	53
4.1	Important properties of MgO on Ag(001). . . . .	60
4.2	Work function shift data. . . . .	65

# Chapter 1

## Introduction and Motivation

These days heterogeneous catalysis plays an important role since more than 90 % of all goods undergo a catalytic process during their production. Furthermore the green energy sector as well as the conventional industry rely on heterogeneous catalysis, e.g. for hydrogen extraction or exhaustgas cleaning. Although the importance of heterogeneous catalysis is well known, a detailed understanding of the reaction steps and pathways is often lacking. In most cases this is a tribute to the high complexity of the chemical reactions since the parameter space determining the turnover is too large and too involved. Thus empirical values are often used in chemical industry. To reduce the complexity model systems have been designed. Model systems are often highly dispersed metal species on an inert substrate. The inert substrate is commonly grown on top of a metal support and is usually only a few monolayers thick (see figure 1.1). Widely used substrates are silica, alumina, titania and magnesium oxide. Such thin film designs provide the opportunity to use surface sensitive techniques since charging effects are prevented by the metal support. Moreover, thin film systems can exhibit properties in their own right [1] mediated by the metal support. Chemical reactions may therefore differ from reactions on bulk oxides. However, surface properties such as the optical, electronic and transport properties as well as the chemical activity crucially depend on surface defects [2]. This is in particular true for MgO. The pristine MgO surface is quite inert, but a defect rich MgO surface shows a complex surface chemistry. On MgO oxygen vacancies, so-called color centers, are frequently discussed since they can trap up to two electrons. Most chemical reactions depend on electron-electron interaction or electron exchange, thus color centers are in focus of today's research. Therefore, to understand many surface properties and chemical reactions on the surface means to detect and analyze in detail for example the local positions of the defects on the surface, their electronic signatures, local potentials and

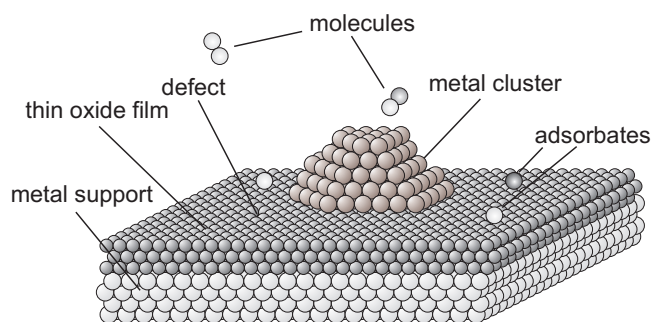


Figure 1.1: Schematic of a model catalyst. A thin oxide film with a dispersed metal cluster on top grown onto a metal support.

interaction behavior with adsorbates.

The influence of the color centers on catalytic reactions has not been proven unambiguously since the defects might be deactivated in the presence of oxygen, i.e. the vacancy is filled by an oxygen atom and therefore not accessible for another reaction cycle. At high temperatures the vacancy might be regenerated. Thus, whether color centers are catalytically relevant or not will be shown in future. To analyze single point defects integrating techniques are insufficient and surface sensitive techniques with a high local resolution are a prerequisite. Dynamic force microscopy (DFM) also known as atomic force microscopy as well as scanning tunneling microscopy (STM) provide high local resolution in real space. Within this study a special setup, a combined DFM/STM, employing the same tip on the same surface area has been used to gain complementary information. To ensure high thermal stability and well defined operation conditions the measurements have been performed in ultrahigh vacuum at 5 K.

In addition, it was unclear whether DFM is able to detect the charge state of single point defects. This possibility would make the analysis of point defects on bulk oxide insulators possible since the DFM in contrast to the STM is not limited to conducting samples or thin oxide films supported on metal surfaces. In the second chapter an overview about the experimental setup and the theoretical background of DFM and STM are presented. In chapter 3 the MgO system is discussed in detail and a comparison between bulk MgO and thin MgO films supported on Ag(001) is made. In chapter 4 the work function shift of Ag(001) induced by MgO and its impact on adsorbates is discussed. Furthermore this chapter is a basis for the high resolution measurements presented in chapter 5, where individual color centers are analyzed by DFM and STM. In chapter 6 the interaction of metal clusters with color centers is discussed.

# Chapter 2

## Methods and Experimental Setup

### 2.1 Overview

The invention of the scanning tunneling microscope (STM) by Gerd Binnig and Heinrich Rohrer in 1982 [3] opened the way into new eras in many different research fields. The scientific impact of STM was widely recognized, and only four years after the invention, Gerd Binnig and Heinrich Rohrer were awarded the Nobel Prize in physics 1986 [4]. The fundamental physical effect utilized by the STM is the quantum mechanical tunneling effect. The STM offers real space resolution based on the local density of states (LDOS) [5] and thus also for the LDOS related topography. The STM can be operated in a number of spectroscopy modes revealing insights into different sample properties. Scanning tunneling spectroscopy (STS) gives detailed insights into the local density of states [5–7]. Moreover, fascinating quantum mechanical effects [7–10] such as quantum corrals [11, 12] have been observed and studied. Photon emission spectroscopy performed with a photon STM provides information about plasmon resonances of e.g. metal clusters [13, 14], inelastic tunneling spectroscopy (IETS) reveals vibrational modes of single adsorbed molecules [15–18]. Furthermore, molecular switches have been designed that can be switched by the STM in a reproducible manner [19]. With a magnetic STM tip, spin polarized tunneling can be performed and magnetic sample properties investigated [20–22].

Accompanied by the question of forces acting between the STM tip and the sample again Gerd Binnig together with Calvin F. Quate and Christoph Gerber developed the atomic force microscope (AFM) [23] in 1986. The deflection of the cantilever due to the tip-sample interaction forces had been de-

tected by a scanning tunneling microscope. With the AFM the breakthrough for interatomic force measurements on many different materials, such as insulators, semi-conductors and conductors, has been achieved since AFM is not limited to conducting surfaces. In the following years the AFM gained high attention and the technique made a strong development. In the first AFMs the static bending of the cantilever was used as a feedback signal. These days the cantilever is usually oscillating and the amplitude is used as a feedback signal (AM-mode) or the shift of the resonance frequency (FM-mode) [24]. The latter mode is sometimes called non-contact atomic force microscopy (NC-AFM) mode. Here it is referred to as dynamic mode and thus DFM (dynamic force microscope) will be used as an acronym instead of AFM. Both the amplitude and the frequency shift are usually detected by a laser beam reflected at the back side of a coated cantilever hitting a four quadrant photo diode.

The DFM today has a strong place in many different research fields ranging from biology to chemistry and physics. Living cells have been investigated in liquid environments [25–28], membrane structures have been mapped [29, 30] and their ion conductivity has been measured. The strong progress in the development of DFM setups manifests itself in many scientific results and the will to push them further. In 1995 Franz Giessibl [31] was the first to obtain atomic resolution with a DFM. The measurements were accomplished on the  $7\times 7$  reconstructed Si(111) surface. In the following years atomic resolution has been observed on metal [32, 33] and insulator [34–36] surfaces.

In 2005 Sugimoto et al. [37] manipulated single atoms at room temperature. In 1998 Franz Giessibl used an oscillating piezo electric tuning fork as a force sensor with one prong glued to a holder [38], this setup is often called qplus sensor. To the oscillating prong he attached a metal tip. The advantage of this setup is its operation without a laser and its detection equipment, since the oscillation of the tip results in a voltage due to the piezo electric properties of the tuning fork. This voltage can be directly amplified and processed. In the following sections the setup used in this paper will be presented followed by an introduction into dynamic force and scanning tunneling microscopy.

## 2.2 Setup: Dual Mode DFM/STM

The setup employed is optimized for surface investigation on the atomic scale with spatial resolution of a few picometers. Picometer resolution can be achieved with both non-contact atomic force microscopy, also known as

frequency modulation dynamic force microscopy (FM-DFM), and scanning tunneling microscopy. For stability reasons of tip and sample, reduced piezo creep and hysteresis, reduction of thermal drift as well as low noise levels the setup operates in ultrahigh vacuum (UHV) and at 5 K. Due to the high stability, atomic resolution on conductors [33] as well as insulators [35] can be achieved.

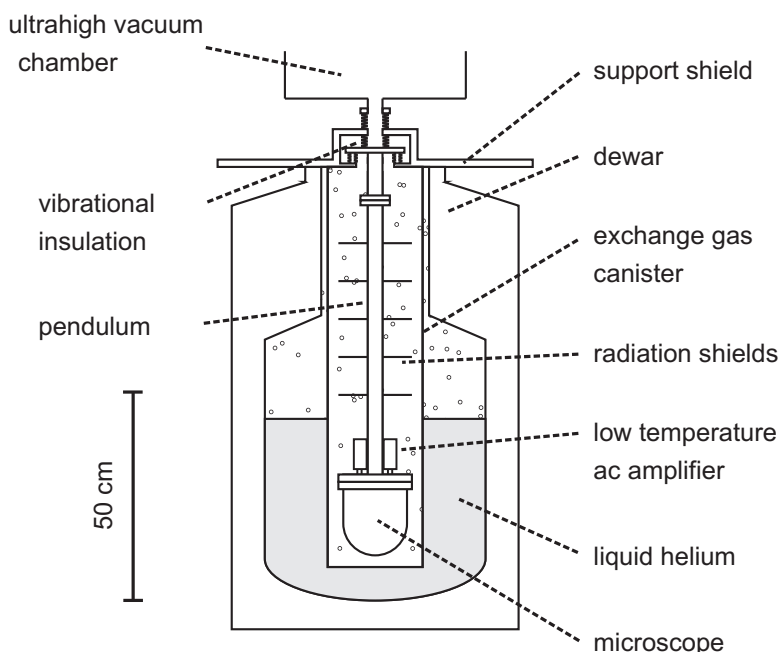


Figure 2.1: Cryostat for low temperature (5 K) investigations. The microscope is situated at the end of a so-called pendulum. The pendulum is inside an exchange gas canister filled with helium gas at a pressure of about 10 mbar. The helium gas causes the thermal coupling between the liquid helium inside the dewar and the microscope. At the same time it decouples vibrations from the evaporating liquid helium.

Beside investigations on the surface structure, site specific spectroscopy measurements can be performed [35]. The UHV chamber is situated inside a sound insulating cabin on a wooden frame which is based on an active vibrational damping system. The background pressure inside the UHV chamber is below  $4 \times 10^{-10}$  mbar. Both main- and preparation chamber are pumped separately by a turbo molecular and an ion getter pump. The preparation of thin MgO films is done in the preparation chamber (see section 3.5). The microscope stage is cooled down via a bath cryostat which is filled with liquid helium (see figure 2.1). Within the cryostat a so-called exchange gas canister

is situated. The exchange gas canister is filled with helium to a pressure of about 10 mbar. The helium gas establishes the thermal coupling between the microscope stage inside the UHV chamber and the liquid helium inside the bath cryostat. In addition, the vibrations caused by the evaporating helium inside the bath cryostat are decoupled from the microscope.

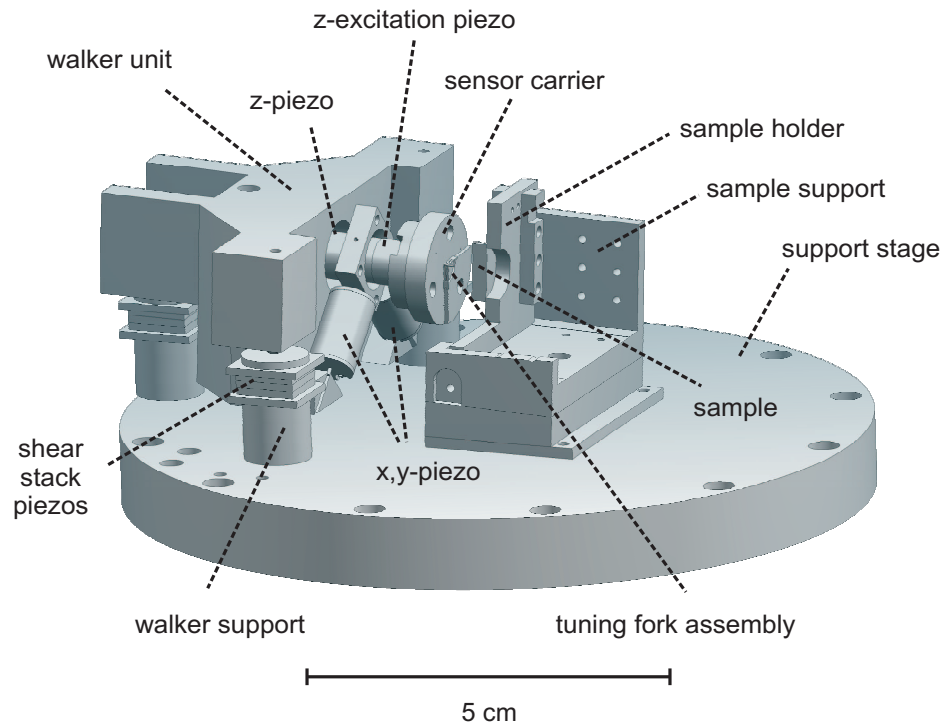


Figure 2.2: The walker unit is a tripod situated on shear stack piezos for the rough approach. The  $x$ ,  $y$  and  $z$  piezos are used during the scan process. The tuning fork is located opposite the sample (only half of the sample is drawn to keep the view free to the sensor carrier). Further explanations are given in the text.

The microscope stage is shown in figure 2.2. The dual mode DFM/STM sensor (figure 2.3) is situated on a tripod stage (walker) opposite the sample. The walker is responsible for the rough approach. The rough approach is facilitated by the shear stack piezos. If the tip-sample distance is in the range of interatomic forces or in tunneling regime the approach is switched off and the scan is performed by the  $x$ ,  $y$  and  $z$  piezos. The additional excitation piezo excites the tuning fork at its resonance frequency. The tuning fork sensor is presented in figure 2.3. Tuning forks are made of quartz ( $\text{SiO}_2$ ) and are therefore piezo electric devices. Tuning forks are commercially used in watches as time keeping elements. Commercial tuning forks have a resonance

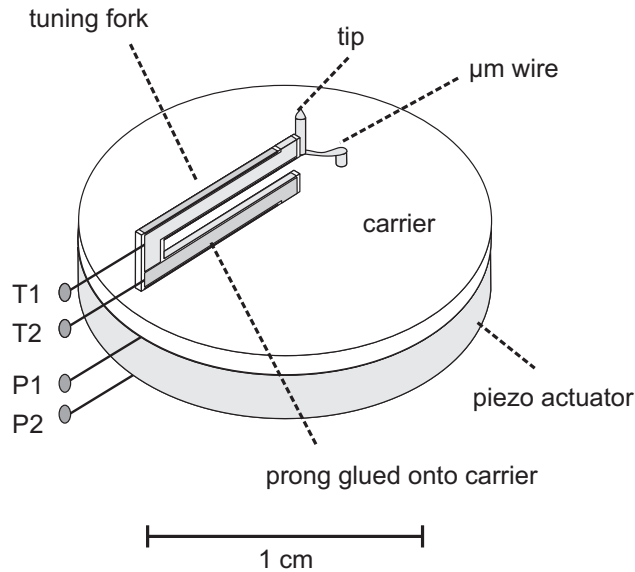


Figure 2.3: The tuning fork is glued onto the carrier made of marcor. Contacts P1 and P2 are for the contact of the excitation piezo. The signal from the tuning fork is detected via contact T1 and T2. The  $\mu\text{m}$  wire attached to the tip conducts the tunneling current.

frequency of 32768 Hz ( $=2^{15}$  Hz). In the setup employed one prong of the tuning fork is glued onto a carrier. To the other prong a  $\text{Pt}_{0.9}\text{Ir}_{0.1}$  cut wire, 250  $\mu\text{m}$  in diameter, is attached with insulating glue. In this manner the electrodes of the tuning fork are insulated from the tip, which is a very important point as discussed later in this section. Due to the fixed prong and the additional mass of the tip at the other prong, the resonance frequency drops to about 22 kHz. Since the tuning fork is excited at its resonance frequency by the excitation piezo, a signal of the resonance frequency can be detected at its electrodes due to the piezo electric effect. The amplitude of the signal is proportional to the oscillation amplitude of the tuning fork. The signal is so small that an amplifier has to be placed nearby to reduce noise. The frequency signal of the tuning fork is used as a feedback signal for DFM. The tip is electrically connected to a  $\text{Pt}_{0.9}\text{Rh}_{0.1}$  wire, 50  $\mu\text{m}$  in diameter (compare figure 2.3). Using this electrical contact a tunneling current can be measured and serves as a feedback signal when operating in the STM mode. However, while operating in one of the modes, DFM or STM, the other channel can always be co-recorded. Much care has been taken to ensure that the two channels, DFM and STM, are electrically separated from each other, preventing cross talk to occur. This setup allows DFM and STM investigations with the same tip on the same surface area at 5 K in ultrahigh

vacuum, making it a powerful tool for high resolution real space analysis at the atomic level and merging the strength of both techniques.

## 2.3 Dynamic Force Microscopy

In this section an introduction into dynamic force microscopy, focusing on high resolution measurements, is given.

### 2.3.1 Frequency Modulation Dynamic Force Microscopy

In the dynamic operation mode the force sensor (here tuning fork) is oscillating. The oscillation prevents the so-called jump-to-contact when the force gradient  $-dF_{ts}/dz$  becomes larger than the spring constant  $c_z$ , where  $F_{ts}$  represents the tip-sample force. When the tip is in contact with the sample no high resolution imaging is possible since multi apex tip-sample contacts are formed. The oscillation adds an additional restoring force to the force sensor preventing a jump-to-contact. In ultrahigh vacuum a tuning fork setup has a high quality factor  $Q$  making the amplitude of the oscillating sensor an inadequate feedback signal since the response time to a disturbance in amplitude is far too long for proper data acquisition times. The time constant for the amplitude to be in a steady state is given by  $\tau \approx Q/(\pi f_0)$ , with  $f_0$  as the resonance frequency [24]. Typical  $Q$  values can be larger than 50000. Therefore the data acquisition bandwidth is larger than 1 s in many cases - which is far too long. Albrecht et al. [24] presented the frequency modulation mode where the shift in resonance frequency is detected caused by changes in force gradient  $dF_{ts}/dz$ . The response time for the frequency shift is given by  $\tau_{FM} \approx 1/f_0$  [39] and is therefore ideal for reasonable data acquisition times. Furthermore the sensitivity to the force gradient makes the frequency modulation mode the perfect operation mode when high resolution investigations are demanded. A schematic showing the implementation of the FM mode is shown in figure 2.4. The signal from the tuning fork is fed back into an automatic gain control (AGC) and afterwards into a phase shifter. The gain factor is adjusted such that the oscillation amplitude is constant. The phase of the excitation signal connected to the excitation piezo is phase shifted by  $90^\circ$  with respect to the incoming signal. This ensures that the tuning fork is oscillating at its resonance frequency. Since the resonance frequency is determined by the tuning fork itself and the tip-sample interaction, this system is often called self driven oscillator. The green channel in figure 2.4 conducts the tunneling current and will be discussed in section 2.4. The signal from the tuning fork is compared with a resonance frequency shift set-point. The

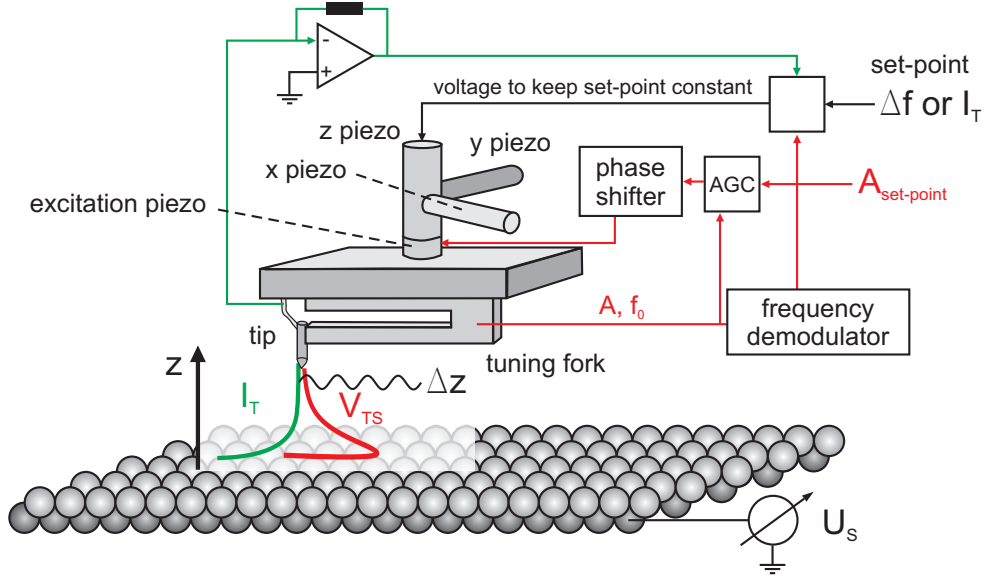


Figure 2.4: Schematic setup of a dual mode FM-DFM/STM. The signal from the tuning fork is amplified (AGC: automatic gain control) and phase shifted before it drives the excitation piezo. In this setup either the frequency shift (detected from the red circuit) or the tunneling current (green circuit) can be used as a feedback signal to control the  $z$  displacement between tip and sample. However while only one signal can be used as feedback both signals can be simultaneously recorded.

resonance frequency of the free oscillating tuning fork without tip-sample interaction is  $f_0$ . If tip-sample forces occur the resonance frequency changes to  $f'_0$  and the resonance frequency shift is then given by  $\Delta f = f'_0 - f_0$ . A voltage applied to the  $z$  piezo is adjusted such that the shift of the resonance frequency  $\Delta f$  chosen by the experimenter is kept constant while the tip scans across the surface according to the  $x$  and  $y$  piezos. Thus recorded FM-DFM images are constant  $\Delta f$  images. The resonance frequency shift is often called frequency shift for brevity.

### 2.3.2 Potentials and Forces in DFM

These days it is well established that there are four distinct fundamental forces. The strong and weak interactions act between neutrons, electrons, protons and other elementary particles. These forces are very short range in character, less than  $10^{-5}$  nm, and are investigated in the research fields of nuclear and high energy physics [40]. Electromagnetic and gravitational forces complete the four distinct forces in nature. These forces act over a

much longer range. On the scale of molecules Richard P. Feynman derived that all intermolecular interactions are essentially electrostatic in origin [40, 41]. This knowledge is based on the development of the quantum theory in the 1920s. With the quantum theory it became possible to derive an expression for the interaction potential and thus also for the interaction force. In the research field of atomic force microscopy it is useful to classify the interaction in seemingly different categories.

Forces detectable in dynamic force microscopy in ultra high vacuum at low temperature have been classified in three main categories [40]. The first category covers forces between charges and are therefore electrostatic in origin arising from Coulomb forces. These forces arise from the interaction between charges, permanent dipoles and higher order moments. Polarization forces belong to the second category. These forces are determined by dipole moments induced in atoms or molecules by electric fields of permanent dipoles and charges nearby. The third category covers bonding forces which are therefore quantum mechanical in nature. These forces lead to charge transfer processes as involved in covalent bonding. Furthermore, the repulsive exchange forces due to the Pauli exclusion principle that balance the attractive forces at short distances fall into this category.

The classification into these three groups is not rigid nor exhaustive, as for example, the van-der-Waals force which falls into category two is a general consequence of the zero-point energy in quantum mechanics [42, 43]. Furthermore magnetic forces, friction forces, capillary forces etc. can in principle occur in atomic force microscopy, but are not relevant in this paper, since a magnetic tip is necessary to detect magnetic forces or a tip has to be in contact with the surface to measure friction forces. In the following the forces relevant for this paper will be discussed.

### Electrostatic/Coulomb interaction

Coulomb forces are a result of charges and can be stronger than most chemical binding forces [40]. The free energy of the Coulomb potential  $V_{CP}$  between two charges  $Q_1$  and  $Q_2$  is given by

$$V_{CP}(z) = \frac{Q_1 Q_2}{4\pi\epsilon_0\zeta z}, \quad (2.1)$$

where  $\zeta$  is the relative permittivity or dielectric constant of the medium and  $z$  the distance between the charges. The Coulomb force  $F_{CF}$  is given by

$$F_{CF} = -\frac{dV_{CP}}{dz} = \frac{Q_1 Q_2}{4\pi\epsilon_0\zeta z^2}. \quad (2.2)$$

The electric field  $\epsilon$  of a point charge  $Q$  at a distance  $z$  is thus

$$\epsilon = \frac{Q}{4\pi\epsilon_0\zeta z^2} . \quad (2.3)$$

The detection of the electrostatic force with a dynamic force microscope is often called Kelvin probe force microscopy (KPFM) ascribed to Lord Kelvin who measured contact potential differences [44]. The contact potential difference (CPD) results from the alignment of Fermi levels from tip and sample having different work functions. The tip-sample geometry can be considered as a plate capacitor resulting in the following equation for the total energy  $E_{tot}$  [45, 46]

$$\begin{aligned} E_{tot} &= E_{el} - E_{VS} \\ &= \frac{n^2q^2}{2C_\Sigma} + \frac{C_1C_2U^2}{2C_\Sigma} - \left[ nq\frac{C_1}{C_\Sigma}U + \frac{C_1C_2U^2}{C_\Sigma} + \frac{C_0}{2}U^2 \right] \\ &= \frac{n^2q^2}{2C_\Sigma} - nq\frac{C_1}{C_\Sigma}U - \frac{C_1C_2U^2}{2C_\Sigma} - \frac{C_0}{2}U^2 , \end{aligned} \quad (2.4)$$

where  $E_{el}$  is the electrostatic charging and  $E_{VS}$  is the work done by the voltage source. Furthermore,  $C_\Sigma(z) = C_1(z) + C_2$ ,  $C_1(z)$  is the capacity between the tip and a defect on the surface,  $C_2$  is the capacity between the defect and the substrate and  $C_0$  is the capacity between the tuning fork back electrodes and the surface. A schematic showing the tip-sample geometry and the resulting capacities is given in figure 2.5.  $U = U_S - \frac{\Delta\Phi_{loc}}{|q|}$ ,  $U_S$  is the voltage applied to the sample,  $q$  is the defect charge,  $\Delta\Phi_{loc}$  is the local work function shift resulting from local contact potential differences while  $n$  represents the number of charges  $q$ . The derivative of equation 2.4 results in the electrostatic force given by

$$F_{el} = \frac{1}{2} \frac{\partial C_S}{\partial z} \left( \frac{nq}{C_2} + U \right)^2 + \frac{1}{2} \frac{\partial C_0}{\partial z} U^2 , \quad (2.5)$$

where  $C_S$  is given by a capacitor series  $C_S = C_1 \cdot C_2 / (C_1 + C_2)$ . The last term in equation 2.5 can be neglected when high resolution is considered, since the electrostatic force between the substrate and the tuning fork's back electrodes integrates a large surface area [45]. The MgO film behaves like a dielectric medium. If no charges from defects or adsorbates are present on the surface equation 2.5 reduces to

$$F_{el} = \frac{1}{2} \frac{\partial C_S}{\partial z} \left( U_S - \frac{\Delta\Phi_{loc}}{|q|} \right)^2 . \quad (2.6)$$

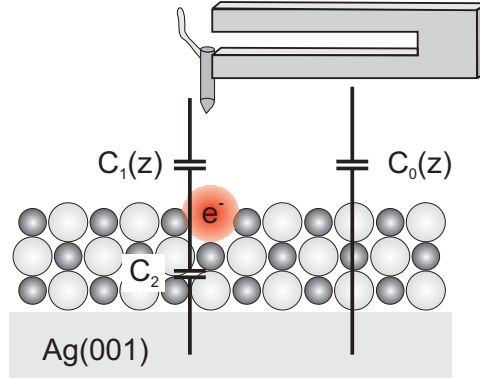


Figure 2.5: Tip-sample geometry showing the capacities. The term  $C_1(z)$  is the capacity between tip and defect (red) which depends on the tip displacement,  $C_2$  is the capacity between defect and metal support and  $C_0(z)$  is the capacity between the tuning fork's back electrode and the metal support. The MgO film behaves like a dielectric medium.

Tip and sample are not directly in contact but are electrically connected via the electronics as shown in figure 2.4. The electrical contact leads to the alignment of Fermi levels from tip and sample. In figure 2.6(a) tip and sample are not electrically connected thus the vacuum levels are equal and the Fermi levels do not align. In figure 2.6(b) tip and sample are electrically connected and electrons from the material with the lower work function (here tip) flow to the material with the higher work function, thus the Fermi levels align and an electrical field is built up [47]. The contact potential difference is then given by the difference in work functions  $\Delta\Phi$ . The advantage of KPFM compared with e.g. UPS is the high local resolution down to single point defects or single adsorbates instead of integrating over a square millimeter range, however, no absolute work functions can be directly measured, only work function differences.

Experimental data showing the tip-sample interaction in parameter space i.e. with respect to  $z$  displacement and bias voltage  $U_S$  are presented in figure 2.7. The experimental data can be recorded either at a constant  $z$  displacement measuring the frequency shift  $\Delta f$  with respect to bias voltage or at a constant bias voltage  $U_S$  detecting the frequency shift  $\Delta f$  as a function of  $z$  displacement. During the measurements a stable tip configuration has to be ensured. The electrostatic interaction in the parameter space of bias voltage  $U_S$  and displacement  $z$  has been simulated in the following manner. A Lennard-Jones potential  $E_{LJ}$  has been used to describe the attractive and repulsive interactions with respect to  $z$ . The Lennard-Jones potential has

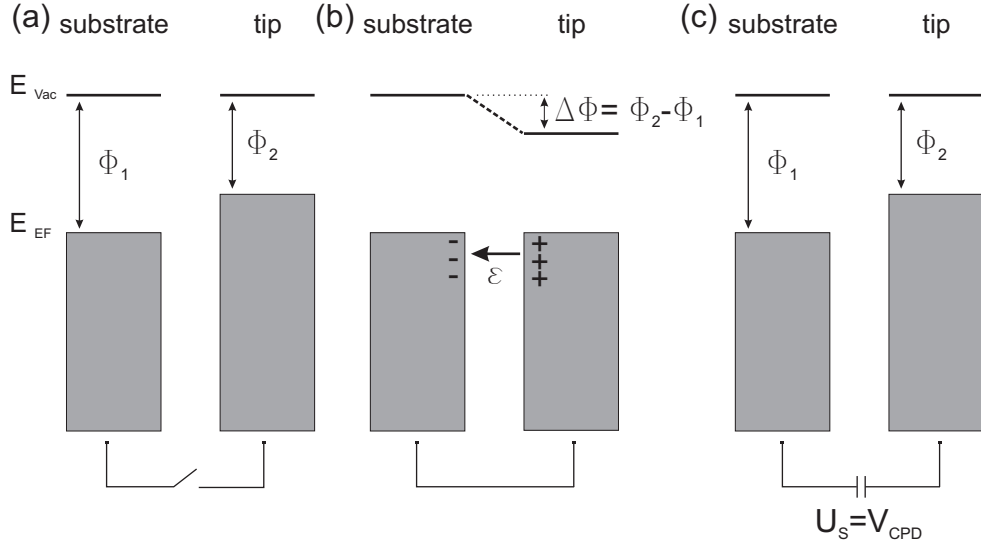


Figure 2.6: (a) The Fermi levels of tip and sample when they are not electrically connected. (b) Tip and sample are electrically connected and the Fermi levels align resulting in an electrostatic field  $\epsilon$  due to the contact potential difference. (c) If the sample bias voltage  $U_S$  equals the contact potential difference  $V_{CPD}$  the electrostatic field is canceled.

been superimposed by an electrostatic potential  $E_{el}$ , which is a function of  $z$  since the capacity between tip and sample  $C_{ts}$  depends on  $z$ . In addition  $E_{el}$  is a function of the applied bias voltage  $U_S$ . The derivative of these superimposed potentials leads to the following tip-sample interaction force

$$\begin{aligned}
 F_{total} &= F_{LJ} + F_{el} \\
 &= \frac{12\epsilon}{z_0} \left\{ \left( \frac{z_0}{z} \right)^{13} - \left( \frac{z_0}{z} \right)^7 \right\} + \frac{1}{2} \frac{\partial C_{ts}(z)}{\partial z} \left( U_S - \frac{\Delta\Phi}{|q|} \right)^2
 \end{aligned} \quad (2.7)$$

with  $\epsilon$  as the equilibrium's energy,  $z_0$  the equilibrium's distance,  $\Delta\Phi$  the contact potential and  $q$  the electron charge. The tunneling current has been assumed to be exponentially dependent on  $z$  and bias voltage  $U_S$ . Furthermore the occupied and unoccupied states have been assumed to be symmetrically distributed across the Fermi level.

The experimental data are presented in figure 2.7.

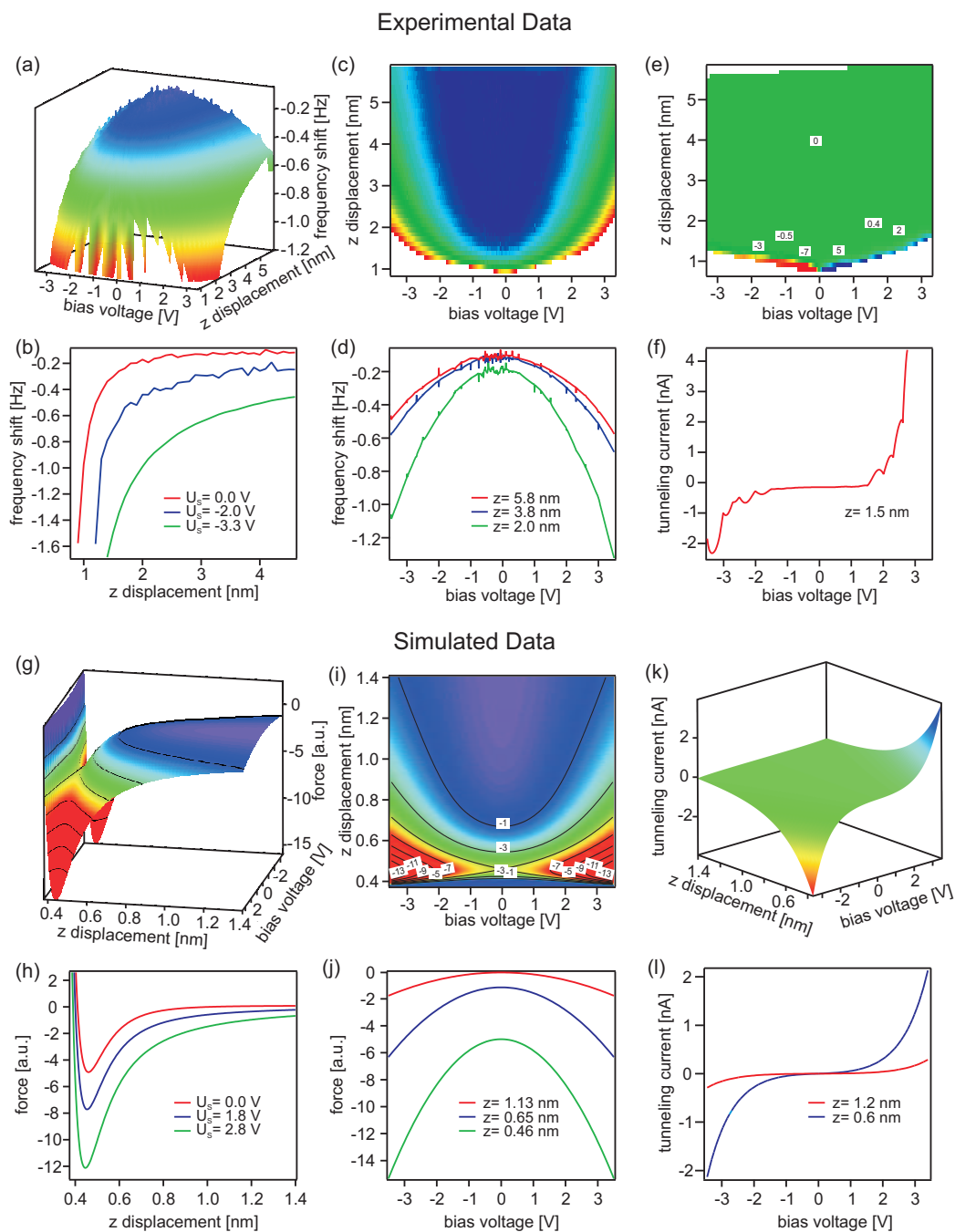


Figure 2.7: (a-d) Experimental data showing the electrostatic tip-sample interaction. (e, f) Simultaneously recorded tunneling current. (g-j) Simulated electrostatic tip-sample interaction based on equation 2.7. (k, l) Simulated tunneling current. Details are discussed in the corresponding text.

Figures 2.7(a-d) show the dependency of the electrostatic force i.e. resonance frequency shift  $\Delta f$  with respect to  $z$  displacement and bias voltage  $U_S$ . In figure 2.7(a) the attractive regime with positive slope is shown. The surface is a part of a saddle which will be recognized from the simulated data. Cuts at constant bias voltages are shown in figure 2.7(b). The graphs at different bias voltages  $U_S$  show with increasing absolute voltages a stronger tip-sample interaction since  $F_{el}$  increases according to equation 2.7. The qualitative behavior resembles a Lennard-Jones equivalent response. Figure 2.7(c) displays the resonance frequency shift  $\Delta f$  in 2D parameter space, while figure 2.7(d) shows cuts through the saddle at constant  $z$  positions.

If the  $z$  position is constant and the voltage swept, only the electrostatic force varies while the contribution from the Lennard-Jones interaction is constant (compare equation 2.7). The interaction shows a parabolic behavior, since the force depends on the square of the applied bias voltage and is therefore always attractive. The desired information about local electronic properties is now included in the shift of the parabola along the abscissa. The shift results from the local potential  $\Delta\Phi$  also known as contact potential difference or local work function (compare equation 2.7). However, the local potential can be significantly affected by adsorbates [48] or local charges as for example present in charged adsorbates [49] or defect sites [50].

The shift of the parabolas along the ordinate in figure 2.7(d) is related to the Lennard-Jones interaction between tip and sample at different tip-sample separations and carries therefore information about the strength of the Lennard-Jones potential at a given  $z$  distance. Figures 2.7(e,f) show the simultaneously recorded tunneling current. For the given  $z$  distance in figure 2.7(f) the tunneling current increases significantly at about  $\pm 2$  V. Here it is important to ensure that the tunneling current is not reaching the overload of the preamplifier. The overload of the preamplifier will suddenly change dramatically the electrostatic tip-sample interaction, since neither tip nor sample are on virtual ground any longer then. However, the experimental mapping of the full force saddle is often difficult, since tip changes occur very likely when the tip enters the repulsive regime. Therefore, the Lennard-Jones interaction superimposed by an electrostatic force has been simulated by equation 2.7 based on a simple pair potential analysis in analogy to Refs. [51, 52]. The results are shown in figure 2.7(g-l). Figure 2.7(g) shows the three dimensional saddle resulting from the superposition of the derivative of a Lennard-Jones potential and an electrostatic potential. In figure 2.7(h) cuts through the saddle for constant bias voltages  $U_S$  are shown. The cuts resemble the behavior of the experimental data. Figure 2.7(i) shows a two dimensional plot of (g). The graphs in figure 2.7(j) show cuts through figure 2.7(g) at constant  $z$  displacements, showing the typical parabolic behavior

while (k) and (l) represent the tunneling current in analogy to figure 2.7(e,f). Overall the simulated data agree qualitatively well with the experimental results. The data presented in figure 2.7 are attributed to fixed  $x, y$  positions on the surface.

To determine differences in saddles of different  $x, y$  positions on the surface it is necessary to measure shifts with respect to bias voltage at a constant  $z$  position. The shift with respect to the zero bias voltage is given by  $\Delta\Phi_1 = \Phi_{site A} - \Phi_{tip}$ , where  $\Phi_{site A}$  and  $\Phi_{tip}$  are the work functions of surface site A and tip respectively and for a second measurement on site B  $\Delta\Phi_2 = \Phi_{site B} - \Phi_{tip}$ . By taking the difference  $\Delta\Phi_1 - \Delta\Phi_2$  the work function of the tip cancels and  $\Delta\Phi = \Phi_{site A} - \Phi_{site B}$ . However, stable tips are a prerequisite for such measurements as will be discussed in chapters 4 and 5.

The electrostatic force also affects the resolution during lateral scans at a constant tip-sample interaction and therefore at a constant resonance frequency shift. The black contour lines in Figs. 2.7(g and i) are examples of possible  $\Delta f$  set-points. Following such a contour means constant tip-sample interaction and therefore a constant resonance frequency shift. However, the resolution for local imaging is not constant along such a contour. For a given resonance frequency shift the tip-sample distance is always the smallest if  $U_S$  equals  $\Delta\Phi$  i.e. at compensated contact potential and thus  $F_{el}$  equal to zero. Under these conditions, since the tip-sample distance is the closest, high resolution is most likely assuming the set-point is set deep enough within the potential on the scale of chemical bonds and assuming a sharp tip apex.

The origin of work function shifts and its impact on surface chemistry on MgO will be discussed in chapter 4.

### Van-der-Waals interaction

Van-der-Waals forces, commonly referred to as London forces, originate from induced fluctuating dipoles in atoms or molecules [43, 53]. For two hydrogen atoms the van-der-Waals interaction potential can be derived by solving the Schrödinger equation assuming a dipole-dipole interaction [42]. The van-der-Waals interaction potential can then be outlined as

$$V_{vdW}(z) = -\frac{C}{z^6} = -6.47 \frac{e^2 z_B^5}{z^6}. \quad (2.8)$$

Here  $z_B$  is the Bohr radius. Due to the minus six power dependence, which has been found to be universal [42], the van-der-Waals force is long range in character compared with covalent bond interaction. Therefore when considering a tip-sample geometry an integration of tip and sample has to be

performed [42]

$$V_{vdW} = -\frac{\pi C \rho_1 \rho_2}{6} \int_{z=0}^{\infty} \frac{2\pi R_c h}{(h+z)^3} dh \quad (2.9)$$

where  $h$  is the tip length,  $R_c$  is the radius of tip curvature,  $\rho_{1,2}$  are the densities of tip and sample respectively. By defining the Hamaker constant as

$$A \equiv \pi^2 C \rho_1 \rho_2 \quad (2.10)$$

the van-der-Waals interaction energy results in

$$V_{vdW}(z) = -\frac{AR_c}{6z} . \quad (2.11)$$

Hence the van-der-Waals force for a tip with curvature  $R_c$  above a surface results in

$$F_{vdW}(z) = -\frac{AR_c}{6z^2} . \quad (2.12)$$

Typical values of the Hamaker constant of metal surfaces are  $A \approx 2 - 3$  eV [40, 42].

### Covalent Binding and Pauli Repulsion Forces

Covalent binding forces are a result of overlapping electron orbitals. In contrast to, e.g., electrostatic forces they are directional. Compared with the van-der-Waals and electrostatic forces, covalent binding forces are short range in nature. Typical ranges are interatomic binding distances of 1 to 2 Å. These forces are supposed to be responsible for the atomic contrast in atomically resolved images since their variation is on a very small scale while other forces will be integrated over a larger area defined by the tip-sample geometry. At distances smaller than the binding distance the repulsive forces start to increase dramatically with decreasing separation. This repulsion arises from the Pauli exclusion principle. Since electrons are Fermions, they have to differ in their quantum numbers. If this is not possible, they will be lifted in energy resulting in a repulsive force. Due to their short range nature atomic resolution in the repulsive regime is possible but tip changes, i.e. plastic deformation of the tip apex is very likely.

### Potentials

An empirical potential describing the tip-sample interaction is the Lennard-Jones potential. The Lennard-Jones potential is a good approximation of

inert gas atoms interaction. The attractive part of the Lennard-Jones potential is given by the van-der-Waals term and the repulsive interaction is given by a 12th power function

$$V(z) = V_0 \left[ \left( \frac{z_m}{z} \right)^{12} - 2 \left( \frac{z_m}{z} \right)^6 \right], \quad (2.13)$$

where  $z_m$  is the  $z$  position of the minimum and  $V_0$  the potential depth. A Morse potential is often used for covalent interactions and is given by

$$V(z) = V_0 \left( 1 - e^{-a(z-z_m)} \right)^2, \quad (2.14)$$

with  $V_0$  and  $z_m$  as defined above. Furthermore, Rydberg potentials are often used [54, 55]

$$V(z) = V_0 \left( 1 + \frac{z - z_m}{l} \right) e^{-(z-z_m)/l}, \quad (2.15)$$

where  $l$  is a decay constant. The different potentials are presented in figure 2.8.

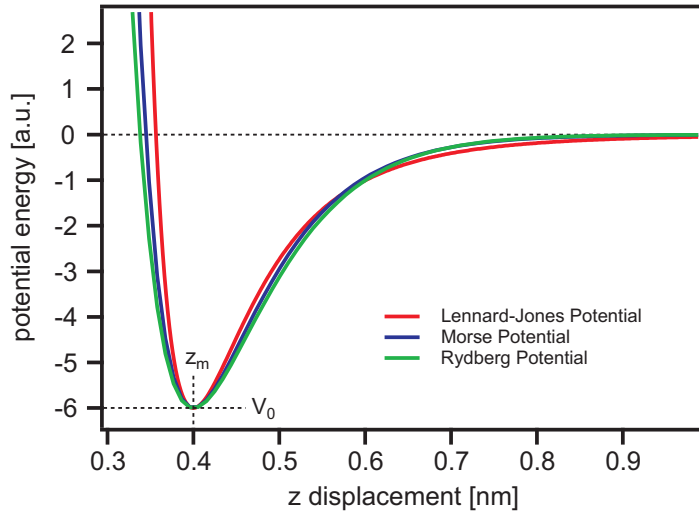


Figure 2.8: Comparison of a Lennard-Jones (red), Morse (blue) and Rydberg potential (green). The Lennard-Jones potential has the strongest slope in the repulsive regime.

By comparing the potentials it becomes obvious that they are quite similar, however, since the van-der-Waals potential describes the interaction of inert atoms, the slope in the repulsive regime is the largest.

### 2.3.3 Theoretical Approach to FM-DFM

In the following a theoretical approach to determine the frequency shift of a tuning fork due to tip-sample interaction forces will be presented. In frequency modulation dynamic force microscopy the oscillating tuning fork can be described by a driven and damped harmonic oscillator. The equation of motion of this system is given by [56]

$$\underbrace{m^* \ddot{z}(t)}_{\text{Newton}} + \underbrace{\frac{2\pi f_0 m^*}{Q} \dot{z}(t)}_{\text{Stokes' friction}} + \underbrace{c_z z(t)}_{\text{Hook's law}} + \underbrace{g c_z z(t - t_0)}_{\text{excitation}} = \underbrace{F_{ts}[z(t), \dot{z}(t)]}_{\text{tip-sample-force}}, \quad (2.16)$$

where  $z(t)$  represents the position of the tip at time  $t$  and  $m^*$ ,  $f_0$ ,  $c_z$  and  $Q$  stand for the effective mass, the resonance frequency, the spring constant and the dimensionless quality factor, respectively. The quality factor is given by  $\gamma = 2\pi f_0 m^*/Q$  with  $\gamma$  as a damping coefficient. Furthermore,  $g$  represents the gain factor for the excitation of the oscillating tuning fork keeping the oscillation amplitude constant. The term  $z(t - t_0)$  describes the time shifted i.e. phase shifted excitation to ensure the system is oscillating at its resonance frequency. The resonance frequency of the tuning fork itself is given by  $f_0 = \frac{1}{2\pi} \sqrt{c_z/m^*}$ . The first term in equation 2.16 is given due to inertia, the second represents Stokes' friction of the tuning fork with the surrounding area. The third term shows the restoring force of the tuning fork by Hook's law. The fourth term represents the excitation of the tuning fork. Term number five stands for the tip-sample interaction depending on distance  $z$  and the tuning fork's velocity  $\dot{z}$ . To solve the differential equation 2.16 the following ansatz can be used

$$z(t) = A \cos(2\pi f t), \quad (2.17)$$

where  $f$  is the present oscillation frequency. To successfully solve the equation of motion the following three assumptions have to be fulfilled

1. The force acting between tip and sample  $F_{ts}$  is a function of displacement  $z(t)$  and velocity  $\dot{z}(t)$ .
2. The oscillation of the tuning fork and thus the tip is sinusoidal and the nonlinear forces between tip and sample are always smaller than the restoring force i.e.  $F_{ts} \ll c_z A$  preventing a jump-to-contact.
3. The oscillation amplitude  $A$  is constant which is ensured by adjusting the gain factor  $g$ .

While the ansatz is inserted into the left hand side of the equation of motion the right hand side is evolved either into a Taylor series or a Fourier series. However, the evolution into a Fourier series turns out to be more straight forward due to the sinusoidal oscillation of the tuning fork. Thus the tip-sample force can be written as

$$\begin{aligned}
\frac{1}{m^*} F_{ts}[z(t), \dot{z}(t)] &= \underbrace{\frac{f}{m^*} \int_0^{1/f} F_{ts}[z(t), \dot{z}(t)] dt}_{=1.\text{Term}} + \\
&+ \underbrace{2 \frac{f}{m^*} \int_0^{1/f} F_{ts}[z(t), \dot{z}(t)] \cos(2\pi ft) dt \cdot \cos(2\pi ft)}_{I_{\text{even}}} + \\
&+ \underbrace{2 \frac{f}{m^*} \int_0^{1/f} F_{ts}[z(t), \dot{z}(t)] \sin(2\pi ft) dt \cdot \sin(2\pi ft)}_{I_{\text{odd}}} + \\
&+ \text{higher harmonics} .
\end{aligned} \tag{2.18}$$

The first term is a constant effecting the rest position of the tuning fork, and can be neglected. In the following the tuning fork is assumed to oscillate at its resonance frequency, so the higher harmonics will vanish. Inserting the ansatz and the Fourier series into the equation of motion 2.16 results in

$$I_{\text{even}} = \frac{f_0^2 - f^2}{f_0^2} + g \cos(2\pi f t_0) , \tag{2.19}$$

$$I_{\text{odd}} = -\frac{f}{f_0 Q} + g \sin(2\pi f t_0) . \tag{2.20}$$

These are two coupled trigonometrical equations which can be solved numerically. If the phase shift between excitation and oscillation is  $\approx 90^\circ$ , i.e.  $t_0 = \frac{1}{4f_0}$ , the tuning fork oscillates at its resonance frequency. Therefore, the cosine term in equation 2.19 becomes zero and the sine term in equation 2.20 becomes one. This leads to

$$I_{\text{even}} = \frac{f_0^2 - f^2}{f_0^2} \Rightarrow \frac{f_0^2 - f^2}{f_0^2} = \frac{2f}{Ac_z} \int_0^{1/f} F_{ts}[z(t), \dot{z}(t)] \cos(2\pi ft) dt \tag{2.21}$$

and

$$I_{\text{odd}} = \frac{-f}{f_0 Q} + g \Rightarrow g = \frac{f}{f_0 Q} + \frac{2f}{Ac_z} \int_0^{1/f} F_{ts}[z(t), \dot{z}(t)] \sin(2\pi ft) dt . \tag{2.22}$$

Assuming that  $\Delta f$  is much smaller than  $f_0$ , i.e.  $\Delta f \ll f_0$ , results in

$$\frac{f_0^2 - f^2}{f_0^2} \cong \frac{-2\Delta f}{f_0} . \quad (2.23)$$

Therefore the two coupled harmonic equations 2.19 and 2.20 are now decoupled and the frequency shift  $\Delta f$  and the gain factor  $g$  can be expressed as

$$\Delta f \cong -\frac{f \cdot f_0}{Ac_z} \int_0^{1/f_0} F_{ts}[z(t), \dot{z}(t)] \cos(2\pi f_0 t) dt , \quad (2.24)$$

and

$$g \cong \frac{f}{f_0 Q} + \frac{2f}{Ac_z} \int_0^{1/f_0} F_{ts}[z(t), \dot{z}(t)] \sin(2\pi f_0 t) dt . \quad (2.25)$$

These two equations are valid for all types of tip-sample interactions and the full amplitude range. The  $g$  factor is a measure for dissipative tip-sample interactions and vanishes for pure conservative forces [57–59]. A further variable transformation leads to

$$\frac{z}{A} = \cos(2\pi f t) \Leftrightarrow t = \frac{1}{2\pi f} \arccos\left(\frac{z}{A}\right) , \quad (2.26)$$

$$\frac{dt}{dz} = -\frac{1}{2A\pi f} \frac{1}{\sqrt{1 - \frac{z^2}{A^2}}} = -\frac{1}{2\pi f} \frac{1}{\sqrt{A^2 - z^2}} . \quad (2.27)$$

For conservative tip-sample interactions  $F_{ts}$  is independent of  $\dot{z}(t)$ . Using  $u = z/A$  results in [60, 61]

$$\Delta f = -\frac{f_0}{\pi Ac_z} \int_{-1}^1 F_{ts}[D + A(1 + u)] \frac{u}{\sqrt{1 - u^2}} du , \quad (2.28)$$

where  $D$  is the distance of the closest approach during the oscillation cycle. With equation 2.28 it is now possible to derive the resonance frequency shift  $\Delta f$  of a tuning fork with spring constant  $C_z$  and oscillation amplitude  $A$  for a given tip-sample interaction  $F_{ts}$ . However, since the resonance frequency shift is detected in FM-DFM and the force is the desired quantity the inversion of the integral, i.e. the possibility of calculating the force from a detected frequency shift is very important.

### 2.3.4 Calculating the Force between Tip and Sample

The inversion of equation 2.28 is of fundamental interest if quantitative analysis is desired. However, the inversion is not straightforward and many attempts have been made in the past. To simplify the inversion some researchers assumed large oscillation amplitudes of their cantilevers compared with the interaction decay length of the potential and force [56, 62, 63]. Dürig developed a method based on Chebyshev polynomials for small oscillation amplitudes compared with the decay length of the tip-sample interaction [57].

Based on the fact that frequency shift data in an experiment is recorded in an discrete manner Giessibl [64] introduced a matrix inversion method which was extended by Pfeiffer [65]. However the most accurate and accepted inversion method, valid at all amplitudes, has been developed by Sader and Jarvis [61]. They expressed the interaction force formally as

$$F_{ts}(z) = \int_0^{\infty} W(\lambda) \exp(-\lambda z) d\lambda, \quad (2.29)$$

where  $W(\lambda)$  is the inverse Laplace transformation of  $F_{ts}(z)$ . Substituting equation 2.29 into equation 2.28 leads to

$$\Delta f = \frac{f_0}{Ac_z} \int_0^{\infty} W(\lambda) T(\lambda A) \exp(-\lambda z) d\lambda, \quad (2.30)$$

where  $T(x) = I_1(x) \exp(-x)$  is the modified Bessel function of the first kind [66]. In Laplace space, force and frequency differ only by a constant factor and  $T(x)$ . Therefore equation 2.28 can be inverted exactly. With the operators  $L\{\}$  and  $L^{-1}\{\}$  as the Laplace and inverse Laplace transformations  $F_{ts}$  results in

$$F_{ts}(z) = L \left\{ \frac{c_z A}{T(\lambda A)} L^{-1} \left\{ \frac{\Delta f(z)}{f_0} \right\} \right\}. \quad (2.31)$$

Following this route and evaluating the integrals, the force  $F_{ts}$  can be outlined as [61]

$$F_{ts}(D) = \frac{2c_z}{f_0} \int_z^{\infty} \left( 1 + \frac{A^{1/2}}{8\sqrt{\pi(z-D)}} - \frac{A^{3/2}}{\sqrt{2(z-D)}} \frac{d}{dz} \right) \Delta f(z) dz, \quad (2.32)$$

where  $D$  is the distance of the closest approach during the oscillation cycle. By integrating equation 2.32 the interaction potential  $V(z)$  can be deter-

mined [61]

$$V_{ts}(D) = \frac{2c_z}{f_0} \int_z^\infty \left( (z - D) + \frac{A^{1/2}}{4} \sqrt{\frac{z - D}{\pi}} + \frac{A^{3/2}}{\sqrt{2(z - D)}} \right) \Delta f(z) dz. \quad (2.33)$$

With equation 2.32 and 2.33 the interaction force and potential between tip and sample can now be calculated for arbitrary oscillation amplitudes.

The accuracy of equations 2.28, 2.32 and 2.33 has been tested in this paper based on an arbitrary Lennard-Jones potential with  $V_0 = -0.8$  aJ and  $z_m = 0.45$  nm.

The derivative of the potential, i.e. the Lennard-Jones force has been inserted into equation 2.28. The frequency shift has been calculated for different amplitudes ( $A = 10, 50, 100, 150, 200, 300, 400$  and  $500$  pm). Afterwards the derived frequency shift has been inserted into equation 2.33 to calculate the interaction potential. If the derived equations based on the assumptions made are accurate, the calculated potential should match the original Lennard-Jones potential. Moreover, the derivative of the potential, i.e. the Lennard-Jones force should match the original Lennard-Jones force. Figure 2.9(a) shows as a blue line the Lennard-Jones Potential, as a red line the derivative of the Lennard-Jones potential and in different green lines the frequency shift for different oscillation amplitudes. As expected for large amplitudes the potential is already recognized at quite large absolute  $z$  separations of tip and sample. Note only in simulation absolute tip-sample separations are known.

With decreasing oscillation amplitude the potential energy of the harmonic potential of the unperturbed tip decreases, therefore the tip-sample interaction disturbing the harmonic oscillation of the tip has a stronger impact, i.e. the anharmonicity increases resulting in an increasing resonance frequency shift. It is interesting to note that for oscillation amplitudes of about 10 pm the frequency shift minimum is located almost at the same  $z$  position as the minimum of the spring constant (orange curve). Thus for small oscillation amplitudes a lock-in technique of the force is observed and the frequency shift is related to the spring constant by a dimensional scaling factor. Hence, for small oscillation amplitudes the tip-sample force and potential can be calculated in a straight forward manner by a simple integration which makes the numerical approach to solve equation 2.28 unnecessary.

However, calculating the interaction potential with equation 2.33 and by derivation the interaction force from these calculated frequency shifts result in the blue and red curves shown in figure 2.9(b). The blue and red curves are formally nearly equal. A further investigation of this data shows no

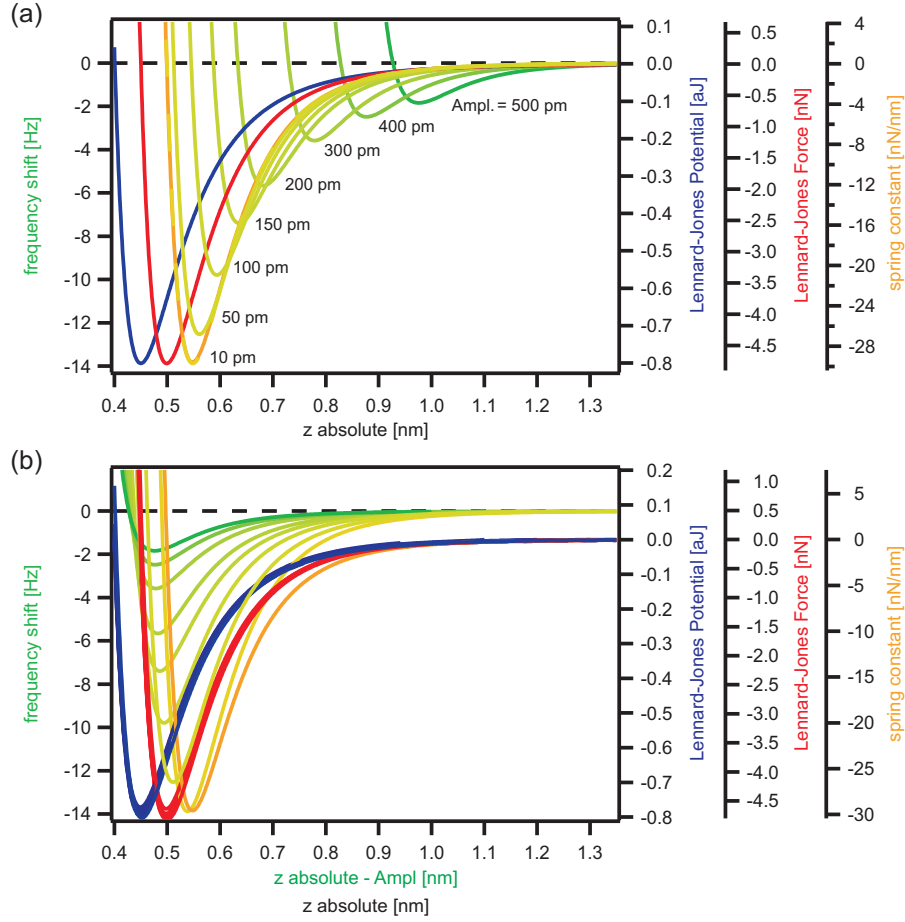


Figure 2.9: For a given Lennard-Jones potential  $V_0 = -0.8$  aJ,  $z_m = 0.45$  pm (blue line) shown in (a), the force (red line) and resonance frequency shifts (various green lines) for different tuning fork oscillation amplitudes have been calculated using equation 2.28. With equation 2.33 the potential has been recalculated (blue lines). (b) The recalculated potentials match the original interaction potential within  $\pm 3$  %. The orange line represents the spring constant related to the tip-sample interaction (discussion see text).

clear trend with amplitude. Beside the errors due to the assumptions made for deriving the equations an additional error is made when solving integral 2.28 and 2.33 numerically. However, the calculated potential curves from the frequency shifts match within  $\pm 3$  % the original Lennard-Jones potential. Since potential integrated during one oscillation process is determined by the oscillation amplitude in figure 2.9(b) the frequency shift data has been plotted vs  $z$  absolute - amplitude. This plot gives a better comparison of frequency shift, interaction force and interaction potential for a given  $z$  displacement.

## 2.4 Scanning Tunneling Microscopy

The second operation mode of the setup used is the STM mode. In this section the working principle of the STM will be discussed followed by a theoretical consideration of this technique. Finally scanning tunneling spectroscopy and field emission resonances will be discussed. In the following  $V$  is used as a synonym for the bias voltage  $U_S$ .

### 2.4.1 STM Operation Principle

A conducting sharp tip is brought very close to a conducting sample. Typical distances are in the picometer to nanometer range, thus tip and sample are not in electrical contact. Prerequisites are a high mechanical and thermal stability of the setup. If a voltage is applied at these close proximities electrons can tunnel from tip to sample or vice versa depending on the sign of the applied voltage due to overlapping wavefunctions. The tunneling current through the vacuum barrier exponentially depends on tip-sample distance  $z$ . When moving the tip laterally across the surface the tip-sample distance  $z$  can be adjusted such that the tunneling current stays constant. This mode is known as the constant current mode. The adjustment of the tip-sample distance can be recorded and displayed as an image. A second mode used less frequently is called constant height mode. In constant height mode the tip-sample distance is not adjusted while the tip scans across the surface and the variation of the tunneling current is detected. The constant height mode can only be applied on flat surfaces with low corrugation and well leveled tip surface geometries, because otherwise the tip crashes, destroying both the tip and/or the sample surface. The adjustment of tip-sample distance during the scan process is established by piezos leading to movements on the picometer scale. Since typical tunneling currents range between picoampere and nanoampere highly developed amplifiers are necessary. The amplified tunneling current signal is compared in a feedback loop with a tunneling current (set-point) chosen by the experimenter. Deviations from the set-point are adjusted by the  $z$  piezo controlling the tip-sample distance.

### 2.4.2 Theoretical Approach

The theory for understanding the mechanisms involved in STM has been strongly developed by Bardeen. His approach aimed to describe the tunneling experiment of Giaever [67] who wanted to verify the Bardeen-Cooper-Schrieffer theory of superconductivity [68]. A metal insulator metal junction designed by Giaever has been mathematically described by Bardeen using a

modified first order one dimensional perturbation theory. The wavefunctions of the two metals are supposed to be independent. Bardeen solved at first the Schrödinger equation of the subsystems and calculated then using time dependent perturbation theory the transition from one electrode to the other. The transition rate from the initial state to the final state obeys Fermi's Golden rule as expected. The tunneling current at a bias voltage  $V$  results in [42]

$$I_T = \frac{4\pi e}{\hbar} \int_{-\infty}^{\infty} [f(E_F - eV + E) - f(E_F + E)] \cdot \rho_T(E_F - eV + E) \rho_S(E_F + E) |M_{TS}|^2 dE, \quad (2.34)$$

where  $f(E) = (1 + \exp[(E - E_F)/k_B T])^{-1}$  is the Fermi-Dirac distribution function describing the energy distribution at temperature  $T$ . Since  $\rho_T$  and  $\rho_S$  represent the local density of states (LDOS) of tip and sample, respectively, the tunneling current is proportional to the convolution of both quantities.  $M_{TS}$  is the tunneling matrix element defined by the surface integral of the overlapping wave functions

$$M_{TS} = -\frac{\hbar^2}{2m} \int_S (\Psi_T^* \nabla \Psi_S - \Psi_S \nabla \Psi_T^*) dS. \quad (2.35)$$

The accuracy of the tunneling matrix element strongly depends on the wavefunctions  $\Psi_{T,S}$  of tip and sample. Tersoff and Haman assumed a spherical tip of radius  $R$  with a s-type orbital located at  $r_0$  [5] (see figure 2.10).

The contribution of the local density of states of the tip near the Fermi level can than be approximated to [69]

$$\rho_T(E_F) \propto |\Psi_T|^2 \propto T(z, E, eV), \quad (2.36)$$

where  $z$  is the distance from tip to substrate. The transition probability  $T(z, E, eV)$  for an electron to overcome the barrier is given by [5, 70]

$$T(z, E, eV) = \exp\left(\frac{-2z\sqrt{2m}}{\hbar} \sqrt{\frac{(\Phi_T + \Phi_S)}{2} - E + \frac{eV}{2} + k_{\parallel}^2}\right). \quad (2.37)$$

$\Phi_{T,S}$  are the work functions of tip and sample respectively. If only states near the  $\Gamma$  point contribute to the tunneling current, the parallel momentum  $k_{\parallel}$  of the surface electronic state becomes zero. With the assumptions made, the tunneling current can be outlined as

$$I_T \propto \int_0^{eV} \rho_S(E) e^{-2\kappa z} dE \quad (2.38)$$

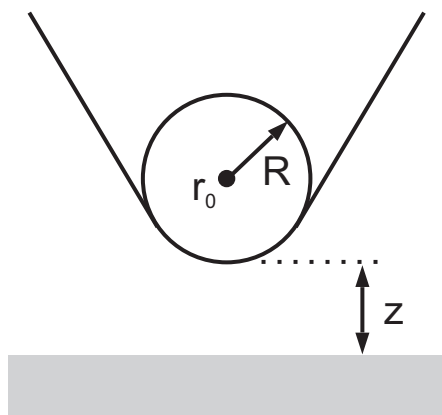


Figure 2.10: Schematic picture of the tunneling junction. The tip shape is assumed to be locally spherical with radius of curvature  $R$ . The center of the sphere is located at  $r_0$ . The tip-sample distance is given by  $z$ . Graphic taken from Ref. [5].

with  $\kappa$  as the inverse decay length given by equation 2.37. Equation 2.38 leads to a simplified understanding of STM images applied in many STM experiments where tip effects are supposed to play a minor role. Although the Tersoff Haman model can explain many experimental results it is often necessary to take more complex tip wavefunctions into account like  $p_z$  and  $d_{zz}$  states [42, 71] to achieve agreement with experiments. A potential energy scheme showing the tunneling junction is presented in figure 2.11. Figure 2.11(a) shows the junction of a metal surface and a metal tip while (b) indicates the tunneling junction with an oxide grown on top of the metal sample. The valence band (VB) and the conduction band (CB) of the oxide (dielectric media) is bent due to the electrostatic field  $\vec{\epsilon}$ . The direction of the electrostatic field  $\vec{\epsilon}$  depends on the sign of the applied voltage which furthermore determines the tunneling direction from tip to sample or sample to tip. However, one has to note that the assumptions made are not always valid. Some theoretical approaches have been made in the past to take fluctuations in the tip density of states into account to gain more accurate information on the sample density of states [72, 73].

### 2.4.3 Contrast Formation in High Resolution STM

In the following a few remarks concerning the contrast formation in STM will be discussed. In STM experiments understanding the origin of image contrast is not always straight forward. The convolution of the LDOS of tip and sample, as well as their different orbitals, can influence the contrast sig-

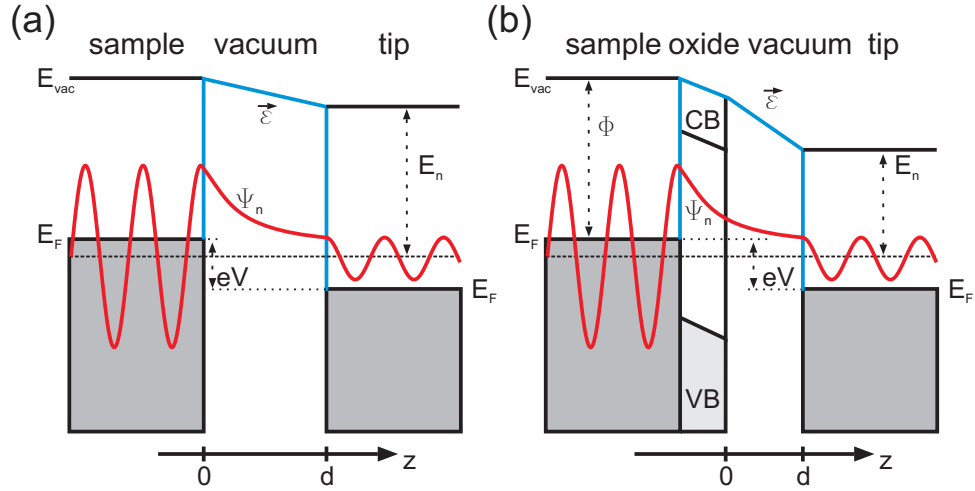


Figure 2.11: Potential energy scheme of the tunneling process. (a) Tunneling from occupied metal sample states to unoccupied tip states. (b) Same situation as (a) but with an oxide layer grown on top of the metal surface. The conduction band and valence band are bent due to the electric field  $\vec{\epsilon}$ .

nificantly. The influence depends on the tip-sample system. To understand high resolution STM images a further approach is necessary. In 1990 Eigler and Schweizer [74] manipulated single Xe atoms on a Ni(110) surface. Surprisingly the closed shell Xe atoms have been imaged as bright protrusions at a tip bias voltage of 10 mV i.e. electrons tunnel from the sample to the tip. The Xe  $5p^6$  ground state lies 6-8 eV below the Fermi level and the lowest empty state  $6s$  lies about 4.5 eV above the Fermi level [75]. Thus one would assume Xe atoms to be invisible in STM. A hole creation process in the Xe  $5p^6$  configuration is unlikely to contribute to the tunneling current since the energy needed is too high [76, 77]. Based on the theoretical calculations by Lang it has been found that the first electronic excited state of Xe  $5p6s$  seems to donate electrons [77]. Taking  $5d$  orbitals into account did not affect the tunneling current since these orbitals are too contracted to modify the tunneling current [76]. The  $6s$  state is virtually unfilled, however, quite extended and a small occupation will result in a difference in LDOS compared with the clean metal. This effect is supposed to be the imaging mechanism involved. Moreover, this approach shows that electrons tunneling from tip to surface or vice versa may interact with orbitals adsorbed on surfaces. Therefore effects like elastic scattering of electrons at orbitals have to be considered. The theoretical background accounting for these effects has been developed by Doyen based on Green's functions [78–80]. This approach is also necessary to explain the imaging mechanism of CO adsorbed on e.g. Cu(111). CO has been

found to appear as a depression when mapped with a clean metal tip [81]. If a CO molecule is picked up by the STM metal tip the CO molecules on the surface appear as bright protrusions for negative and positive bias voltages [81]. In the same experiment it has been found that oxygen atoms appear always as depressions whether a CO molecule is attached to the tip or not. CO has a wide gap between the highest occupied and the lowest unoccupied molecular states (HOMO and LUMO), while such a gap does not exist with oxygen atoms. In a theoretical work Nieminen et al. [82] considered the influence of different tunneling channels and their interference by use of a scattering approach described by a Green function formalism. They derived an equation taking 5 different tunneling channels into account, which has been independently derived by Todorov [83] and Pendry [84]. The first channel is tunneling through the vacuum incorporating unperturbed states of the tip and sample, the second channel is related to the scattering of electrons by the molecule. The third channel describes a path through the molecule. These three channels determine the tunneling process for the clean metal tip. If a CO molecule is attached to the tip, two further channels have to be considered. The fourth channel takes scattering due to the tip molecule and the fifth channel tunneling through the tip molecule into account. For the clean metal tip on the clean surface only channel one contributes to the tunneling current. On top of the molecule, channel two and three also contribute to the tunneling current. But channel one and three interfere destructively and hence the tunneling current on top of the CO molecule is smaller, since only scattered electrons (channel two) contribute to the tunneling current, compared with the surrounding clean metal area, and thus the CO molecule on the surface appears as a depression. If the tip is functionalized i.e. a CO molecule is picked up, the tunneling current is reduced on the bare metal surface, however, on top of the CO adsorbed on the surface, the additional tunneling channels result in an increase in tunneling current compared with the bare surface and therefore the CO molecule is imaged as a protrusion. For the contrast formation of the oxygen no such straightforward analysis could be found. The hybridization of the 2s and 2p orbitals lead to many channels denoted as channel two and three. This peculiar behavior shows that tunneling current intensities and phases of the tunneling channels play an important role in contrast formation in STM. In addition, the theory applied has to be carefully chosen depending on the system studied.

For thin oxide film theoretical and experimental efforts have been made to understand the contrast formation. The corrugation of thin FeO films has been experimentally investigated and theoretically analyzed by different tip models taking the scattering of tunneling electrons into account [85]. However, the LDOS of FeO is sensitive to the magnetic order of the thin

film, introducing another element of complexity to this system [86]. FeO is a Mott insulator with a band gap of about 2.5 eV [87]. Despite the band gap, at small bias voltages like 50 mV and moderate tunneling currents like 0.3 nA, i.e. small tip surface distances, atomic resolution can be achieved [86, 88]. In this respect the ultra thin alumina film grown on NiAl(110) is an interesting example [89]. The film does not grow thicker than one monolayer. The monolayer consists of an oxide interface layer and a oxide surface layer. Depending on the applied bias voltage and set-point of the tunneling current, either the interface or the surface layer can be imaged, however, in all cases only one species, Al or O, has been imaged. Whether the oxygen or the aluminum is imaged can easily be determined, since their numbers within the unit cell are different [89, 90]. In our workgroup, even a change in contrast and therefore in the layer imaged for the same imaging parameters has been observed. This is a further indication that for this system tip states play an important role and not only scanning parameters. For the MgO system with a one to one stoichiometry it is unclear whether the magnesium or oxygen ions are imaged as bright protrusion. Since these oxide films are insulators with a large band gap it is not obvious from figure 2.11 that the atomic structure of the oxides is visible. However, the scattering mechanism discussed for the adsorbates are also supposed to play an important role in atomic resolution imaging of MgO thin films.

#### 2.4.4 Scanning Tunneling Spectroscopy

For the analysis of surfaces, adsorbates down to single atoms or defects it is often important to gain information about their electronic structure. Since the tunneling current depends on the LDOS of the sample, the states close to the Fermi level can be measured at a fixed  $x, y, z$  position (open feedback loop) while sweeping the bias voltage. This method is commonly known as scanning tunneling spectroscopy (STS). Usually the derivative of the tunneling current with respect to bias voltage ( $dI/dV$ ) is discussed, which is known as the conductivity. At small temperatures  $k_B T \ll eV$  the Fermi-Dirac distribution function in equation 2.34 can be approximated by a step function. For a specific tip-sample state the derivative results in [73]

$$\begin{aligned} \frac{dI_T(eV)}{dV} &= \frac{4\pi e}{\hbar} |M_{TS}|^2 \rho_T(0) \rho_S(eV) + \\ &+ \int_0^{eV} \rho_S(E) \frac{\partial}{\partial V} \left[ |M(E, E - eV)|^2 \rho_T(E - eV) \right] dE . \end{aligned} \quad (2.39)$$

Equation 2.39 shows that the conductivity is not only related to the sample LDOS but also to the tip LDOS. However, in many cases, as shown for a thin alkali halide film, the derivative of equation 2.38 can be applied if an accuracy of a few 10 meV is sufficient [91]. From equation 2.38 follows

$$\frac{dI_T}{dV} \propto \rho_S(E)e^{-2\kappa z} . \quad (2.40)$$

Therefore, with STS band structures can be mapped and thus similar information as provided by UPS is accessible. The advantage of STS is the high lateral resolution. STS measurements can be performed on the atomic scale while UPS measurements always integrate over a large surface area. Angular resolved measurements can resolve the full  $k$  space while with STS angular resolved measurements are not possible. Furthermore, band onsets might be shifted in STS spectra due to the electric field as indicated in figure 2.11 [92–94]. Since the feedback loop is open, experimenters have to choose the swept voltage range carefully. The tip-sample distance will be constant, hence the electric field might become quite large and the tip is likely to be destroyed. Therefore only voltages up to  $\pm 200$  mV should be used. If higher voltages are required, the feedback loop should be closed resulting in a constant tunneling current since the tip-sample distance will be adjusted. Instead of  $dI/dV$ ,  $dz/dV$  is analyzed. Although the energy resolution of  $dz/dV$  is not as high as for  $dI/dV$ , gap states for example can be analyzed and distinguished [95].

### 2.4.5 Field Emission Resonances

Field emission resonances (FER) are a result of matching electron wave functions in a potential created by the tip-sample geometry if high voltages are applied. The voltage applied must exceed the work function (here of the tip). Figure 2.12 shows the potential between tip and sample. After tunneling through the potential barrier the electron propagates as a free particle, being reflected at the boundaries. In the geometry depicted in figure 2.12 the wave functions are to the right bound to the barrier due to the applied field and on the left to the metal sample. At the metal surface, parts of the wave functions are reflected, when a mismatch of the wave functions in the vacuum gap and metal occurs [96].

The reflectance can be constructive or destructive and thus standing electron waves will be formed within the classical region. These so-called field emission resonances have theoretically been predicted by Gundlach in 1966 [97] and are therefore often referred to as Gundlach states. In 1982 Binnig and Rohrer detected these states in STM measurements [96]. As soon as the resonance condition  $eV = E_n$  is fulfilled standing waves will be formed

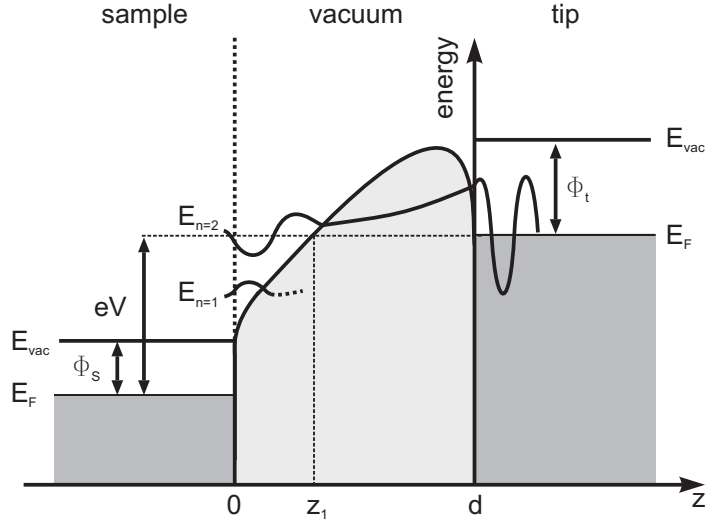


Figure 2.12: Schematic showing the potential between tip and sample for voltages larger than the tip work function. The light gray shaded vacuum region is classically forbidden. Electrons tunneling through this barrier can enter the classical region and form standing waves as they are reflected at the metal surface and the potential barrier originating from the applied bias voltage  $V$ . The edges of the potential barrier are rounded off by the image potential. For  $eV = E_{n=2}$  the electron energy is in resonance with the corresponding eigenstate.

and thus an additional tunneling channel is created, leading to an increase in tunneling current. This regime is also known as the Fowler-Nordheim regime. A typical example showing the differential gap conductivity is given in figure 2.13. The amplitude decreases with increasing energy. The reflectivity at the sample surface decreases with increasing energy exponentially. Therefore the electron lifetime decreases with increasing resonance number i.e. higher energies. The lifetime can be approximated by the Heisenberg uncertainty principle  $\Delta t \approx h/\Delta E$ , with  $\Delta E$  as the FWHM of the conductance peak. Typical lifetimes are in the order of femtoseconds. If a state decays the energy can be transferred to a photon, which then can be detected (photon STM) [98].

However, at low temperature the field emission current is given by [99]

$$I(V) = \frac{em}{2\pi^2\hbar^3} \int_0^{E_F} (E_F - E) T(E, V) dE \quad (2.41)$$

with  $T(E, V)$  as the transition probability, and  $V$  represents the bias

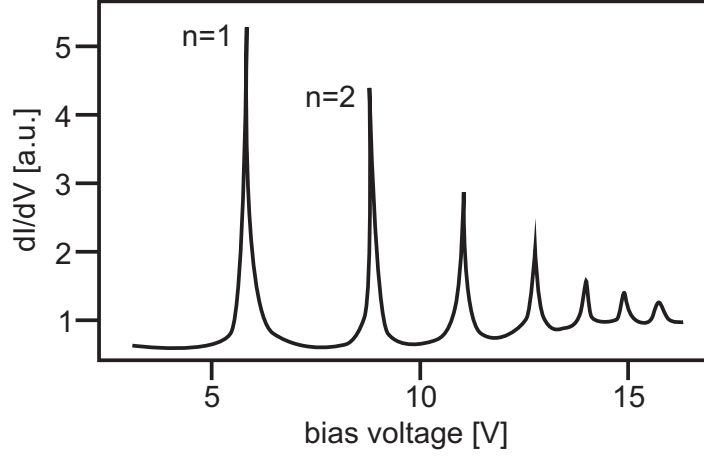


Figure 2.13: Example of field emission resonances. The resonance number  $n$  is indicated for the first two resonances. The amplitude of conductance decreases to a reduction of reflectivity with increasing bias voltage i.e. energy.

voltage. The Wentzel-Kramers-Brillouin (WKB) method describes  $T(E, V)$  only in the regime from  $z = 0$  to  $z = z_1$ . Gundlach also derived an expression for  $T(E, V)$  in the regime  $z_1 < z < d$ . Within this classical regime  $T(E, V)$  shows a sinusoidal behavior and the tunneling current results in

$$I(V) = I_{FN} \sqrt{\frac{eV + E_F}{eV - \Phi_S}} \left[ 1 - \frac{1}{2} \frac{(E_F + \Phi_S) \Phi_t \sqrt{E_F + eV}}{(eV - \Phi_S)^{5/2}} \sin(\alpha + \beta) \right] \quad (2.42)$$

with  $I_{FN}$  as the Fowler-Nordheim equation [99–101]

$$I_{FN} = \frac{\sqrt{E_F/\Phi_t}}{E_F + \Phi_t} \frac{e\epsilon^2}{4\pi^2\hbar} \exp \left\{ -\frac{4}{3} \left( \frac{\Phi_t}{e\epsilon l} \right)^{3/2} \right\} \quad (2.43)$$

with  $\epsilon$  as the electric field and

$$\alpha = \frac{4}{3} \left( \frac{eV - \Phi_S}{e\epsilon l} \right)^{3/2}, \quad \sin \beta = 2 \frac{\sqrt{\Phi_t(eV - \Phi_S)}}{eV + \Phi_t - \Phi_S}, \quad l = \left( \frac{\hbar^2 d}{2m(eV + \Phi_t - \Phi_S)} \right)^{-3}.$$

The derivative of equation 2.42 leads to the differential gap conductivity [99]

$$\frac{dI}{dV} = 2 \left( \frac{\Phi_t}{e\epsilon l V^{2/3}} \right)^{3/2} I_{FN} \left( 1 - \frac{E_F + \Phi_S}{4\sqrt{\Phi_t eV}} \cos \left[ \frac{4(eV - \Phi_S)}{3e\epsilon l} \right] \right). \quad (2.44)$$

The oscillatory behavior in the classical regime is given by the cosine-term in equation 2.44. Thus the condition for a maximum to occur in the conductance is determined by the cosine-term [99]

$$\frac{4}{3} \frac{\sqrt{2m}}{\hbar} \frac{(eV_n - \Phi_S)^{3/2}}{e\epsilon} = 2\pi \left( n + \frac{1}{4} \right), \quad (2.45)$$

with  $V_n$  as the voltage of the  $n$ -th resonance. If the feedback loop of  $I$  is closed during the measurements the tunneling current will be constant and thus the effective electric field can be considered as constant as usually assumed in STM measurements. Approximating  $(n + 1/4)^{2/3} \approx n^{2/3}$  results in

$$E_n = eV_n = \Phi_S + \left( \frac{3\pi\hbar e}{2\sqrt{2m}} \right)^{2/3} \epsilon^{2/3} n^{2/3}. \quad (2.46)$$

The tip-sample geometry is three-dimensional. Within the approximations made the tip-sample geometry has been assumed to be one-dimensional. Due to the exponential dependence of the tunneling probability on the barrier width, the tunneling current is mainly determined by the region with the smallest gap. This reduces the geometry to a quasi-one-dimensional gap. Furthermore image potential effects have not been taken into account. The image potential rounds off the corners of the potential as visualized in figure 2.12, therefore the resonances are shifted to lower energies. Including the image potential into the Schrödinger equation makes an analytical solution of the problem impossible [99]. The image potential modifies the Fowler-Nordheim equation to [101]

$$I_{FN} = \frac{4}{3} \frac{16\pi m e (E_F/\Phi_t)^{1/2}}{h^3 (E_F + \Phi_t) \gamma^2} \epsilon^2 \exp \left( -\frac{\Phi_t^{3/2} \gamma}{\epsilon} \right), \quad (2.47)$$

where  $\gamma = 6.8 \cdot 10^7 \left( 1 - 3.8 \cdot 10^{-4} \frac{\epsilon^{1/2}}{\Phi_t} \right)^{1/2}$  is a correction factor. However, the image potential mainly affects resonances with small  $n$  [97, 99]. A prerequisite is a stable tip since instabilities will effect the electric field  $\epsilon$  between tip and sample and thus the potential within the vacuum gap. In addition the work function of the tip  $\Phi_t$  will be modified if tip changes occur. If thin oxide films are grown on top of the metal sample these films are an additional barrier for the tunneling current. Thus the tunneling current will be reduced due to effects discussed in section 2.4.3. Since the metal substrate dominates the tunneling process the above discussed wave function matching conditions have still to be fulfilled. Within the presented model of the tip-sample tunneling junction a good estimation of the sample work function can be found for resonances  $n \geq 2$  as has been shown for FeO on Pt(111) [88].

# Chapter 3

## MgO on Ag(001)

In the following chapter the properties of MgO will be discussed. The discussion will start with an overview of bulk MgO, followed by thin MgO films grown on Ag(001) and a comparison between the two.

### 3.1 General MgO Aspects

Magnesium oxide is a wide band gap and ionic oxide with a rocksalt structure. Due to its simple structure and high dielectric constant it recognizes high attention in many research fields. MgO is for example used in sandwich structures of magnetoresistance devices [102–104]. In the research field of heterogeneous catalysis it is used as a support for catalytic particles and clusters as well as a bare oxide [1, 105–112]. The surface chemistry is believed to be dominated by the defects present on the surface. The pristine MgO surface is quite inert while the defect rich MgO surface shows a complex surface chemistry [2, 113]. Great attention was paid to defects with a high electron affinity and thus acting as electron traps in a number of theoretical [114–118] as well as experimental studies [95, 119–122]. The defects can act as nucleation centers [116, 123–125] and as electron donor sites which enhance the chemical activity of deposited metal clusters [126, 127]. However, the role of color centers in catalytic cycles is still being discussed [128] and has not yet been completely understood. The development of knowledge about insulating oxides surfaces enormously benefited from the possibility to grow thin films reactively on metal substrates. Due to the metal support beneath these thin films, charging effects are prevented during spectroscopic measurements such as LEED or XPS. The film thickness has been recognized as an important parameter to tune properties of the thin films as well as properties of adsorbates [110, 129–131].

## 3.2 MgO Properties

The magnesium oxide system Mg-O is known in mineralogy as periclase. The phase diagram of this system (figure 3.1), including the gas phase and taking into account the oxygen solubility in liquid Mg, has been derived from calculations of Gibbs free energy [132]. A general experimental verification of the phase diagram has not been presented so far. However, the melting point of stoichiometric MgO has been experimentally confirmed [133]. Stoichiometric  $\text{Mg}_1\text{O}_1$  is the only stable compound over a wide temperature range [134, 135] with a melting point at  $T_L = 3100$  K (compare figure 3.1). Nevertheless, magnesium oxides with higher oxygen content like magnesium peroxide exist [135–137].

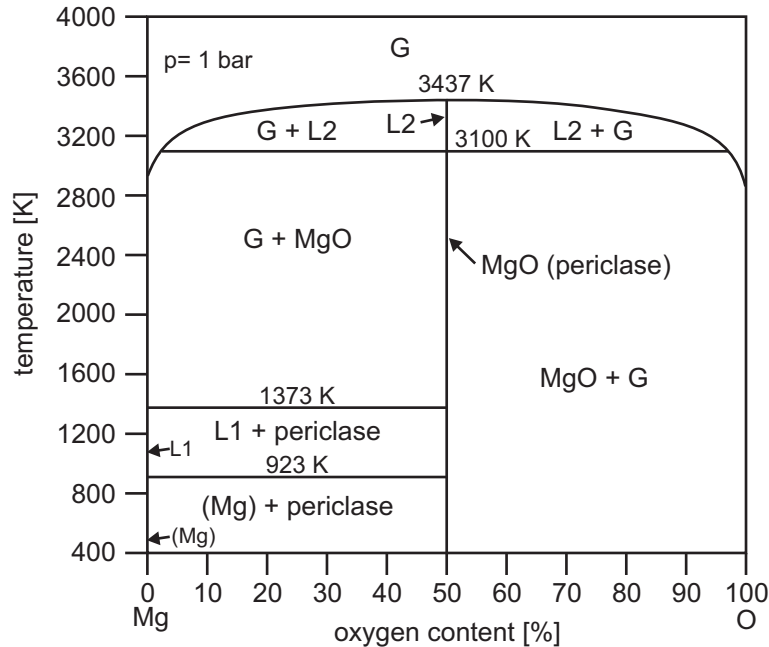


Figure 3.1: Phase diagram of MgO at 1 bar [132]. L1 refers to liquid Mg, L2 to liquid MgO and G to the gas phase. The gas phase is assumed to consist of Mg,  $\text{Mg}_2$ , MgO, O,  $\text{O}_2$  and  $\text{O}_3$  [134]. The pure Mg has a hcp structure, a melting point at  $T_L = 923$  K and a boiling point at  $T_B = 1373$  K.

MgO has been found to be stable up to a pressure of 227 GPa at room temperature demonstrating its remarkable structural strength [138]. This strength is related to the highly ionic rocksalt NaCl (B1) structure due to the large differences in electronegativity of Mg (1.31) and O (3.44). The Mg ( $1s^2 2s^2 2p^6 3s^2$ ) is oxidized to  $\text{Mg}^{2+}$  and O ( $1s^2 2s^2 2p^4$ ) is reduced to  $\text{O}^{2-}$ , thus the two Mg  $3s^2$  electrons are transferred to the O  $2p$  orbital. These findings

have direct consequences for the geometric and electronic structure of bulk MgO and its surface. In the rocksalt NaCl (B1) structure each anion/cation is coordinated by 6 cations/anions forming an octahedral configuration as shown in figure 3.2. One should note that the "free"  $O^{2-}$  anion does not exist, because it is unstable by 7.5 eV unless it is stabilized by surrounding positively charged ligands [139].

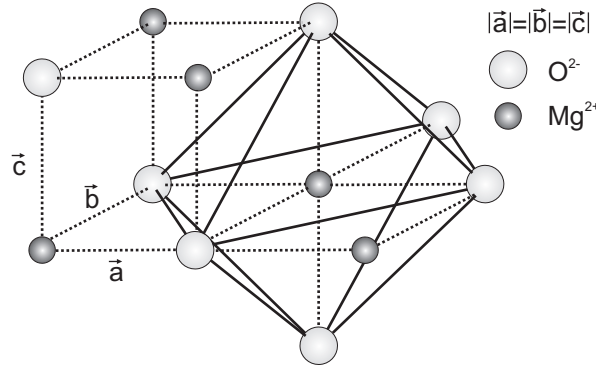


Figure 3.2: Ball-structure model of the MgO lattice. Dashed lines indicate the rocksalt structure while solid lines stress the octahedral configuration.

The structure is driven by Coulomb forces, which are large and long range in character leading to local charge neutrality [139]. The forces arise from the gradient in the Madelung potential [140], which does not only affect the geometrical structure but also the electronic properties of MgO (of course geometric and electronic properties are strongly connected). The interaction potential of the  $i$ th ion with all other ions can be outlined as [141]

$$U_i = \sum_j \underbrace{\lambda e^{-r_{ij}/\rho}}_{\text{repulsive pot.}} \pm \underbrace{\frac{1}{4\pi\epsilon_0} \frac{q^2}{r_{ij}}}_{\text{Coulomb pot.}} \quad (3.1)$$

where  $\lambda$  is the strength and  $\rho$  the decay length of the repulsive interaction. The positive sign is taken for like charges and the negative sign for unlike charges. Neglecting surface effects and applying basic mathematics lead for a crystal with  $2N$  ions to a total lattice energy of

$$U_{tot} = NU_i = \underbrace{-\frac{N\alpha q^2}{4\pi\epsilon_0 R_0}}_{\text{Madelung pot.}} \left(1 - \frac{\rho}{R_0}\right). \quad (3.2)$$

With  $R_0$  being the equilibrium separation of neighboring ions. The attractive Coulomb interaction is known as the Madelung potential  $E_M$  and  $\alpha$  as the

dimensionless Madelung constant given by

$$\alpha = \sum_j \pm \frac{R_0}{r_j}. \quad (3.3)$$

By knowing the Madelung constant  $\alpha$  and the equilibrium separation  $R_0$  it is possible to calculate the Madelung potential. However, this holds only true for anions and cations occupying equivalent lattice sites as in a rocksalt structure. For a stable ion crystal the Madelung constant has to be positive. For the NaCl structure the Madelung constant is  $\alpha = 1.747565$  [141, 142]. Using an advanced summation method developed by Ewald [143] it is possible to determine quite accurate Madelung energies comparable to values derived from XPS measurements (Bagus et al. [144]). The Madelung energy  $E_M$  of MgO per ion is [142, 144]

$$\frac{E_M}{2} = \pm 23.9 \text{ eV}, \quad (3.4)$$

where the plus applies for anions the minus for cations. However, the band gap energy of MgO cannot be estimated from the Madelung potential alone [145]. The electrostatic polarization is an important quantity. The electron distribution is distorted leading to a reduction of the band gap. The polarization effects on the band gap can be estimated from continuum electrostatic models or shell model calculations. Moreover, the overlap of neighboring ion orbitals has to be taken into account, reducing the band gap further [compare figure 3.3(a)]. These considerations lead to a bulk band gap of about 7.8 eV [145–149] as shown in figure 3.3(a,b). The valence band is predominately O  $2p$  in character while the conduction band is determined by the Mg  $3s$  orbital [145, 148, 150, 151] [figure 3.3(c)].

The band gap is affected by the presence of the surface. Due to the change in coordination number and equilibrium positions of the ions, the Madelung potential decreases. These findings together with the polarization of the surface ions wave functions, due to the change in surface potential, reduce the band gap at the surface to about 6.7 eV [95, 149, 151, 152]. Despite the lower coordination of the  $\{001\}$  surface ions and those located at steps, they can be considered as  $\text{Mg}^{2+}$  and  $\text{O}^{2-}$  ions [139, 151]. Oxide surfaces with at least two different species bear charges of opposite sign. They can be classified on the basis of electrostatic criteria as described by Tasker [153].

**Type I surfaces:** All planes parallel to the surface are electrically neutral. This is true for the  $\{001\}$  and  $\{110\}$  face of rocksalt crystals, since each layer contains as many anions as cations.

**Type II surfaces:** In many oxide surfaces the atomic layers are not neutral. But the stacking sequence may be such that the total dipole moment of each unit vanishes.

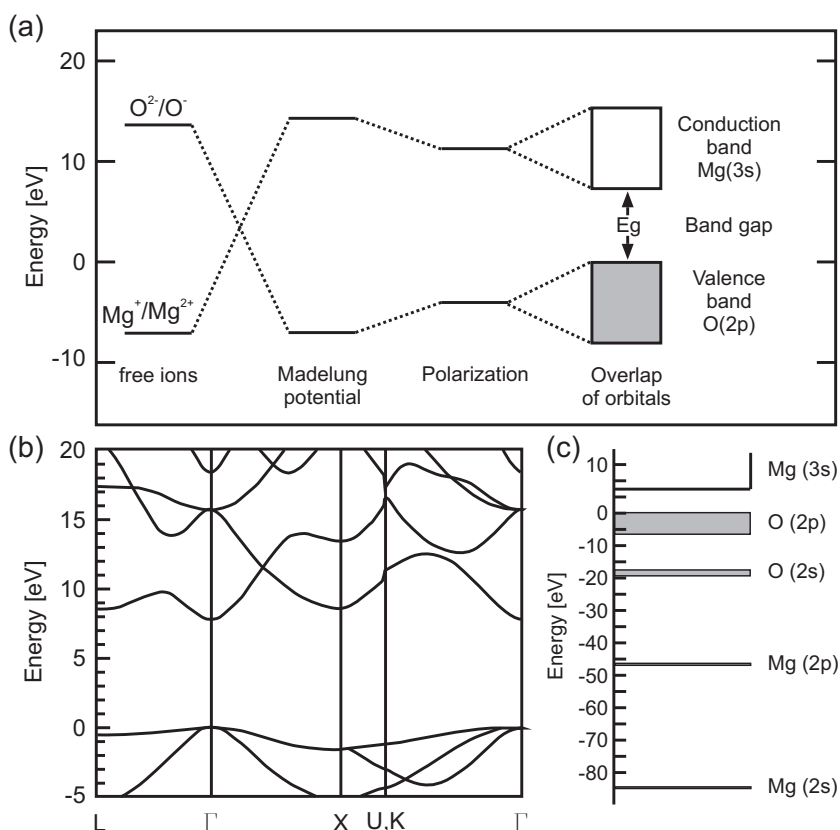


Figure 3.3: (a) Valence and conduction band energies in MgO [145]. Compared with the original figure the zero energy level has been aligned with the top of the valence band. (b) Calculated band structure of MgO along high symmetry lines [150]. (c) Approximated energy level diagram for MgO, based on XPS [151].

Type III surfaces: The layers are not electrically neutral and the stacking results in a non-zero dipole moment.

The three different types are presented in figure 3.4. The charge of each layer is represented by  $Q$ . For an equal number of anions and cations within a layer  $Q$  becomes zero.  $\mu$  stands for the net dipole moment for each unit as indicated.

The MgO {001} and {110} surface belongs to type I while the {111} is unstable in vacuum due to the dipole moment. However, in nature (ambient conditions) minerals need not be in equilibrium, since they might be solified from water or from a matrix. Interfacial energies are then important not the *pure* surface energy alone. Therefore, MgO (periclase) can be found with {111} faces [154]. For the rocksalt structure with one broken bond per

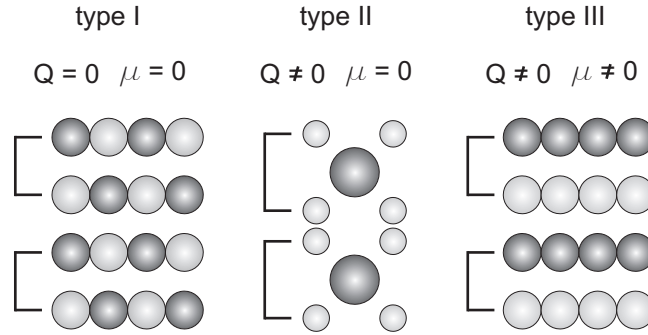


Figure 3.4: Separation of insulating surfaces into categories according to Tasker [153].  $Q$  and  $\mu$  represent, respectively, the charge of each layer and the net dipole moment of each unit as indicated.

surface atom the  $\{001\}$  surface is most stable, while the  $\{110\}$  and  $\{211\}$  surfaces with two and four broken bonds, respectively, have higher surface energies. Therefore, the MgO cleaves extremely well along the  $\{001\}$  planes [145]. Since the surface atoms are lower coordinated, the surfaces relax inward (i.e. the spacing between the surface layer and the layer beneath decreases) by an average value of  $-0.56 \pm 0.5 \%$  compared with the bulk lattice constant. However, anions are less affected than cations. This leads to a surface rumpling of  $1.07 \pm 0.5 \%$  as has been determined by grazing incident x-ray scattering [155].

### 3.3 Characteristics of MgO Thin Films on Ag(001)

The epitaxial growth of MgO thin films on metals depends strongly on the lattice mismatch of MgO and metal support. MgO thin films are mainly deposited on Ag(001) (nearest neighbor distance  $d_{Ag-Ag} = 289$  pm), Au(001), Fe(001) and Mo(001)[156] resulting in lattice mismatches of 2.9 % [157, 158], 3.1 % [158], 3.7 % and 5.4 % [156], respectively. Better matching conditions were obtained for alloys e.g.  $Cr_{0.7}Mo_{0.3}(001)$  with negligible misfit [159]. Lattice mismatches as in the case of MgO on Mo lead to line dislocations aligned along the  $[110]$  direction and screw dislocations, which compensate with increasing film thickness [160]. To minimize substrate induced epitaxial effects MgO has been grown on Ag(001). MgO grows on Ag(001) (which is face centered cubic) in the Frank-van-der-Merve growth mode [109, 161]. The oxygen anions are located on top sites and magnesium cations in four fold hollow sites with respect to the Ag layer as derived from LMTO [157]

and DFT [162, 163] calculations. This is of course in line with calculations done by Smoluchowski presented in 1941 [164]. He showed that the electron gas of clean metals tend to move into the *holes* between the surface atoms. Therefore cations will prefer these sites.

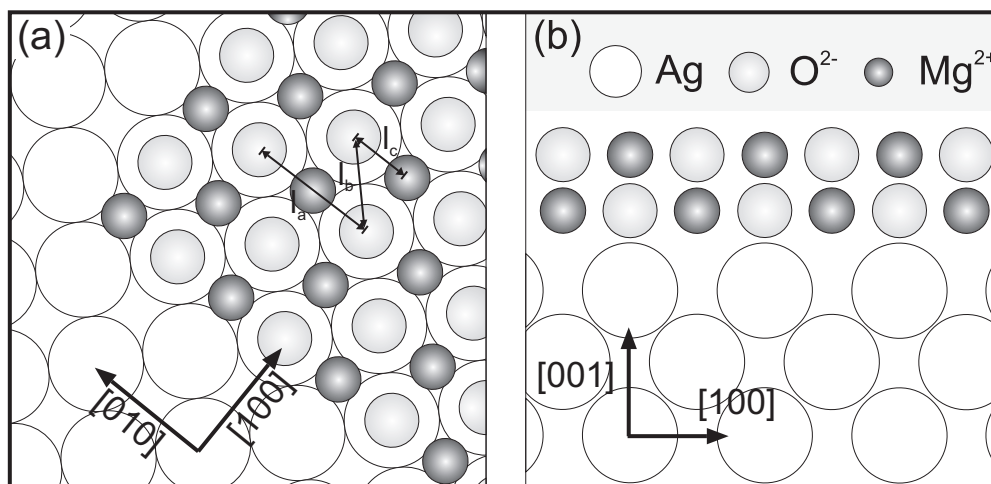


Figure 3.5: Growth model of MgO (rocksalt, B1) on fcc Ag(001). The oxygen atoms adsorb on top of the silver atoms while magnesium prefers hollow sites. (a) Top view,  $l_a = 408$  pm is the Ag unit cell length [165],  $l_b = 289$  pm is the nearest neighbor distance of Ag and  $l_c = 204$  pm is the Mg-O bonding distance. (b) Side view of the growth model.

The overlayer-surface interfacial distances are  $2.55 \text{ \AA}$  for the oxygen anion and  $2.46 \text{ \AA}$  for the magnesium cation as calculated by DFT [166]. One has to note that the mean calculated interface distances range from  $2.39 \text{ \AA}$  [162, 163] to  $2.5 \text{ \AA}$  [166] and  $2.62 \text{ \AA}$  [129] depending on the code used for the calculations. This shows that the derived values may differ considerably, however trends are consistent. Experimentally interface distances of  $2.53 \pm 0.05 \text{ \AA}$  and  $2.39 \pm 0.06 \text{ \AA}$  have been found by EXAFS [167] and LEED [163], respectively. The rumpling of the single MgO monolayer of almost  $0.1 \text{ \AA}$  results from releasing some of the energy arising from film compression due to the smaller Ag lattice constant. For a second MgO layer present, the interface rumpling decreases and only a value of  $0.03 \text{ \AA}$  between anion and cation positions remains (see table 3.1) [166]. The corrugation due to the rumpling is still present within the second layer as can be seen in table 3.1. Compared with bulk MgO the average bilayer distance is elongated by about 3 % [166]. Rumpling as well as elongation effects are expected to decrease with increasing MgO layers adsorbed. The topmost Ag layer is also affected by the MgO overlayers. Their positions change by  $-0.027 \text{ \AA}$  and  $-0.055 \text{ \AA}$  with one

Table 3.1: MgO layer distances with respect to the Ag(001) surface.  $N$  represents the number of MgO layers. Index  $i$  stands for the layer in contact with the metal, while  $s$  stands for the surface MgO layer. As discussed in the text the calculated values vary with the code used for the calculation. However, trends are generally observed. Data have been taken from Ref. [166].

$N$	$z_{Ag}$ [Å]	$z_{O_i}$ [Å]	$z_{Mg_i}$ [Å]	$z_{O_s}$ [Å]	$z_{Mg_s}$ [Å]
1	-0.027	2.546	2.455	-	-
2	-0.055	2.472	2.446	4.644	4.607

and two MgO overlayers present compared with the uncovered and relaxed Ag surface respectively. Interesting is the bonding and the related electronic structure of the inert oxide noble metal interface. The bonding mechanisms and the related electronic structure of the MgO/AgO(001) interface have been studied by many different surface science techniques including LEED [156], HREELS [156], UPS [168], XPS [168], AES [168], TPD [156] and STM in combination with STS [149]. Beside these experimental investigations theoretical calculations have been performed to clarify and understand the decisive parameters determining the interface [149, 157, 161–163, 166, 168]. The lowest ionization states of MgO are mainly O  $2p$  in character. Therefore, the contribution to the interaction is expected to result from O  $2p$  with Ag  $4d$  and Ag  $5sp$  orbitals.

However, from a series of XPS measurements it is concluded that the O  $2p$  states hybridize strongly with the Ag  $5sp$ , in contrast to a weak interaction with the Ag  $4d$  states [168]. The hybridization of the O  $2p$  states with the Ag  $5sp$  states is supposed to push the oxygen density of states all the way up to the Fermi level [157, 161, 166], which is not the case with unsupported MgO. These states are often referred to as metal induced gap states (MIGS) and are a general feature of metal-oxide interfaces [142, 169, 170].

MIGS result predominantly from the metal-oxide interface, because calculations show that the second oxide layer does not contribute to the MIGS [149]. Thus experimental results and theoretical calculations seem to support each other. The MIGS as they are in the band gap, have a characteristic damping length [170]. At midgap the damping reaches its maximum. Assuming an exponential damping the charge density can be expressed as  $\rho(z) = \alpha \exp(-2kz)$  with  $k$  being the decay length of charge density  $\alpha$  [161]. For  $k$  a value of  $0.84/d$  has been derived with  $d$  being the interplanar dis-

tance [161]. Assuming a mean interplanar distance of Mg and O atoms of 2.50 Å,  $k$  results in 0.34 Å. With increasing film thickness the MIGS should therefore not be present at the surface. The valence band of a monolayer grown on Ag(001) is of O  $2p$  character while the conduction band is mainly Mg  $3sp$  determined [149, 157, 166]. The electronic structure of MgO thin films is established with the second to third monolayer present on the surface [52, 129, 149, 161, 162].

These findings about the electronic structure at the interface lead to weak electrostatic bonding of MgO(001) on Ag(001) [129, 157] as expected for an inert oxide grown on a noble metal. In table 4.1 (see chapter 4) adhesion energies per interface area ( $E_{adh}/S_{int}$ ) for different numbers of MgO layers on Ag(001) are presented and compared with MgO layers on Mo(001). With only one layer present the adhesion energies at the interface are at their maximum while with two MgO layers present the adhesion energies decrease and stay constant from three layers onwards. However, the adhesion energy per interface area for 3 ML MgO/Mo(001)  $E_{adh}/S_{int} = 0.136 \text{ eV}/\text{Å}^2$  is about 6 times larger than for 3 ML MgO/Ag(001)  $E_{adh}/S_{int} = 0.023 \text{ eV}/\text{Å}^2$ . The influence of the adhesion energy on the work function will be discussed in chapter 4.

### 3.4 Defects in MgO

Defects present at a surface decisively determine the properties of the surface. In particular point defects determine the optical, electronic and transport properties as well as the chemical activity of the surface [2]. This is in particular interesting in the research field of heterogenous catalysis. Here oxides are often used as support or directly as a catalyst.

In the case of MgO the perfect single crystal surface is quite inert, but a defect rich MgO surface shows a high and complex chemical reactivity [2, 115, 171–174].

Most chemical reactions are determined by electron-electron interaction or electron exchange. It has been experimentally observed and supported by theory that metal clusters of Au and Pd deposited on defect rich MgO films are catalytically more active than clusters deposited on defect poor films [126, 127, 175, 176]. The defects have two important roles: They provide adsorption sites and are therefore nucleation centers [123–125, 177, 178] and they can act as electron donor or acceptor sites. The major irregularities present on the MgO surface are the following [2, 172]:

- *Low coordinated cations.* These are  $\text{Mg}^{2+}$  ions with a lower coordination number than on the flat (001) surface. Therefore, four-coordinated ions

located at steps and edges,  $\text{Mg}_{4c}^{2+}$  and three-coordinated ions located at kinks and corners, etc.  $\text{Mg}_{3c}^{2+}$ .

- *Low coordinated anions.* These are  $\text{O}^{2-}$  ions with a fourfold coordination  $\text{O}_{4c}^{2-}$  like at steps and edges and threefold coordinated ions located at corners and kinks, etc.  $\text{O}_{3c}^{2-}$ . The chemical properties of the low coordinated oxygen ions strongly depend on their coordination.
- *Divacancies.* These defects are created by removing a neutral MgO unit, therefore the generated defect is also neutral. A divacancy created at a step leads to three- and fourfold coordinated surface ions.
- *Hydroxyl groups.*  $\text{H}_2\text{O}$ , which to a certain amount is always present in UHV chambers, easily reacts with low coordinated sites leading to OH groups present at the surface of MgO. These centers are possible nucleation sites for metal particles and other adsorbates.
- *Oxygen vacancies.* Commonly called color centers or F centers from the german word *Farbe*. The reason for this nomenclature comes from the adsorption of light in the visible region. Therefore, MgO with a high defect concentration has a different color [117]. The F centers can be charged differently. By removing an  $\text{O}^{2-}$  ion a positively charged  $\text{F}^{2+}$  vacancy is formed. It can trap one electron resulting in an  $\text{F}^+$  or two electrons resulting in a neutral  $\text{F}^0$  vacancy. However, their exact creation pathway is still discussed and different mechanisms are supposed [122]. The  $\text{F}^+$  center is paramagnetic.
- *Cation vacancies.* Cation vacancies are related to the removal of Mg,  $\text{Mg}^+$ , or  $\text{Mg}^{2+}$  species resulting in  $\text{V}^0$ ,  $\text{V}^-$  and  $\text{V}^{2-}$  defects. The  $\text{V}^0$  and  $\text{V}^-$  centers are paramagnetic.
- *Impurity atoms.* Beside the possibility to substitute transition metals into the MgO matrix a very effective way to create highly reactive  $\text{O}^-$  ions is to substitute divalent  $\text{Mg}^{2+}$  ions by monovalent  $\text{Li}^+$ . The  $\text{O}^-$  ion is a paramagnetic center.

Figure 3.6 shows a schematic of a MgO(001) surface with differently coordinated surface sites.

The concentration of the defects on the MgO(001) surface is quite small  $10^{16}$  to  $10^{18}$  defects/cm<sup>2</sup> [2]. One might expect an increase in defect concentration induced by the growth process during the reactive deposition of Mg in an oxygen background pressure. The stress induced defect formation is not significant with Ag(001) as a support [118]. The number of defects

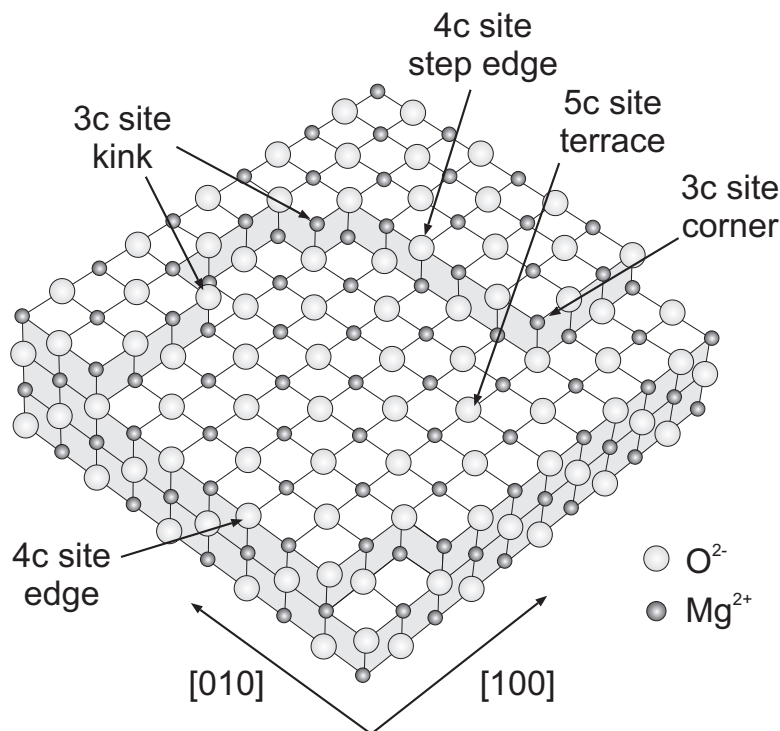


Figure 3.6: The MgO(001) surface with differently coordinated surface sites and the corresponding nomenclature.

present on the surface can be increased by bombarding the surface with electrons released from a filament or by scanning the surface at high voltages and currents generating tip induced defects. The latter method is applied in this study. Typical voltages are  $U_S = 7$  V and currents of  $I_T = 6$  nA.

In the following the discussion will be focused on morphological defects like low coordinated sites, divacancies and color centers. These defects are preferentially created at low coordinated sites such as steps and corners, since formation energies are smaller at these positions [114, 179]. The energy required to generate an oxygen vacancy cannot easily be measured. However, it has been calculated by different approaches. Plane wave density functional calculations in the local density approximation (LDA) result in 10.5 eV for removing an oxygen atom from bulk (sixfold coordinated), 9.8 eV for removing an oxygen atom from the surface (fivefold coordinated) [114]. From plane wave gradient corrected DFT a value of 9.48 eV has been computed as the energy to remove an oxygen atom from the surface [118] with a cluster approach a formation energy of 9.07 eV has been derived [180]. The formation energy is reduced to 9.0 eV and 8.1 eV for low coordinated oxygen ions at a

step edge (fourfold coordinated) and at a corner site (threefold coordinated), respectively [114]. The same trend (9.7, 8.1, 6.9, 5.6 eV for bulk, surface, step edge, corner) has been computed by Hartree Fock calculations [179]. The values derived by Hartree Fock calculations are lower compared with the DFT calculations because of the absence of correlation effects. However, LDA is known to overestimate bond strength. The formation energy for neutral vacancies follows the trend: bulk and subsurface > surface > step > corner. Moreover, the Hartree Fock calculations [179] show the following trend in stability:  $F^0 > F^+ > F^{2+}$  independent of the coordination. This trend can be explained by the electronic structure of the defects. The electrons of the  $F^0$  interact with the Madelung potential of the crystal and stabilize the defect [179]. With a decreasing number of electrons the defects become less stable, explaining the observed stability trend [172]. One might expect that the electrons in the  $F^0$  and  $F^+$  color centers belong to one or more  $Mg^{2+}$  ions of the cavity changing their oxidation states while being delocalized over the 3s level of one or several  $Mg^{2+}$  ions of the cavity. This is not the case. The electrons of the  $F^0$  and the electron of the  $F^+$  color centers are located within the center of the cavity formed by the surrounding  $Mg^{2+}$  ions [118, 181, 182]. Charge density distribution plots will be shown and discussed in chapter 5.

Divacancies have also been found to be quite stable and are energetically less costly (formation energy terrace: 13.4 eV, step: 10.8 eV [183]) than a pair of isolated anion and cation vacancies [172, 184]. The recombination of isolated vacancies results in an energy gain of up to 12 eV [2]. The stability of the divacancy at the surface is higher than in the bulk, therefore a migration to the surface is expected at high temperatures. A divacancy has an electron affinity of about 1 eV and can become a paramagnetic center. For a second electron the affinity becomes negative and is thus not expected to be stable [184].

The ionization potential of color centers have been calculated by DFT [180] and Hartree-Fock [179, 185]. All the calculations that consider the ionization energy (IE) of a corner, a step, the surface and bulk show the following trend:  $IE(\text{corner}) > IE(\text{step}) > IE(\text{surface}) > IE(\text{bulk})$  (compare table 3.2). This trend is not obvious. Based on an electrostatic argumentation one would expect that the IE is inversely proportional to the electrostatic potential. Neglecting geometric relaxation, the electrostatic potential is directly related to the Madelung constant which is smaller at low-coordinated sites, in contrast to what was found for the IEs. The trend is not completely described by electrostatics. The difference can be explained by considering the spatial extent of the O 1s orbitals and comparing it with the electrons trapped at an  $F^0$  center [179]. The core orbitals are very much contracted by the strong nuclear potential while the trapped electrons in an  $F^0$  center are

much more diffuse and interact with the neighboring ions [179]. This interaction, although it is weak, gives rise to a Pauli repulsion, which is stronger for high coordinated F centers and decreases for low-coordinated defects where the electrons can extend towards the vacuum [179]. Table 3.2 shows the ionization energies, relaxation energies and electron affinities calculated by DFT [180] for different charge states of the F center situated at a terrace and at an anion corner of MgO.

Table 3.2: Ionization (IE) and relaxation energies (RE) and electron affinities (EA) of different charge states of the anion vacancy at a terrace and at an anion corner of MgO [180].

Notation (see fig.3.7)	Process	Terrace [eV]	Corner [eV]
IE(v)	$F^0 \rightarrow F^0 - e^-$	3.4	3.4
RE	$F^0 - e^- \rightarrow F^+$	0.9	0.6
IE(v)	$F^+ \rightarrow F^+ - e^-$	5.6	6.6
RE	$F^+ - e^- \rightarrow F^{2+}$	1.1	0.8
EA(v)	$F^{2+} \rightarrow F^{2+} + e^-$	3.4	5.0
EA(r)	$F^{2+} \rightarrow F^+$	4.5	5.8
EA(v)	$F^+ \rightarrow F^+ + e^-$	1.7	2.3
EA(r)	$F^+ \rightarrow F^0$	2.6	2.8

The notation in table 3.2 is explained in figure 3.7. IE(v) represents the energy required for a 'vertical' ionization, followed by the energy gain due to relaxation effects RE. EA(v) shows the 'vertical' affinity for fixed nuclei positions around the cavity and EA(r) the affinity of a completely relaxed structure. The data in table 3.2 shows the already discussed trend of the ionization energy. Moreover, electrons associated to low-coordinated oxygen vacancies are more strongly bound than in the corresponding high-coordinated vacancies. The lattice surrounding the defect relaxes due to the absence of an anion. This relaxation process has been analyzed in a number of theoretical studies [118, 172, 179–182, 186]. All these studies have in common that the  $Mg^{2+}$  ions move outward and the  $O^{2-}$  ions move inward with respect to the center of the defect [see figure 3.8(a,b)]. The relaxation effects increase with the number of electrons trapped decreasing. For an  $F^0$  color center at the surface the relaxation is the smallest, about 3 % [118] compared with the pristine surface Mg-O bonding distance. For the  $F^+$  color center the relaxation increases to about 6-7 % [118] and for the  $F^{2+}$  to about

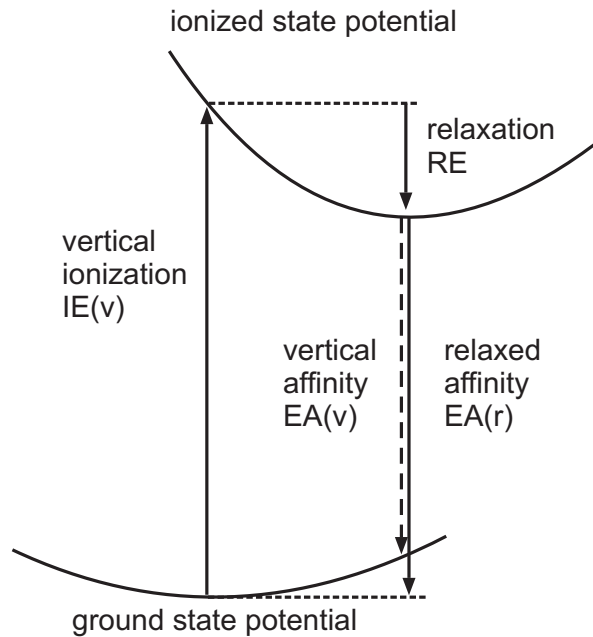


Figure 3.7: Schematic explanation of the notation used in table 3.2 for the ionization (IE) and relaxation energies (RE) as well as electron affinities (EA). Reproduced from Ref. [180].

10 % [172, 181]. The relaxation effects increase slightly when the defects are located at steps or corners [118]. The relaxation of the neutral divacancy is comparable to the  $F^0$  center while it is almost absent for the negatively charged divacancy [184].

For the diffusion of color centers or oxygen ions both have to interchange their position. The barrier that has to be overcome depends on the charge state of the color center involved. For the  $F^0$  and the  $F^+$  centers the diffusion barriers are higher than for an  $F^{2+}$  center. The reason is that the interaction of the trapped electrons lead to a repulsive interaction with the charge of the oxygen ion [179]. This results in the following trend for the diffusion barrier (DB) of an oxygen ion and the corresponding vacancy [179, 187]:  $DB(F^0) > DB(F^+) > DB(F^{2+})$ . Thus it is usually assumed that the  $F^{2+}$  centers are involved in the ion migration and therefore in ion conductivity [188, 189]. For the diffusion of a sub-surface  $F^{2+}$  vacancy to the surface a barrier of 2.9 eV has been derived by Hartree-Fock calculations [179]. The barrier for an oxygen ion migrating from one terrace site to another terrace site is about 1.6 eV, while it results in 0.7 eV for the migration from a step site to a terrace vacancy [179]. Thus an  $F^{2+}$  center preferentially migrates in the other direction from a high-coordinated to a low-coordinated surface

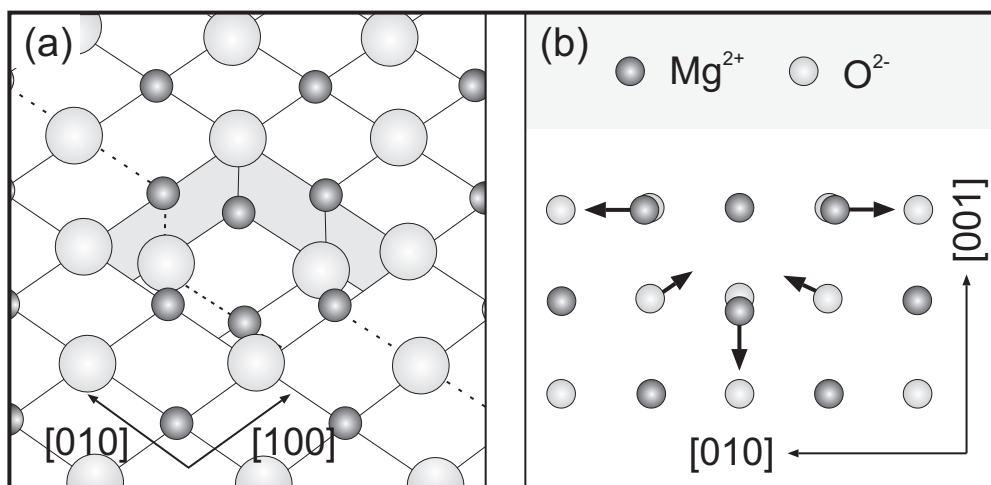


Figure 3.8: (a) Oxygen vacancy at the MgO(001) surface. (b) Cut through a defect along the dashed line indicated in (a). The arrows indicate the lattice relaxation directions for Mg<sup>2+</sup> and O<sup>2-</sup> ions. Magnesium ions relax outwards while oxygen ions tend to relax inwards with respect to the vacancy center [118]. For a better visualization the anions and cations have the same size.

site. The diffusion pathway of an oxygen ion diffusing from a filled to a vacant site on the (001) surface follows a curved trajectory. At midpoint it is 0.6 Å above the surface [179]. With increasing temperature the thermal energy increases and the diffusion barriers are more likely to be overcome. Thus at high temperatures the oxygen ions migrate from low-coordinated sites to high-coordinated vacancies leaving a higher vacancy concentration at the surface, step and corner sites [179].

From the argumentation of charge neutrality one can expect that the charges of F<sup>+</sup> and F<sup>2+</sup> centers have to be compensated at least to a certain amount by cation vacancies, so-called V centers [139]. Cation vacancies exist in three different charge states, V<sup>0</sup>, V<sup>-</sup> and V<sup>2-</sup> resulting from the removal of a Mg, Mg<sup>+</sup> and Mg<sup>2+</sup> atom/ion respectively. V centers have been analyzed in experimental [190, 191] and theoretical [114, 181, 192–195] studies. Compared with the F centers much less work has been performed on the V centers. One reason is that V centers are present in smaller concentrations due to their high formation energies. To remove a cation from bulk and form a V<sup>2-</sup> center requires an energy of about 13-20 eV [188, 194]. The trend of the formation energy of V centers is comparable to the formation energy trend of F centers. To create a V<sup>0</sup> center in bulk requires an energy of 15 eV while at the surface 13.5 eV are needed [195]. Therefore they tend to migrate to the surface at high temperatures. Electrons that can be attributed to the

$V^-$  and  $V^{2-}$  centers are occupying levels near the top O 2p valence band and are localized on the oxygen ions surrounding the defect [181]. The charge interaction with the Madelung potential is responsible for the stability of the V centers:  $V^{2-} > V^- > V^0$  [181]. The relaxation of the lattice around the V center is for a neutral  $V^0$  the smallest and rises with increasing charge but is slightly smaller than for the F centers, since the charge is not localized inside the V center but on the surrounding oxygen ions [181].

However, the complexity of the properties of the color centers like charge state, formation energy and stability increases when MgO thin films are grown on a metal substrate. The properties of the color centers are affected by: metal work function, distance to the metal substrate and therefore film thickness, the position inside the film or the position on the surface like steps, edges, corners. A detailed discussion of the influence of these parameters can be found in Ref. [118]. The formation energy of an  $F^0$  defect on a terrace of a 3 ML MgO film supported on Ag(001) is with 9.44 eV comparable to the formation energy of the unsupported MgO layers 9.48 eV. Both values have been calculated by plane wave gradient corrected DFT [118]. Also the geometrical relaxation is quite similar (about 3 %).

A difference occurs in the density of states. For the unsupported MgO layers the occupied  $F^0$  states have been calculated to be in the band gap about 2.15 eV above the top of the valence band. If the film is supported the states introduced by the defect are 2.35 eV above the valence band [118]. For comparison, it would be interesting to calculate with the same DFT code used to calculate the formation energy of the above discussed  $F^0$  center, the formation energies of an  $F^+$  and an  $F^{2+}$  center. This is not possible, since the background for charge neutrality introduces a disruptive interaction [118].

However, the states introduced by the defect can be calculated with the same approach. For an  $F^+$  center on a terrace the defect states are 1.75 eV and 2.05 eV for the unsupported MgO and Ag supported 3 ML MgO thin films, respectively, above the valence band [118]. Theoretical calculations for  $F^{2+}$  defect states within the gap have not been published so far, however, they are expected to be close to the MgO valence band [196]. Also the states of divacancies have not been published or have not yet been calculated. Table 3.3 summarizes the formation and relaxation energies. Since DFT calculations underestimate the band gap only trends become obvious. Figures 3.9(a,c) show energy levels for  $F^0$  and  $F^+$  color centers calculated by a DFT embedded cluster method and experimentally determined values by STS [figure 3.9(b)] that can be correlated to the calculated levels [95]. The valence band (VB) is about 4.5 eV below the Fermi level and the conduction band (CB) is about 2.2 eV above the Fermi level. The calculated unoccupied states for an  $F^+$  center are about 1-2 eV above the Fermi level, while the

Table 3.3: Formation energies and lattice relaxations for different defect types in their ground state. The defects are either located at a surface terrace of 3 ML MgO supported on Ag(001) or on a surface terrace of unsupported 3 ML of MgO. The formation energies will decrease considerably when located at edges, steps and corners. [118, 181]

type	form. energy [eV]	latt. relax.	Ref.
F <sup>0</sup> 3 ML MgO/Ag	9.44	0.06 Å, 3 %	[118]
F <sup>0</sup> 3 ML MgO	9.48	≈0.06 Å, 3 %	[118]
F <sup>+</sup> 3 ML MgO/Ag	-	≈ 0.13 Å, 6-7 %	[118]
F <sup>+</sup> 3 ML MgO	11-12	≈ 0.13 Å, 6-7 %	[118, 181]
F <sup>2+</sup> 3 ML MgO/Ag	-	-	-
F <sup>2+</sup> 3 ML MgO	33-36	≈ 0.2 Å, 10 %	[179, 181]

occupied states are 1.5-2.5 eV below the Fermi level, thus defects with type I signature have been attributed to F<sup>+</sup> centers [see figure 3.9(a)]. Furthermore, the energy levels depend on the local positions of the defects as already discussed. For type II defect states at about ±1 eV have been observed. These states are attributed to F<sup>0</sup> color centers.

Optical spectra of thin MgO films have been studied in a number of publications [197–200]. The experimental EELS data presented in Ref. [198] show 5 distinct loss features (1.0, 1.3, 2.4, 2.8 and 3.4 eV). A primary electron beam of 40 eV has been focused on the MgO thin film grown on Ag(001). A clear understanding and assignment of the loss features with the help of theory have not yet been achieved. The observed loss features have been compared with offset reduced post Hartree Fock calculations [199]. The offset meaning overestimation of the derived Hartree Fock values has been estimated to be 1 eV [198]. Comparing theory and experiment leads to the suggested assignment of loss features to F<sup>0</sup> centers located at different surface sites and color center dimers (M centers) as shown in table 3.4.

The transition from the singluet ground state to the triplet excited state is a s-p like transition [118]. The decomposition of loss features originating from F<sup>0</sup>, F<sup>+</sup> and F<sup>2+</sup> is difficult, since they are close in energy [201]. When exposed to an oxygen background pressure the loss features disappear, which is an indication that they are related to color centers close to the surface [198]. However, for bulk color centers the calculations clearly show a blue shift of additional 2.0 to 2.5 eV [202]. The discussed loss features appear after electron bombardment of thin MgO films. For thicker films and/or higher energies like those available from x-ray sources additional loss features can

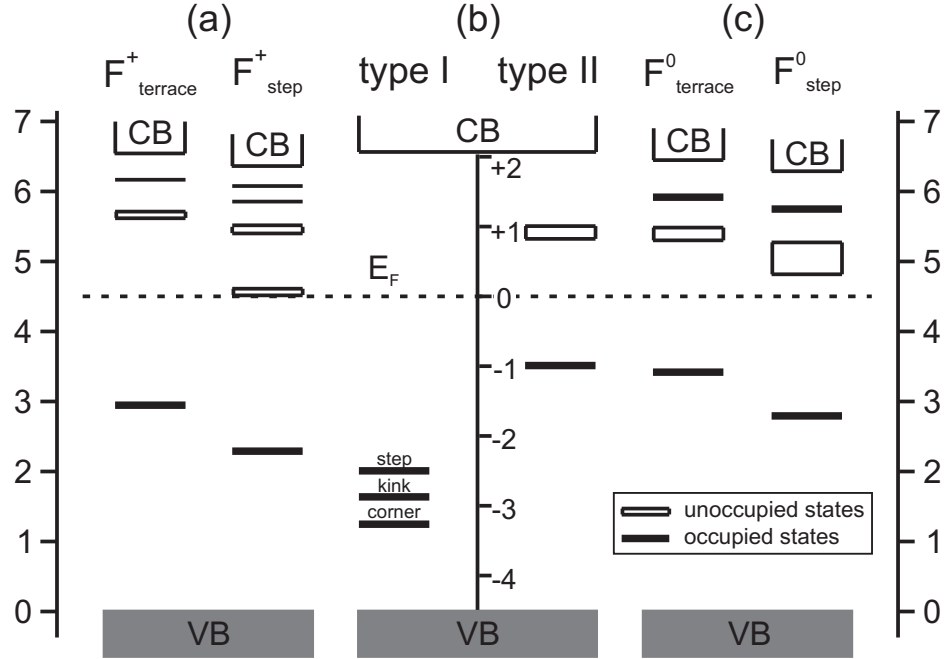


Figure 3.9: (a) Calculated energy levels of  $F^+$  centers on terrace and step sites. (b) Energy level detected by STS for type I and type II defects. (c) Calculated energy levels of  $F^0$  centers on terrace and step sites. The units in (a), (b) and (c) are Volts. Figure reproduced from Ref. [95].

be observed [202] showing the complexity arising from different defect types and sites.

The kinetics of  $F^0$  color center formation at the surface has been studied by analyzing the loss intensity, used as a measure of defect concentration, with respect to electron exposure in units of electrons per surface oxygen atom [198] (figure 3.10).

The derived rate equation is of first order given by [198]

$$\frac{dn}{dD} = a(1 - n) - bn \Rightarrow n(D) = \frac{a}{a + b} \left(1 - e^{-(a+b)D}\right). \quad (3.5)$$

The first term describes the defect generation and the second term the defect annihilation of surface color centers. Variable  $n$  represents the number of surface oxygen atoms while  $b$  represents different mechanisms for defect annihilation, like adsorption of atoms from the residual gas phase [198]. Bulk defects have not been considered, since the loss features disappear when exposed to an oxygen background pressure. The initial slope is given by

$$a = \lim_{n \rightarrow 0} (dn/dD) \quad (3.6)$$

Table 3.4: Suggested assignment of EELS features [198] with the help of post Hartree Fock calculations [199] for  $F^0$  color centers present at different surface sites. The absorption wavelength  $\lambda_{exp}$  has been calculated based on the experimental energy values. The experimentally determined loss features at 1.0 and 1.3 eV are supposed to be related to M-centers.

Location	Transition	$E_{calc}$ [eV]	$E_{calc} - 1$ eV [eV]	$E_{exp}$ [eV]	$\lambda_{exp}$ [nm]
terrace	$1s \rightarrow 2p_{x,y}$	4.72	3.72	3.4	364
terrace	$1s \rightarrow 2p_z$	3.39	2.39	2.4	516
step	$1s \rightarrow 2p_{x,y}$	3.82	2.82	2.8	442
step	$1s \rightarrow 2p_z$	2.92	1.92	-	-
corner	$1s \rightarrow 2p_{x,y}$	2.6	1.60	-	-
M-center	-	-	-	1.0 , 1.3	1239 , 953

which is a measure for the cross section of color center generation [198]. Since the five loss peaks follow the same first order kinetics, it is concluded that either only single defects are created during electron bombardment or that color centers agglomerate, e.g., M centers are formed by a one step process [198]. Deviations from a random formation of, e.g., M centers cause a parabolic or higher order onset of the loss intensity vs electron exposure curves, as has been observed for color center generation on NaCl films [203]. For the desorption process of neutral or ionic oxygen species an Auger decay of core holes, created by electron bombardment, seems to be most likely [122, 198]. This mechanism has been proposed by Knotek and Feibelman [204, 205]. To create a core hole in the O 2s energy level an energy of about 17 eV is required. This hole can be refilled by electrons from the valence band which are mainly located at the oxygen site.

The energy gained can be transferred to other valence band electrons that are consequently emitted. This process is an intra atomic Auger process. If the energy of the incident electrons is high enough to create a hole in the Mg 2p state (about 50 eV), the hole can be refilled by valence electrons and again the energy gained will be sufficient to eject electrons from the valence band. This process is an inter atomic process. The intra atomic decay is expected to be much faster due to the larger overlap of wave functions. The oxygen ion involved in the Auger process thus becomes neutral or positively charged. Both types can leave the surface, while especially the positively charged oxygen will be ejected due to the repulsive interaction with the Madelung

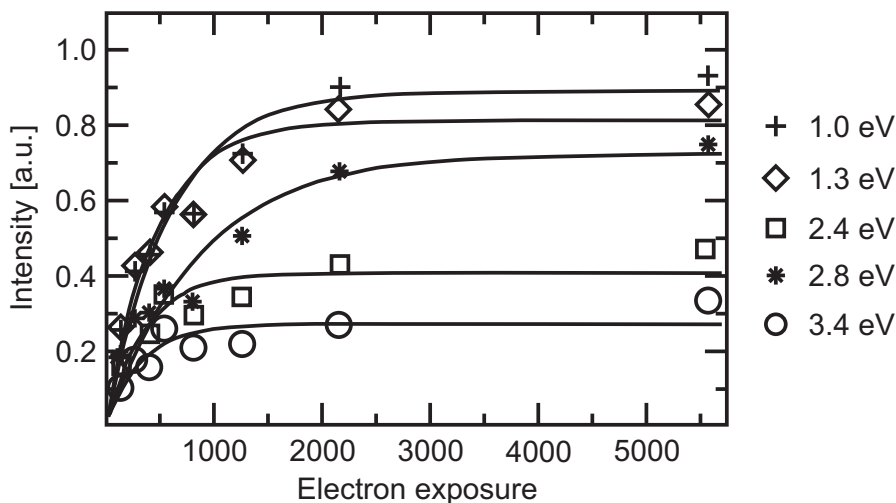


Figure 3.10: Intensity evolution of loss peaks (EELS) as a function of electron exposure at a bombardment energy of 200 eV. The corresponding losses are indicated in eV. The electron exposure is in units of electrons per surface oxygen atom. The solid lines have been fitted to  $a/(a+b)(1-e^{-(a+b)D})$ . Data have been taken from Ref. [198].

potential of the surrounding cations [198, 206]. The energy required to release a neutral or ionic oxygen considerably decreases with decreasing coordination number as presented in table 3.3 for surface terrace defects [118].

The MGR mechanism as described by Menzel, Gomer and Redhead, which is based on a one-electron Franck-Condon excitation from a bonding to an antibonding state, is supposed to play a minor role, since for an excited state the  $O^{2-}$  is still attracted by the strong Madelung potential.

However, the number of defects and the type of defects generated depend on a number of experimental parameters. The temperature, energy and geometry of electron bombardment, the thickness of the MgO film and the influence of secondary electrons generated in the metallic substrate have to be taken into account. A detailed disentanglement of these parameters is difficult and has so far not been achieved.

Finally the lifetimes of the considered defects play a significant role whether the defects can contribute to chemical reactions or not, especially when thin films are supported by a metal substrate. In that case charge can in principle be transferred to the metal or vice versa. However, the importance of lifetimes is discussed in literature [118] but no concrete answers have been presented so far. Since some of the discussed experiments have been performed on the time scale of hours or in the case of low temperature environments

days [50, 95], lifetimes seem to be long enough such that color centers can be involved in chemical reactions as discussed.

### 3.5 Preparation of MgO Thin Films on Ag(001)

The preparation conditions of MgO on Ag(001) follow a route described in Ref. [136] where a stoichiometric composition was observed. This procedure has proven its applicability in many preparation cycles. The Ag(001) was sputtered with  $\text{Ar}^+$  ions at a current density of  $10 \mu\text{A}/\text{cm}^2$  and 800 V for 15 min. Afterwards, the Ag(001) was annealed to 690 K for 30 min. The sputtering and annealing cycle was repeated several times. Mg was evaporated from a Knudsen cell in an oxygen atmosphere of  $1 \times 10^{-6}$  mbar, at a substrate temperature of 560 K, and a deposition rate of about 1 ML of MgO/min. The desired number of MgO layers can be grown onto the Ag(001) by linear extrapolation of a sub-monolayer coverage to the desired number of monolayers, assuming a constant sticking coefficient. This preparation method is only possible if the reaction kinetics of Ag with oxygen is very slow [207] compared with the reaction between Mg and O. Figures 3.11(a-c) show LEED images of the bare Ag(001) and 3 ML MgO grown on Ag(001) in the described manner.

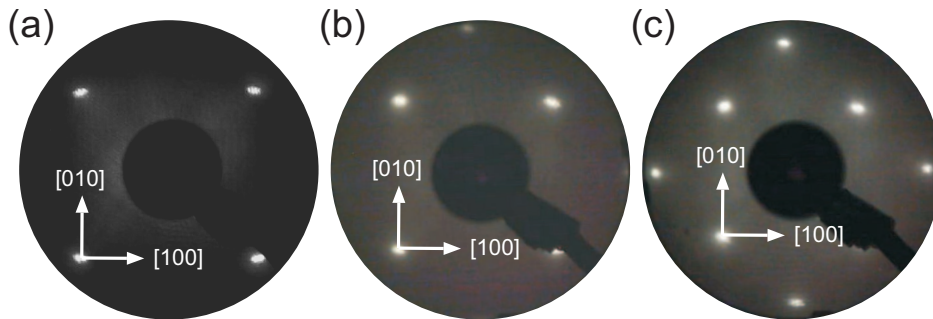


Figure 3.11: LEED images of the (a) bare Ag(001) and (b,c) 3 ML MgO grown on Ag(001). Primary electron energies are (a)  $E_P = 60$  eV, (b)  $E_P = 70$  eV and (c)  $E_P = 93$  eV.



# Chapter 4

## Ag(001) Work Function Shift Induced by the MgO film

The metal work function is a key parameter for charging adsorbates with high electron affinity on thin oxide films grown on metal single crystal surfaces. Here the first experimental data for the work function shift of Ag(001) induced by 1, 3 and 8 monolayers of MgO is measured *in situ* by three independent scanning probe techniques on the same surface area, making the different approaches comparable. The methods to detect the work function shift are based on the Kelvin probe force microscopy measuring the contact potential difference (CPD),  $I_T(z)$  curves and field emission resonances. The motivation will be followed by the measurement procedure, the results and discussion including a comparison with theoretical predictions.

### 4.1 Motivation

Oxide films of varying thickness have intensively been studied in the research field of heterogeneous catalysis since they are often used as supports for catalytically relevant metal particles and clusters [208]. While oxide films of about 6 ML often already resemble bulk properties, films of about 1-3 ML differ from those, therefore thin film systems can exhibit properties in their own rights [1, 110]. Moreover, the film thickness has been found to be a critical parameter to tune properties of adsorbed particles. Controlled by the film thickness adsorbates might become charged and chemically active or stay neutral and chemically inert [209]. The charging of Au and Pd clusters of different size has recently been discussed by density functional theory calculations for metal/MgO systems [210–213] and for MgO/Ag(001) [214]. While Au single atoms and clusters are charged [49, 131] Pd atoms and clus-

ters have been found to be neutral [49]. The charging of single Au atoms and clusters has experimentally been confirmed by STM investigations [49, 131]. Surprisingly Au, which is chemically inert, has been found to be chemically active when it is charged [126, 215, 216]. Moreover, the charging affects the adsorption energy as well as the adsorption site [210, 213]. The charge is supposed to result from the oxide/metal, i.e. MgO/Ag(001) interface [210, 217]. For high coverages the negatively charged Au atoms (0.9 electrons/Au, Bader analysis [213]) repel each other and form a superstructure [49]. However, the charge transfer depends on the electronegativity of the adsorbate, thus Pd atoms in contrast to Au stay neutral [49, 210], the work function of the Ag(001) with MgO grown on top, and the tunneling length. The electronegativity depends on the adsorbate itself and the film thickness (controllable by the growth procedure), which must not exceed the tunneling length. An interesting parameter is the shift of the Ag work function induced by the MgO layer grown on top. Moreover, these measurements are an ideal starting point to investigate the experimental parameters necessary for investigations with point defect resolution as demanded in chapter 5.

## 4.2 Preliminary Considerations

The work function, as one of the suggested key parameters for charge transfer, is generally defined as the minimum potential the most loosely bound valence electron in the solid has to overcome in order to be ejected into vacuum outside the solid with zero kinetic energy at absolute zero temperature [218]. Therefore the work function  $\Phi_m$  of a metal can be outlined as

$$\Phi_m = eV_{exchange} + eV_{dipole} - E_F , \quad (4.1)$$

where  $E_F$  is the Fermi energy,  $V_{exchange}$  results from electron-electron interactions and thus from correlation effects and depends on the bulk electron density.  $V_{dipole}$  represents the surface dipole that must be overcome by the electrons and is responsible for each crystallographic orientation having a different work function. The work function of the metal  $\Phi_m$  can be lowered or increased depending on the dielectric/metal interface [129] resulting in  $\Phi_{m/d}$ .

The model proposed by Schottky for a dielectric/metal interface forming a Schottky barrier with a height given by the difference of the top of the valence band and the metal work function is not applicable in general. The reason for this is that there is no charge transfer across the Schottky barrier, however the metal induced gap states (MIGS), as discussed in section 3.3, can act as electron donor or acceptor states depending on their position within the gap. Therefore, charge transfer across the metal dielectric interface can

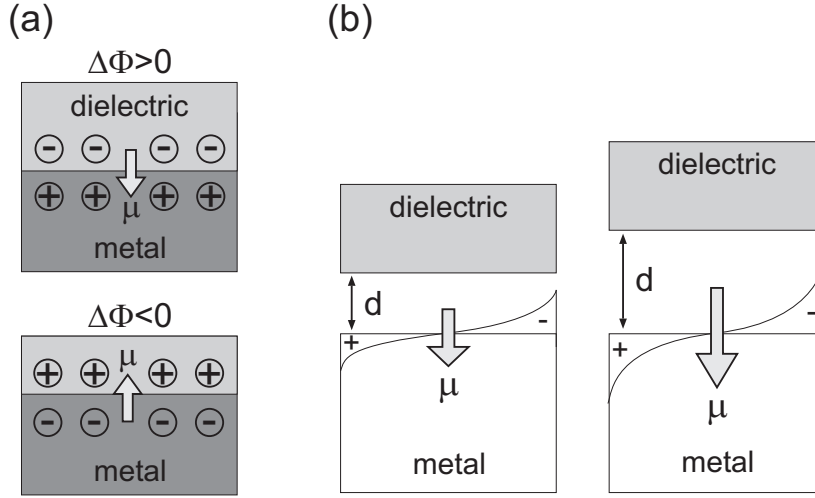


Figure 4.1: The two major contributions to the work function shift (a) charge transfer at the interface and (b) electrostatic compression effect due to the adhesion of the dielectric media on the metal surface. Both terms affect the surface dipole  $\mu$  and hence the metal work function. In analogy to Ref. [130].

occur. Density functional theory calculations have shown that charge transfer affects the work function  $\Phi_{m/d}$ . Especially negative charges above the metal increase the surface dipole and lead to an increase in work function. Positive charges above the metal surface decrease the surface dipole (or even change the sign) resulting in a lowering of the work function [compare figure 4.1(a)] [130]. The shift of the metal work function  $\Delta\Phi = \Phi_{m/d} - \Phi_m$  can have, beside the charge transfer, two further contributions. The electrons of the bare metal surface spill out of the metal and decay into the vacuum, creating a surface dipole. With a dielectric medium grown on a metal surface the electrons decaying into the vacuum are pushed back into the metal surface, thus the surface dipole decreases [see figure 4.1(b)]. The contribution of this compression effect strongly depends on the adhesion energy of the dielectric medium on the metal. For high adhesion energies the bonding distances are smaller and therefore the compression effect is stronger than for small adhesion energies and large bonding distances. A third effect that has to be considered in some cases is the relaxation of the interface. Thus the shift can be outlined as [130]

$$\Delta\Phi = \Delta\Phi^{CT} + \Delta\Phi^{comp} + \Delta\Phi^{IR} \quad (4.2)$$

with  $\Delta\Phi^{CT}$  as the shift due to charge transfer processes,  $\Delta\Phi^{comp}$  as the shift resulting from the compression of the electron wave functions back into the

metal and  $\Delta\Phi^{IR}$  originating from the interface relaxation. The charge transfer effect dominates the work function change of films interacting strongly with the metal substrate while the compression effect is dominant for highly ionic films like MgO [130]. For metals like Ag  $\Delta\Phi^{IR} \approx 0$  is valid since the surface relaxation is quite small [130]. Table 4.1 shows some important properties of MgO grown on Ag(001) and Mo(001).

Table 4.1: Important properties of MgO on Ag(001). For comparison values of MgO on Mo(001) are presented. N represents the number of layers, d the interface distance,  $\Delta\mu/S$  the surface dipole change with respect to the pristine metal, CT/S the net charge transfer per surface area,  $E_{adh}/S_{int}$  the energy per interface area,  $\Phi$  is the work function of the pristine metal,  $\Delta\Phi$  is the change of the metal work function due to the MgO overlayer(s). Data taken from Ref. [129].

	N	d [Å]	$\Delta\mu/S$ [q/Å]	CT/S [q/Å <sup>2</sup> ]	$E_{adh}/S_{int}$ [eV/Å <sup>2</sup> ]	$\Delta\Phi_{m/d}$ [eV]	$\Delta\Phi$ [eV]
MgO/Ag(001)	1	2.62	0.0053	0.0101	0.031	3.29	-1.01
	2	2.73	0.0065	0.0050	0.022	3.10	-1.20
	3	2.73	0.0064	0.0055	0.023	3.12	-1.18
MgO/Mo(001)	1	2.10	0.0097	0.0161	0.153	2.52	-1.67
	2	2.15	0.0118	0.0090	0.135	2.05	-2.14
	3	2.14	0.0118	0.0093	0.136	2.05	-2.14

The difference in metal work function for MgO on Ag(001) and on Mo(001) is about 1 eV. This difference has its origin in the adhesion energies of MgO on Ag(001) and Mo(001), which is 6 times larger for MgO on Mo(001). The stronger adhesion energy results in a shorter interface distance and thus in a stronger compression of the metal electrons leading to their polarization and therefore in a stronger shift of the surface dipole resulting in a larger work function shift  $\Delta\Phi$ .

### 4.3 Measurement Procedure

From electrostatic tip-sample interactions, as deduced in section 2.3.2, work function differences can be measured based on the equation

$$F_{el} = \frac{1}{2} \frac{dC}{dz} \left( U_S - \frac{\Delta\Phi}{|q|} \right)^2 . \quad (4.3)$$

The change in  $\Delta\Phi$  when going from the clean Ag(001) to 1, 3 and 8 ML MgO was determined at constant  $x$ ,  $y$  and  $z$  positions, i.e. during each measurement the tip position was constant. The bias voltage was swept and the parabolic behavior of the electrostatic force was detected as the resonance frequency shift. Since the  $z$  position is constant, only the change of the long range electrostatic force is detected while contributions to the frequency shift from other forces result in a frequency shift offset which does not contain information on the work function shift and can therefore be subtracted. Since the maxima of the parabolae in figure 4.3 are given by  $\Delta\Phi/|q| = U_S$  (compare equation 4.3), the shift of the maximum along the abscissa provides the information of interest. In a single measurement:  $\Delta\Phi = \Phi_{\text{sample}} - \Phi_{\text{tip}}$ . By taking the difference  $\Delta\Phi_{\text{MgO/Ag}} - \Delta\Phi_{\text{Ag}}$  the effect of the tip can be canceled and the Ag(001) work function shift can be derived. However, stable tip-sample conditions are a prerequisite for reproducible measurements.

The second method applied to characterize the shift in the metal work function utilizes the STM mode of the dual mode setup. The oscillation of the tip was disabled and the tip was situated at a fixed lateral position. The tip was moved towards the sample surface while the tunneling current was recorded simultaneously with the  $z$  displacement of the tip. The tunneling current exponentially depends on the  $z$  displacement as described by Binnig and Rohrer [219, 220] by the well-known equation

$$I_T(z) \propto \exp \left( -2z \sqrt{2m\Phi_{ap}/\hbar^2} \right) , \quad (4.4)$$

where  $m$  is the mass of the electron and  $\Phi_{ap}$  the apparent barrier height. A typical curve is shown in figure 4.4(a). The graph shows the exponential dependence of  $I_T$  on  $z$ . The inset presents a logarithmic plot of the same data. The apparent barrier height can be calculated from an exponential fit or from the slope of the logarithmic plot [221].

The third method applied to identify the shift in the Ag(001) work function is based on field emission resonances (FER), operating the microscope in the STM mode. If the applied bias voltage exceeds the work function, electrons can form standing waves in the vacuum gap between tip and sample.

The standing waves are the eigenstates of the sample-vacuum-tip potential and are also known as Gundlach states. A detailed consideration of field emission resonances is given in section 2.4.5. Since the detection of a large number of resonance states requires high voltages, tip changes are very likely in constant height mode due to the high electric field. Thus the feedback loop was closed to keep the tunneling current constant. The tip was not oscillating and the FER were taken at constant lateral position while the bias voltage was swept [see figure 4.5(a)]. For the analysis of the data the equation 4.5 has been used. The condition for the FER to occur is than given by [99]

$$E_n = eU_n = \Phi_S + \left( \frac{3\pi\hbar e}{2\sqrt{2m}} \right)^{2/3} \epsilon^{2/3} n^{2/3}, \quad (4.5)$$

where  $e$  is the charge of an electron,  $U_n$  is the voltage of the  $n$ -th resonance,  $\Phi_S$  is the sample work function,  $\epsilon$  is the electric field and  $n$  is the number of the  $n$ -th resonance. This equation does not account for the image potential which rounds off the corners of the potential [97] between tip and sample. The influence of the image potential mainly affects resonances with small  $n$ . Thus the first resonance of the spectra was excluded from the data analysis. By fitting equation the 4.5 to  $U_n$  vs  $n$  the work function of the different sample systems and the shift by taking the difference to the bare Ag(001) can be determined. All the three techniques have in common that stable tips are a prerequisite, which has been checked before and after the measurements by comparing contrasts in images. Furthermore the measured curves themselves show artifacts if tip changes occur. In addition the reproducibility of the derived values are an indication of stable tip-sample conditions.

## 4.4 Results and Discussion

The surfaces investigated are presented in figure 4.2. The three techniques with high local resolution, which have already been discussed, have been applied on the clean Ag(001) surface, on 0.5 monolayer (ML) (effectively 1 ML high islands), 3 and 8 ML MgO on Ag(001). Figure 4.2(a) shows terraces of the clean Ag(001) surface, while (b) presents MgO islands and (c) 3 ML MgO grown on Ag(001). The surface structure of the 8 ML film is indistinguishable from the 3 ML film by FM-DFM and STM images.

Representative curves showing contact potential difference measurements on clean Ag(001) and 3 ML MgO/Ag(001) are shown in figure 4.3. As previously discussed the shift along the abscissa results from the work function shift. The dashed and dotted lines are fits to parabolae to determine the positions of the corresponding maxima.

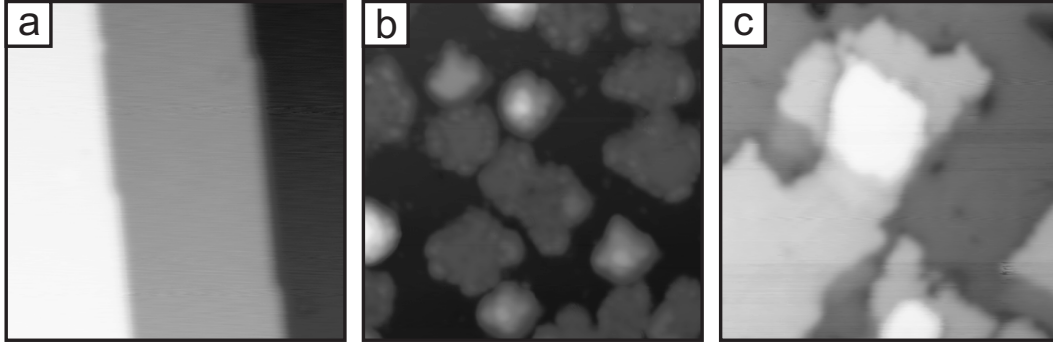


Figure 4.2: STM images: (a) bare Ag(001),  $20 \times 20 \text{ nm}^2$ ,  $U_S = 10 \text{ mV}$ ,  $I_T = 1 \text{ nA}$ . (b) MgO islands (0.5 ML) grown on Ag(001),  $50 \times 50 \text{ nm}^2$ ,  $U_S = 3.5 \text{ V}$ ,  $I_T = 400 \text{ pA}$ . (c) MgO film of 3 ML on Ag(001),  $30 \times 30 \text{ nm}^2$ ,  $U_S = 3.5 \text{ V}$ ,  $I_T = 200 \text{ pA}$ .

A typical tunneling current vs  $z$  displacement curve is shown in figure 4.4. With the equation 4.4 the apparent barrier height can be determined.

Nevertheless, it is not straightforward to extract the work function from the apparent barrier height. Controversial statements have been made in the past. In his theoretical considerations Lang [220] claims a convergence of  $\Phi_{ap}$  to  $\Phi$  for large  $z$  displacements, while Chen [42] in his theoretical approach shows that  $\Phi_{ap}$  stays constant till point contact. The latter has been confirmed by Besenbacher et al. [222] in an experiment. They point out that it is crucial to measure  $U_S$  simultaneously to  $I_T(z)$ , due to the finite impedance of the tunneling current amplifier. This effect is mainly a consequence of the deviation of the amplifier from an ideal amplification. Thus a voltage drop occurs at the input of the amplifier. Furthermore, the resistance of the bias voltage supply can cause additional voltage deviations. Therefore for performing these experiments a highly advanced current amplifier is necessary in combination with a stable bias voltage supply. Moreover, the bias voltage might deviate from the set value due to elastic deformations within the tunneling gap [222]. These deformations reduce the tip-sample distance in a non-linear way, which can affect the tunneling current significantly. Depending on the stiffness of tip and sample the relaxation effect occurs with the tip a few Ångström above the surface. The  $I_T(z)$  curves taken within these investigations do not show deviations from exponential behavior (see figure 4.4), thus relaxation effects are not supposed to be crucial in these measurements.

Figure 4.5(a) shows field emission resonances. The first resonance is indicated. While figure 4.5(b) shows a set of resonance peak positions vs bias

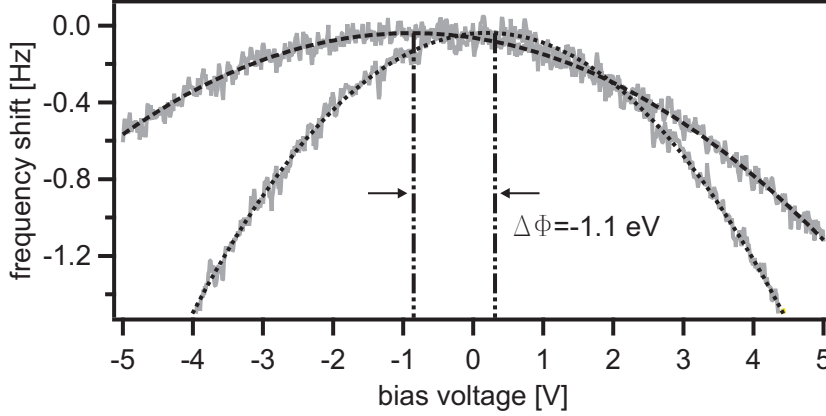


Figure 4.3: Contact potential measurements on clean Ag(001) (dashed parabola fit) and on 3 ML MgO/Ag(001) (dotted parabola fit). The dashed-dotted line indicates the shift of the work function. For each curve the tip position was constant.

voltage as derived from measurements equivalent to figure 4.5(a). The blue solid line is a fit to the equation 4.5, from which the work function of the Ag(001) surface can be derived as one of the fitting parameters.

The results of the three independent techniques are listed in table 4.2. The first column represents the number of MgO layers grown on the Ag(001) by the growth method previously stated. The MgO islands were effectively one monolayer high. The second column presents theoretical values calculated by Pacchioni et al. [130]. The calculations are based on density functional theory (DFT) using the generalized gradient approximation (PW-91 functional) [223] implemented in the VASP program [224, 225] which uses a plane wave basis set and a projector augmented wave (PAW) method [226] for the treatment of core electrons. The third to fifth columns show the experimental data. Considering the CPD measurements good agreement with theory for the work function shift can be found except for the MgO islands. The experimental value of -0.5 eV is too small compared with the theoretical value of -0.94 eV. This discrepancy arises from an averaging effect.

Due to the long range nature of the electrostatic force the area of tip and sample involved in the CPD measurements is larger than the MgO islands, thus measurements average over MgO covered areas and the bare Ag(001). Furthermore at tip-sample distances of about 3 nm above the surface [see figure 4.6(a)] the measured work function shift on a MgO island (crosses) and on the bare Ag(001) (circles) between the islands are indistinguishable. When the tip gets closer to the surface the shift measured on the MgO

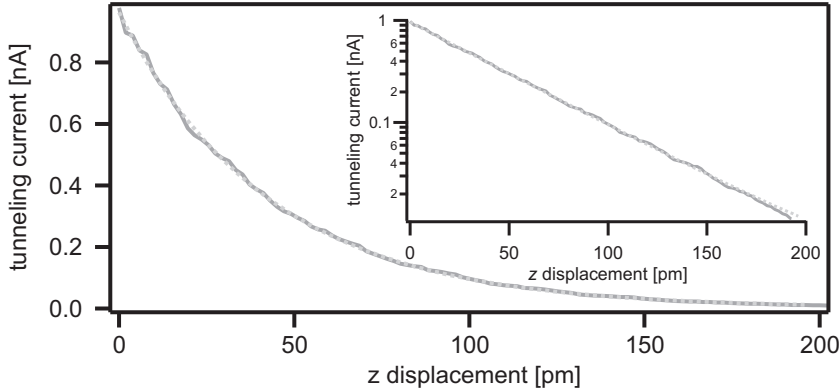


Figure 4.4: Tunneling current vs distance relation, i.e.  $I_T(z)$  curve (inset shows a logarithmic plot). Dashed line indicates exponential fit.

island and the Ag diverge. The maximum difference is  $-0.5$  eV taken at a tip position  $200$  pm closer to the surface than the set-point. Note that the zero position of the  $z$  displacement belongs to the set-point  $U_S = -2$  V,  $I_T = 500$  pA. At closer distances tip changes occurred while sweeping the bias voltage although the bias sweep was limited from  $-2$  V to  $+2$  V. The divergence of the shift at close distances clearly shows an increase in lateral resolution of the work function shift. To explain the increase in resolution, the attractive electrostatic interaction of tip and sample has been simulated by a one dimensional model. The tip is represented by a single atom while the surface is given by a line of 25 atoms [see figure 4.6(b)].

Table 4.2: Comparison of experimental and theoretical data. ( $\dagger$  data from Ref. [130],  $\ddagger$  data from Ref. [129], \*calculated for 1 monolayer.)

number of MgO layers on Ag(001)	theory	experiment		
	$\Delta\Phi$ [eV]	CPD $\Delta\Phi$ [eV]	$I_T(z)$ $\Delta\Phi_{ap}$ [eV]	FER $\Delta\Phi$ [eV]
MgO island	$-0.94^{*\dagger}$	$-0.5$	$-2.0$	$-1.2$
3	$-1.18^\ddagger, -1.27^\ddagger$	$-1.1$	$-1.4$	$-1.4$
8		$-1.1$	$-1.2$	$-1.3$

The interaction of the tip atom with the surface atoms has been calculated in analogy to Ref. [51] by the summation of pair potentials. For the pair potential a Coulomb potential has been chosen with a negative and positive charge resulting in an attractive electrostatic potential (compare section 2.3.2 and equation 4.3). Therefore the tip atom sample interaction results in

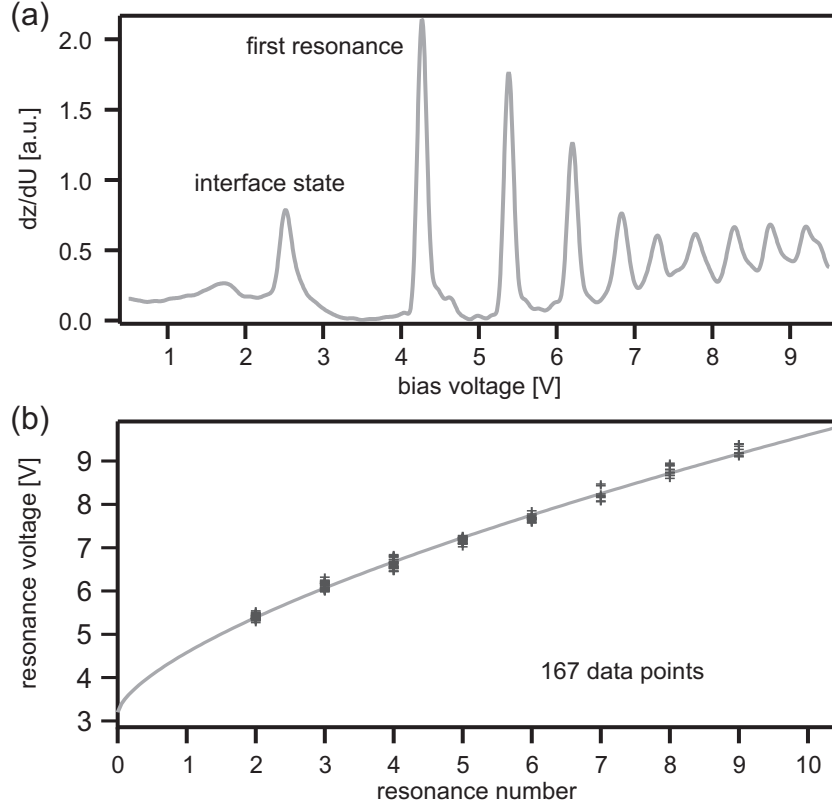


Figure 4.5: (a) Field emission resonance curve taken on MgO. Feedback on  $I_T(z)$ . (b) A representative collection of 167 resonance peaks vs voltage position measured on 3 ML derived from field emission resonances. The first resonance has not been considered due to image charge effects.

$$V_{ts} = \sum_i^N V_i = V_j + \sum_{m \neq j}^N V_m, \quad (4.6)$$

where  $V_j$  is the interaction of the tip atom with the surface atom directly beneath the tip.  $\sum_{m \neq j}^N V_m$  describes the interaction of the tip atom with all other surface atoms except the one at position  $r_j$  directly under the tip. The pair potential  $V_i$  is given by the Coulomb interaction

$$V_i = \frac{q_1 q_2}{4\pi\epsilon_0 r_i}, \quad (4.7)$$

where  $\epsilon_0$  is the dielectric constant,  $q_1$ ,  $q_2$  are the charges of the tip and a surface atom at distance  $r_i$  respectively. Thus  $r_i$  is given by

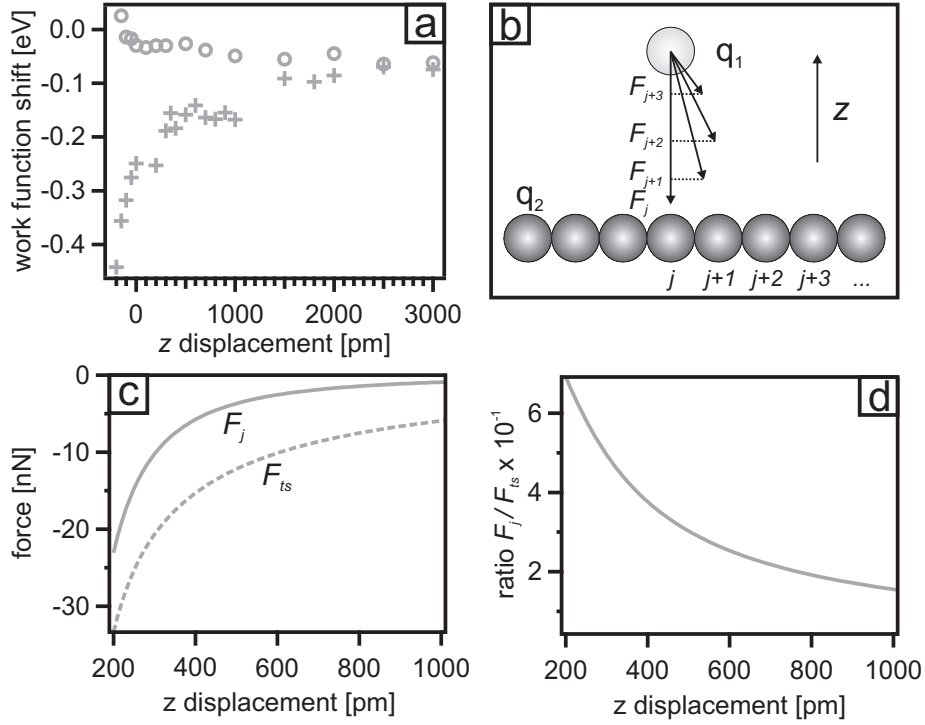


Figure 4.6: (a) Work function shift vs  $z$  displacement. The crosses were taken on the MgO islands while the circles indicate measurements between the islands on the Ag(001). For large  $z$  displacements the measurements on the islands reveal the same values as on the Ag(001) between the islands. For small distances the maximum positions diverge. (b) Simulation of the tip-sample interaction (not all surface atoms considered in the simulation are shown). The projection of the Coulomb force onto the  $z$  axis is indicated. (c) Solid line represents the force  $F_j$  of the tip and the atom directly beneath the tip. The dashed line indicates the force  $F_{ts}$  between the tip atom and all surface atoms. (d) Ratio  $F_j/F_{ts}$  see text.

$$r_i = \sqrt{(x_{q_1} - x_{q_2,i})^2 + (y_{q_1} - y_{q_2,i})^2 + (z_{q_1} - z_{q_2,i})^2}. \quad (4.8)$$

Thus the force between the tip and the  $N$  surface atoms summarizes to

$$\begin{aligned} F_{ts}(z) &= -\frac{\partial V_{ts}}{\partial z} = -\frac{\partial}{\partial z} \left( V_j + \sum_{m \neq j}^N V_m \right) \\ &= F_j(z) + \frac{q_1 q_2}{4\pi\epsilon_0} \sum_{m \neq j}^N \frac{1}{r_m^2} \frac{z}{r_m}. \end{aligned} \quad (4.9)$$

The term  $z/r_m$  accounts for the fact that only force components in  $z$  direction result in a frequency shift.  $F_j(z)$  and  $F_{ts}(z)$  have been calculated for different  $z$  displacements [see figure 4.6(c)]. The solid line in figure 4.6(c) represents the force  $F_j$  between the tip atom and the surface atom directly beneath it. The dashed line indicates the force between the tip and all surface atoms  $F_{ts}$ . Figure 4.6(d) presents the ratio of these interactions, therefore it is defined by: ratio= $F_j/F_{ts}$ . This ratio clearly indicates that the contribution to the force of the atom directly beneath the tip increases with decreasing tip-sample separation. Therefore the increase in resolution for the CPD measurements on MgO islands with decreasing  $z$  separations as shown in figure 4.6(a) can be explained. Nevertheless a further resolution enhancement meaning operating at closer distances, however, was not possible due to the mentioned tip instabilities. On the 3 ML and 8 ML MgO film this averaging effect is not important since the layers cover large areas. The detected values for the work function shift from CPD are close to theory. The standard deviation of the CPD measurements presented in table 4.2 is about 11 %. However, an absolute determination of the work function is not possible with this technique, since the electrostatic force is only sensitive to the work function difference (compare equation 4.3).

For the  $I_T(z)$  measurements a value of  $\Delta\Phi_{ap} = -2.0$  eV for 0.5 ML MgO on Ag(001) has been derived, which is considerably larger than the calculated DFT value, despite the high lateral resolution due to the exponential tunneling dependence on  $z$ . The derived values on 3 ML and 8 ML MgO broadly correspond with the theory. Nevertheless the standard deviation of this method is the largest about 20 %. The absolute value for the work function measured on the clean Ag(001) surface by  $I_T(z)$  curves is  $\Phi_{Ag} = 4.1 \pm 0.6$  eV, which matches the value of 4.23 eV calculated by DFT [130] and a value derived from UPS measurements of  $4.22 \pm 0.04$  eV [227].

Considering the FER the experimental and theoretical data for the work function shift correspond well. The measurements on the 0.5 ML MgO film

benefit from the previously discussed dependency of the tunneling current resulting in a value of  $\Delta\Phi = -1.2$  eV. The standard deviation is about 11 %. From the fit to the equation 4.5 the electric field  $\epsilon$  between tip and sample can be calculated resulting in  $\approx 2$  V/nm. The absolute value of the clean Ag(001) surface results in  $\Phi_{Ag} = 4.5 \pm 0.1$  eV, which is slightly too high compared with literary values.

Overall the three techniques show no significant change in the metal work function when going from 3 to 8 ML MgO. This indicates that the work function shift is built up within the first layers and is dominated by the MgO/Ag interface. Since the Ag(001) work function with the MgO grown on top decreases, the Fermi level of the Ag is lifted such that the energy levels of Au adatoms, with their high electron affinity, are just below the Fermi level [111, 210, 214]. Therefore electrons can tunnel from the metal support to the metal atom or cluster. Also a charge transfer in the opposite direction has been proposed [214]. The states of deposited K species are just above Fermi level, therefore they will transfer their valence electron to the metal and become positively charged. Charge transfer is of course only possible if the film thickness does not exceed the tunneling length and is therefore an effect related to thin films.

## 4.5 Conclusion

The metal work function shift of 0.5 ML, 3 ML and 8 ML MgO grown on Ag(001) has been investigated. The work function shift is one of the key parameters for charging adsorbed particles having a high electron affinity like Au deposited on defect poor MgO layers. Therefore the work function shift is essential for the catalytic properties of Au/MgO/Ag(001) and makes these thin films a research area in there own right [1, 110], since their behavior is different to Au on thick films or bulk MgO. The CPD measurements average over a surface area with a radius of 10-15 nm. On the 3 and 8 ML film the averaging effect is not an issue and the derived values are in good agreement with the theory. However, on 0.5 ML the averaging of the surface area does effect the detected shift. The resolution could be enhanced at close tip-sample proximities. This resolution enhancement is explained by a simulation. The contribution to the force signal of the atom directly under the tip increases with decreasing tip-sample distance. Nevertheless the CPD value on 0.5 ML is too small and the increase in resolution was limited by tip instabilities. To derive the work function shift from  $I_T(z)$  curves is not straightforward. Moreover, this method is highly affected by the experimental conditions. In consequence it might not be surprising that this method

---

shows the largest standard deviation for the methods used here. The FER analysis on all sample systems agrees with the theory and is featured by their stable detection conditions resulting in a small standard deviation. Beside the interesting research background of the work function and its important role in adsorption processes like in catalysis this paper presents an *in situ* comparison of three independent methods on the same surface area gained by a dual mode DFM/STM setup.

# Chapter 5

## Identification and Characterization of Color Centers

Electron transfer processes play an important role in chemical reactions in general and in catalysis in particular. Surface defects are crucial in catalysis as oxide surfaces are often present either as supports or directly as catalysts. Oxygen vacancies on MgO i.e. color centers are electron trapping sites and are therefore supposed to be involved in electron transfer processes on the MgO surfaces. The trapped electrons in the color centers can be provided to adsorbates such as Au atoms, or color centers can be directly involved in chemical reactions on the surface. In the following color centers on the MgO surface will be identified by their charge state.

### 5.1 Motivation

The perfect MgO surface is quite inert while a defect rich surface shows a high and complex chemical reactivity [2]. To make progress in understanding possible reaction pathways a detailed characterization of color centers is highly desired. Information about their local position and thus coordination, electronic structure, local potential and possible adsorbate interaction are of fundamental interest.

However, to distinguish single point defects on a local scale, techniques having a high lateral resolution are a prerequisite. Therefore a dual mode dynamic force microscope in combination with a scanning tunneling microscope have been employed. The benefit of this dual mode setup is the possibility to employ both techniques on the same surface area with the same tip. Further-

more the setup has been designed for high resolution measurements making it the perfect tool to investigate the properties of interest in real space at the atomic level.

## 5.2 Results and Discussion

To investigate color centers at the atomic level 3 ML and 6 ML MgO thin films have been prepared on Ag(001) in the way presented in section 3.5. However, the presented measurements show the same trends for both film thicknesses. Since the intrinsic defect density of the film is very low  $10^{16}$  to  $10^{18}$  defects/cm<sup>2</sup>, color centers have been generated by operating the microscope in the STM mode at high currents  $I_T = 6$  nA and high voltages  $U_S = 7$  V. Therefore clean and well grown MgO areas have been selected to ensure defined conditions. The defects are preferentially located at kinks, corners and step edges. An FM-DFM image of a MgO step edge with point defects is shown in figure 5.1. Beside FM-DFM images, STM images have been recorded at different

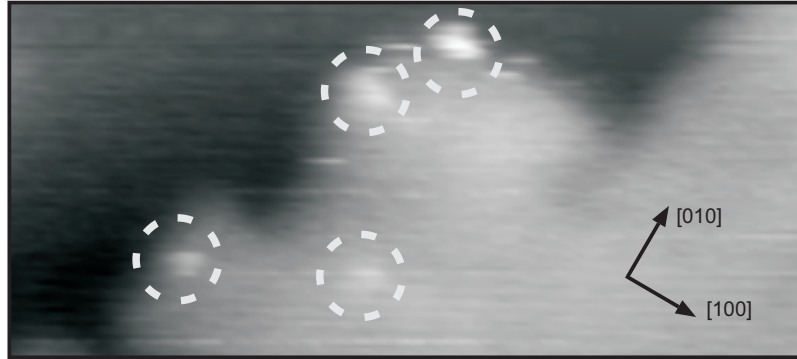


Figure 5.1: FM-DFM image of  $21 \times 9$  nm<sup>2</sup> measured at a resonance frequency shift of  $\Delta f = -1.6$  Hz, an oscillation amplitude of  $A_{osc} = 340$  pm and  $U_S = -50$  mV. Defects are indicated by circles.

bias voltages mapping different available states of the defects (figure 5.2). The  $z$  displacements of both techniques show a strong peak at the position of the defect. From a structural point of view the positions of the defects are "holes" i.e. missing oxygen atoms in the lattice. These measurements with point defect resolution enable tip positioning above the defect. At the position of the defects the feedback either on  $\Delta f$  or  $I_T$  has been switched off to keep the tip height constant. Afterwards the frequency shift vs applied bias voltage has been measured and compared to equivalent measurements at the same height close to the defect. The parabolic behavior of the resonance

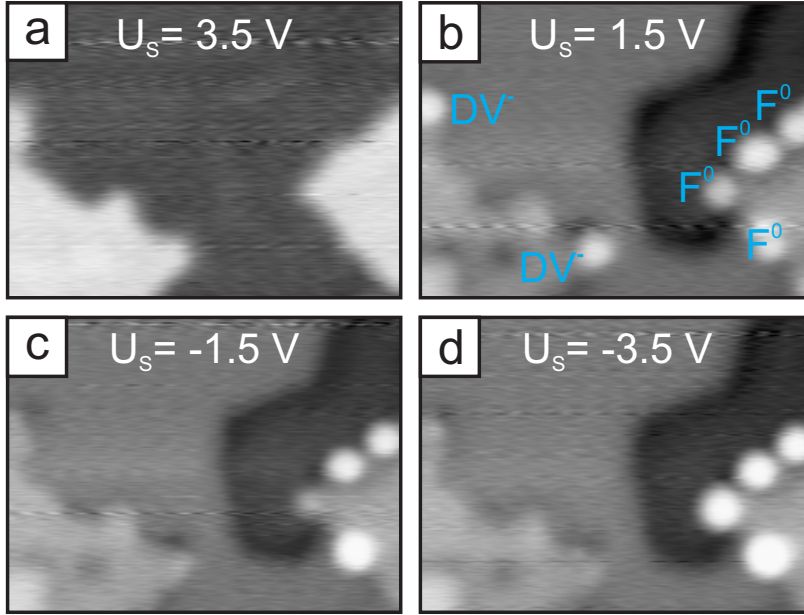


Figure 5.2: STM images at different voltages of point defects on MgO/Ag(001) generated by the tip. Scan range:  $40 \times 30 \text{ nm}^2$ . The point defects can be assigned to negatively charged divacancies ( $DV^-$ ) and  $F^0$  defects. (a) Typical topography STM image of MgO/Ag(001). The positions of the defects are hardly distinguishable from the MgO.  $U_S = 3.5 \text{ V}$ ,  $I_T = 20 \text{ pA}$ . (b) At  $U_S = 1.5 \text{ V}$ ,  $I_T = 20 \text{ pA}$  the defects appear as clear protrusions. (c,d) For  $U_S = -1.5 \text{ V}$  and  $-3.5 \text{ V}$  only the  $F^0$  defects appear as protrusions.

frequency shift curves has been analyzed resulting from the electrostatic force between tip and sample given by [45, 46, 50, 228]

$$F_{el} = \frac{1}{2C_{\Sigma}^2} \frac{\partial C_1}{\partial z} \left( nq + C_2 \left( U_S - \frac{\Delta\Phi_{loc}}{|q|} \right) \right)^2, \quad (5.1)$$

where  $C_{\Sigma}(z) = C_1(z) + C_2$ , with  $C_1(z)$  as the capacity between tip and defect,  $C_2$  as the capacity between defect and substrate. The local defect charge is represented by while  $n$  represents the number of elementary charges. An additional term representing the capacity between the tuning fork's back-electrode and the substrate can be added to equation 5.1, but is irrelevant for point defect resolution.

The electrostatic force is always attractive, due to the parabolic dependency (compare equation 5.1) and therefore independent of the bias voltage sign. Details of the electrostatic tip-sample interaction have been discussed in section 2.3.2. The maximum of the parabola depends on the defect charge

$q$  and the local potential  $\Delta\Phi_{loc}$  also known as the local work function. However, as measured and discussed in chapter 4 the MgO thin film shifts the Ag(001) work function by about 1.1 eV. This level is set as the reference level measured on the MgO surface and relative shifts are related to this level. From measurements of numerous defects four different types have been distinguished by their maximum position of the resonance frequency shift vs bias voltage parabola. The results are collocated in figure 5.3.

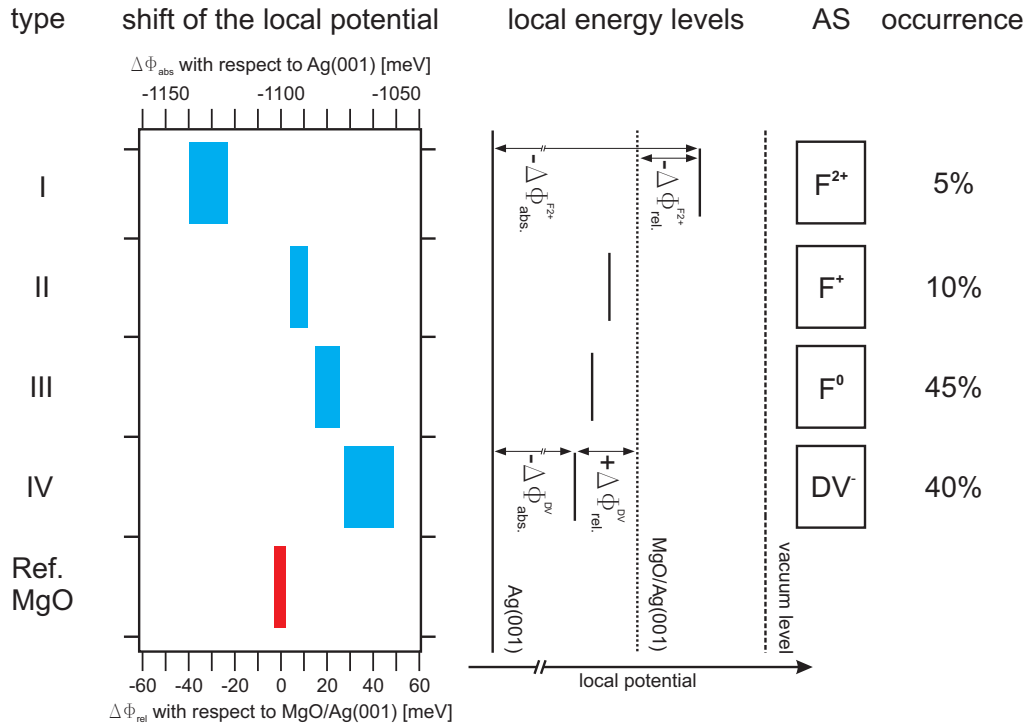


Figure 5.3: The left labeling assigns numbers to the defects. The graph shows the relative shift of the local potential  $\Delta\Phi_{rel}$  with respect to the MgO surface (bottom abscissa) and the absolute shift  $\Delta\Phi_{abs}$  with respect to the Ag(001) level (top abscissa), both shifts include the local charge. The covered range in the shifts results from measurements with different local resolutions due to different tip structures. The energy level scheme presents the different energy level of the defect types and their local potential shifts. The labeling on the right gives the assignment (AS) of the defect types.

To the left in figure 5.3 the four types are indicated by numbers and the MgO reference level is given (red bar). The graph presents the positions of the maxima of the parabolas with respect to the reference MgO level (bottom abscissa) and with respect to the Ag(001) level (top abscissa), while the energy scheme shows the energetic levels and their shifts.

For type I defects shifts of  $-50$  to  $-25$  meV below the MgO level have been observed. These significant shifts can be explained by the presence of positively charged defects with respect to the surrounding area resulting in a decrease in the local potentials as indicated in the local energy scheme in figure 5.3. The charge density distribution is significantly reduced at the positions of the defects compared with the surrounding MgO lattice as shown in figure 5.4(a). The presence of charges localized at the positions of the defects induces a work function shift in the Ag(001) substrate in analogy to the Helmholtz equation [218]  $\Delta\Phi = 4\pi e\mu\sigma$ , where  $\mu$  is the dipole moment induced by the localized charge at the site of the defect and the screening charge in the Ag(001) substrate,  $\sigma$  is the surface concentration and  $e$  is the elementary electron charge. However, the full complexity is not covered by the Helmholtz equation and calculations are still desired.

For defect type II the shift changes its sign and shows a shift of  $\approx +9$  meV. This shift can be assigned to an  $F^+$ . For an  $F^+$  the overall charge is positive, but on a very local scale the single electron has a probability above the surface as derived by density functional calculations [118, 196]. The charge density distribution for an  $F^+$  center is plotted in figure 5.4(b). The charge density spills out of the site of the defect and has therefore a probability above the surface. The spill out of the negative charge changes the local dipole moment such that the local potential increases compared with the MgO/Ag(001) reference level. The electron charge is symmetrically distributed along the surface normal with its charge maximum located in the center of the defect.

Defect type III results in a shift of about  $+15$  to  $+20$  meV above the MgO level. The shift results from two charges present in a defect site and is thus attributed to an  $F^0$  color center. An  $F^0$  is neutral compared to the surrounding MgO lattice, but due to Coulomb repulsion the two electrons have a large probability density above the surface as visible in figure 5.4(c). The charges are as for type II symmetrically distributed and located in the center of the defect. Therefore the charge does not belong to any  $Mg^{2+}$  site surrounding the defect. Thus the oxidation state of the surrounding lattice is not affected by the trapped charges. The spill out of the charges results in a stronger dipole moment compared to defect type II. Overall the measured shift is about twice as large as that for defect type II.

The strongest positive shift on the relative scale is that of type IV. The strong shift indicates that negative charges might be involved. Therefore this shift might result from divacancies (DV) or OH groups trapped at low coordinated  $Mg^{2+}$  sites. It is known that OH groups can trap electrons [229]. However, OH groups and other adsorbates can be excluded since all defects occur only after high voltage and high current scanning and are not present

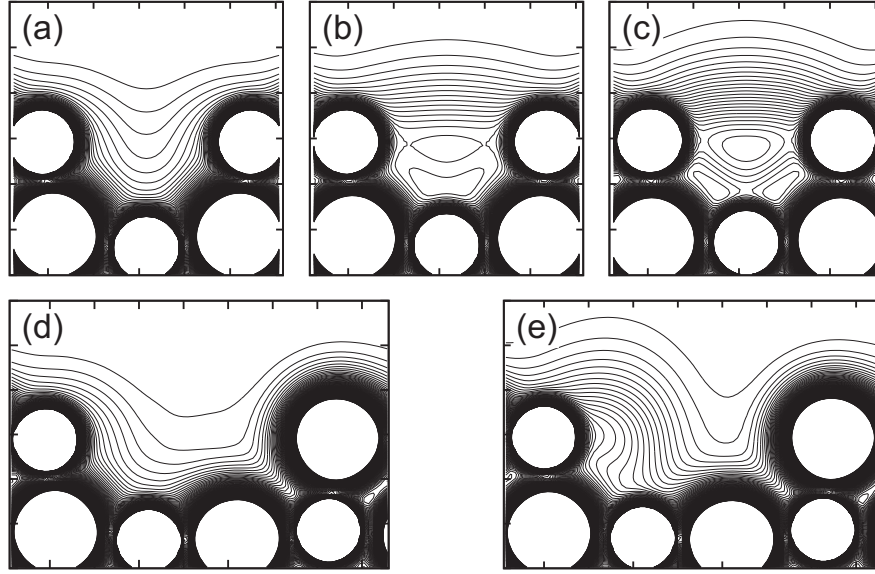


Figure 5.4: Charge density distributions of (a)  $F^{2+}$ , (b)  $F^+$ , and (c)  $F^0$  color centers. Size of (a-c)  $6 \times 6 \text{ nm}^2$ . (d) Charge density distribution of a neutral divacancy and (e) a negative divacancy with a trapped electron. Size of (d, e)  $8.5 \times 6 \text{ nm}^2$ . Isolines separation (a-e):  $8 \times 10^{-3} \text{ e}/\text{\AA}^3$ , cutted off at  $0.5 \text{ e}/\text{\AA}^3$ . DFT calculations were performed in the workgroup of G. Pacchioni, Milano, Italy. With courtesy of G. Pacchioni.

on regular terraces and steps. With the scan parameters discussed above, adsorbates would be removed from the scan area. Furthermore the defects occur only within the scanned frame and not outside. Therefore favored candidates are divacancies formed at step and corner sites since the formation energy is lowest here. The stability of divacancies and their electron affinity for trapping electrons have been confirmed by DFT calculations [183]. A divacancy is neutral compared with the surrounding MgO, since a Mg-O unit is missing. Due to the electron affinity of  $0.6 - 1 \text{ eV}$  electrons can be trapped by the DV for example from the tunneling junction and the DV becomes negatively charged. The charge density distributions of a neutral DV and charged  $DV^-$  are depicted in figure 5.4(d) and (e) respectively. The trapped electron of the  $DV^-$  is strongly localized at the  $Mg^{2+}$  site due to the attractive Coulomb interaction. Since the  $DV^-$  is negatively charged with respect to the surrounding MgO area the additional dipole moment will increase the work function resulting in the largest positive shift on the relative scale. The covered ranges in the maximum positions are supposed to originate from different tip structures however the reproducibility for two

measurements directly after each other is within  $\pm 2$  meV. Therefore all defects types analyzed show a characteristic *fingerprint* due to different charge states.

The measurements based on FM-DFM are supported by complementary STS measurements. The STS measurements have been performed directly after the local contact potential measurements without moving the tip laterally. Thus for all defects the local density of states (LDOS) has been detected. To prevent tip changes, when doing STS at high voltages, the feedback on the tunneling current was switched on, and  $dz/dU_S$  was detected. The discussion of this technique is given in section 2.4.4. The spectra measured on the defects are compared with MgO spectra on the terrace next to the defect. The MgO reference spectra show no peaks within the voltage regime due to the band gap (compare figure 5.5 red lines). The spectra taken on the

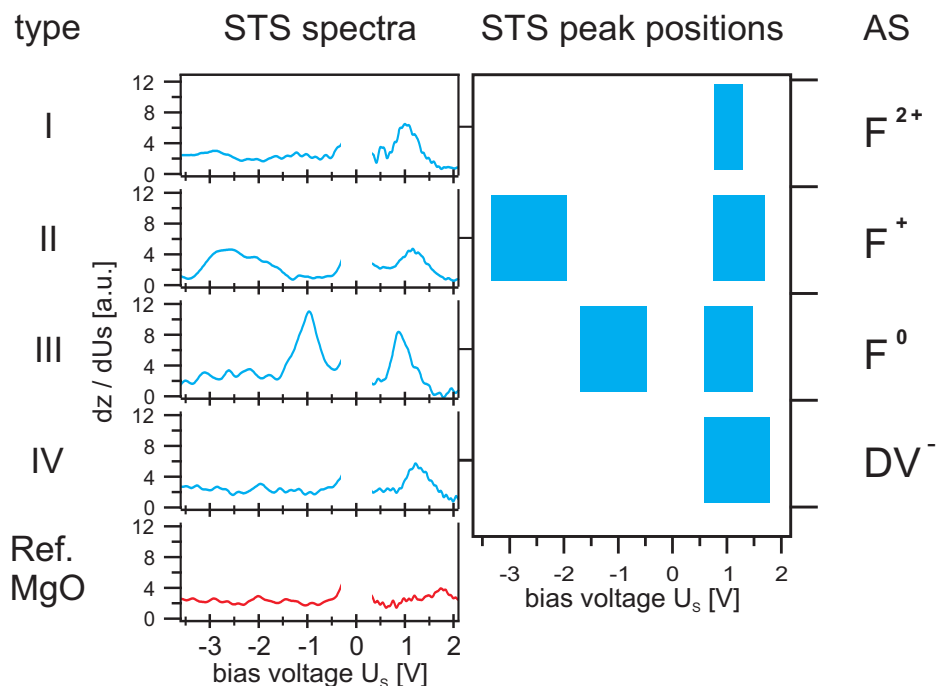


Figure 5.5: The left labels indicate the defect types by numbers. The left graph shows STS spectra of the respective defect. The right graph presents the maxima of the STS data. The covered abscissa range accounts for the statistics of the peak positions. The identification of defect types with color centers and negatively charged divacancies ( $DV^-$ ) according to the theory is implemented to the right.

$F^{2+}$  show peaks only in the unoccupied regime at voltages of  $\approx +1$  V above the Fermi level (see figure 5.5). The  $F^+$  centers have both occupied and

unoccupied electronic states within the band gap. The electronic states are located within the band gap of MgO. The occupied states are quite broadly distributed from  $-3.5$  V to  $-2.0$  V below the Fermi level, depending on the defect location on the film [95]. The empty states are at  $\approx +1$  V above the Fermi level. Considering the  $F^0$  color center the doubly occupied state is higher in energy  $\approx -1$  V below the Fermi level, while the position of the unoccupied state is similar to  $F^+$  centers.

The negatively charged divacancies only show a clear feature in the empty states at about  $+1$  V. The corresponding occupied shallow state is expected to be very close to the Fermi level, i.e. in a region where the experiment cannot clearly detect states. However  $F^0$  and  $DV^-$  are equally frequent and represent  $\approx 85$  % of the total defects.  $F^+$  color centers are much less frequent  $\approx 10$  % and  $F^{2+}$  centers about 5 %. These findings are in good agreement with the high formation energies of  $F^{2+}$  centers. By comparing the STS peak positions in figure 5.5 it becomes obvious that  $F^{2+}$  and  $DV^-$  defects are hardly distinguishable by their electronic structure but show a significant difference in the local potential due to the effect of the locally trapped charge on the surface dipole.

### 5.3 Conclusion

Four of the major defect types on MgO, which are those the mostly discussed in literature, have been characterized by their charge state and finally identified by complementary application of FM-DFM and STS in combination with DFT results [118]. The preferential positions of the defects at corners, kinks and steps could be confirmed. In addition the local potential based on the charge state and electronic signature has been measured and analyzed. The electronic states of the defects are located within the band gap of the MgO surface. The identification of surface defects by FM-DFM was performed for the first time. This possibility of FM-DFM opens the way to investigate bulk oxide systems in more detail in the future, which is however, not possible by STM, since it is limited to conducting samples.

# Chapter 6

## Attractive Interaction on $F^0$ Color Centers

This chapter discusses the interaction of metal atoms and clusters with an  $F^0$  color center as one of the most frequent color centers on the MgO surface. The adsorbate defect interaction has been mimicked by a dynamic force microscope tip measuring the interaction with an  $F^0$  defect on the MgO(001) surface. The experimental findings are complemented by density functional theory calculations performed in the workgroup of Gianfranco Pacchioni.

### 6.1 Motivation

The influence of color centers on chemical reactions is intensively discussed in literature. From calculations it has been proposed that color centers are directly involved in chemical reactions [181, 182] e.g. as adsorption sites due to more attractive defect adsorbate interactions compared with the pristine MgO surface. However, in principle color centers could be indirectly involved in chemical reactions since they might be less attractive compared with regular sites, forcing adsorbates into local energy minima far away from the positions of the defects. In the following for the first time experimental measurements show whether  $F^0$  color centers are attractive or repulsive with respect to the surrounding MgO lattice.

### 6.2 Results and Discussion

The experiments have been performed on 3 and 6 ML MgO thin MgO films with no significant difference. The MgO films have been prepared, as discussed in section 3.5. Starting points were clean and well grown MgO sur-

faces. The defects were created by scanning the MgO surface at high voltages  $U_S = 7$  V and currents  $I_T = 6$  nA. Typical adsorbates desorb at these scanning conditions and can therefore be excluded as possible protrusions within the observed images. The defects were characterized by contact potential and STS measurements as described in chapter 5.

The perfect tool to analyze the interaction of an adsorbate with a color center is the dynamic force microscope. Based on the high local resolution FM-DFM images as shown in figure 5.1 are the starting point for adsorbate defect interaction studies. The tip, representing the adsorbate, scans laterally across the defect positions at constant height along the step direction. The simultaneously measured resonance frequency shift  $\Delta f$  and tunneling current  $I_T$  give insights into the local surface potential as well as into the local electronic structure. The corresponding results of such an experiment are shown in figure 6.1 where the tip scans across an  $F^0$  defect. The identification of the color center has been performed in analogy with chapter 5. The three stacked graphs show the simultaneously recorded oscillation amplitude, the resonance frequency shift and the tunneling current. The colored traces indicate constant height scans at different tip-sample separations. At the different tip-sample distances the oscillation amplitude can be considered as constant, which is a prerequisite, since the frequency shift scales with amplitude (compare equation 2.28 and Ref. [61]).

Since the tunneling current exponentially depends on the tip-sample distance, at the largest separation it vanishes and the resonance frequency shift is a consequence of the long range force background arising from electrostatic and van-der-Waals forces. The averaged resonance frequency shift at the largest separation is about  $\Delta f = -0.52$  Hz. By decreasing the tip-sample distance by  $0.5$  Å the modulus of the tunneling current and the resonance frequency shift increase at the position of the defect. The tunneling current results in  $I_T = -0.5$  nA and the resonance frequency shift in  $\Delta f = -0.75$  Hz at the position of the defect. Decreasing the tip-sample separation by another  $0.5$  Å results in a tunneling current of  $I_T = -9.9$  nA and a resonance frequency shift of  $\Delta f = -1.13$  Hz at the position of the defect. Despite the decrease of  $1.0$  Å in tip-sample distance, the average tunneling current on the regular MgO terrace stays below  $I_T = -0.05$  nA. The resonance frequency shift changes by  $0.15$  Hz with the tip-sample distance decreasing. This experiment demonstrates the highly attractive interaction with an  $F^0$  center.

It has been debated in literature how color centers are imaged by FM-DFM [230, 231] since a color center is a hole in the MgO lattice [2]. However, no FM-DFM measurements on defined defects of the MgO surface have been presented in literature so far. The arising question is: Why are the  $F^0$  center so highly attractive? The attraction results from the charge density of the

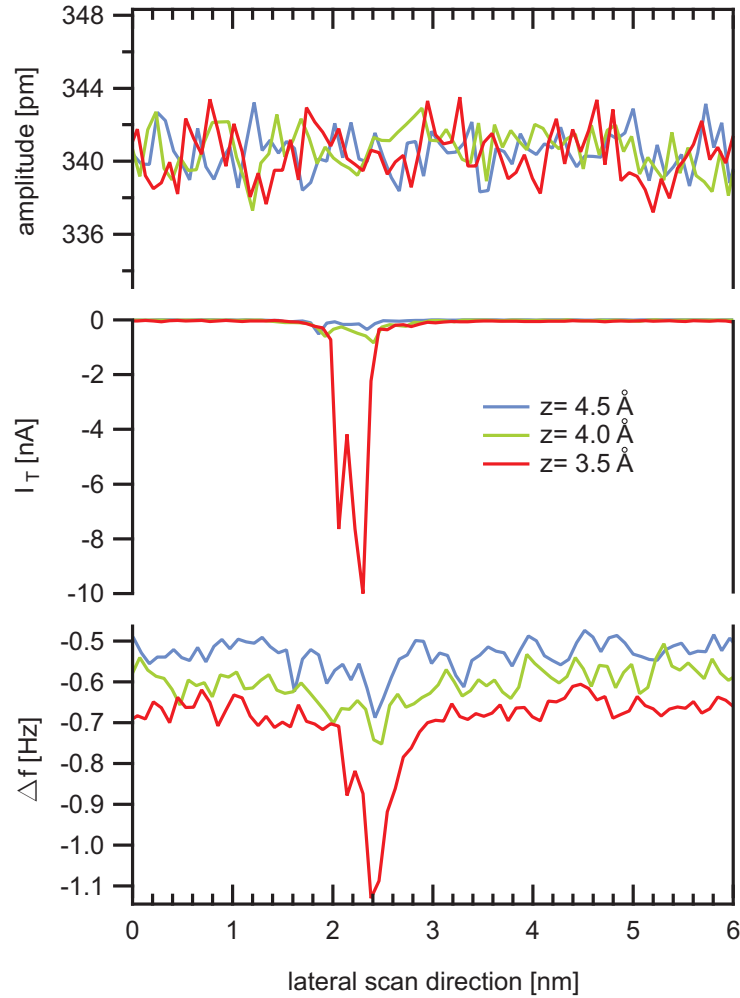


Figure 6.1: Constant height linescans across an  $F^0$  defect situated at a step edge. The scan direction is along the step edge. The three presented channels have been measured simultaneously. The colors indicate different tip-sample distances. Note that the displacement of  $4.5 \text{ \AA}$  has been chosen arbitrarily, since absolute values are generally unknown in scanning probe microscopy. The top graph shows the oscillation amplitude. The amplitude is constant during scan process. This excludes artefacts in frequency shift. The graph in the middle presents the tunneling current and the graph at the bottom shows the resonance frequency shift. Data has been taken at a bias voltage of  $U_S = -50 \text{ mV}$ .

two electrons trapped located in the center of the defect site. Due to the Coulomb repulsion the two electrons trapped, repel each other and spill out of the defect site into vacuum [118]. Therefore a considerably large charge

density is above the surface. This charge density is supposed to interact with the tip resulting in a strong attraction, as presented in figure 6.1. Since the doubly occupied  $F^0$  state is close to the Fermi level of the MgO/Ag(001) system [95], the charge density is also responsible for the strong peak in the tunneling current signal.

To gain further insights into the interaction of tip and color center periodic supercell DFT calculations at the level of the generalized gradient approximation as implemented in the VASP code [224, 225] have been performed in the workgroup of Gianfranco Pacchioni. The  $Pt_{0.9}/Ir_{0.1}$  tip has been modeled by a tetrahedral  $Pt_4$  cluster, whose geometry has been relaxed separately. The  $F^0$  color center has been created by removing an O atom from the top layer of a three layer MgO slab. The structure of the slab with the color center has been relaxed. The tip surface interaction energy has been computed as a function of tip-sample distance of the apical  $Pt_4$  tip with respect to the top layer of the MgO slab [see inset in figure 6.2(b)]. During these calculations the separately optimized tip structure was not allowed to relax. However, the relaxation of the MgO surface has been found to be very small for the calculated distances where no direct contact is established. The outward relaxation of the O anion at 3.5 Å is about 0.12 Å.

The results of the experimental distance related measurements and the corresponding theoretical results are presented in figure 6.2(a,b) respectively. The experimental results, as derived from figure 6.1, show a significantly stronger interaction on top of the defect than on the regular MgO surface as previously discussed. Note that the absolute  $z$  displacement in the experimental data is not known with precision in the experiment and is supposed to be around 4.0 Å, since the tunneling current is fairly small on the terrace. However, the comparison of experimental and theoretical data can only be done qualitatively since the exact shape and composition of the tip are not known, but have a strong influence on the absolute energy value. Since the experimental results have been highly reproducible with the same qualitative behavior and the scan process did not show any contrast changes nor tip instabilities, a metallic tip has been assumed. Due to the tip composition of  $Pt_{0.9}/Ir_{0.1}$  Pt atoms are very likely tip atoms. The frequency shift scales with energy (compare equation 2.33), hence a qualitative agreement between experimentally detected frequency shift [figure 6.2(a)] and the theoretical calculations [figure 6.2(b)] is well established. The blue dotted line in figure 6.2(b) shows the interaction of the  $Pt_4$  tip with a regular oxygen site of the MgO surface, while the red solid line represents the interaction with an  $F^0$  color center.

The interaction with a cation site is not explicitly discussed, since interaction has been found to be considerably smaller. At a distance of 5.0 Å from

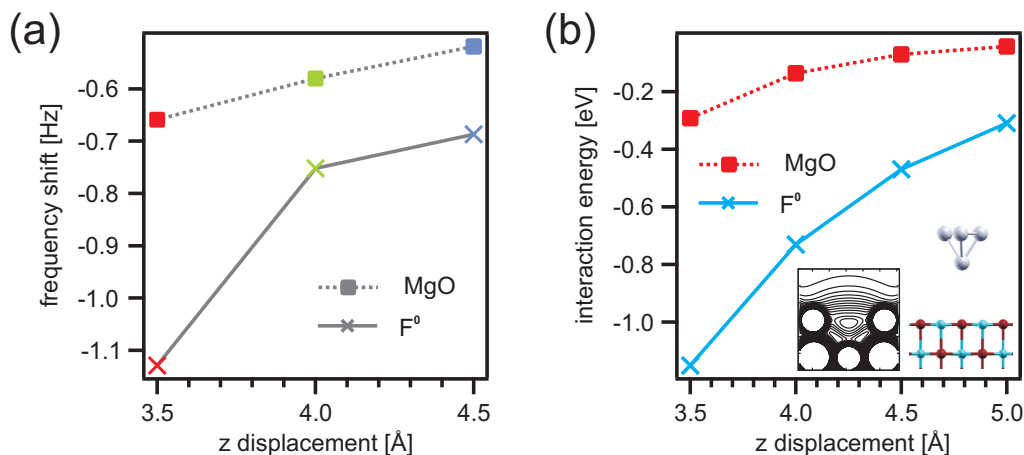


Figure 6.2: (a) Resonance frequency shift of a  $Pt_{0.9}/Ir_{0.1}$  tip on a regular MgO surface (rectangles) and above an  $F^0$  defect site (crosses). Experimental data are derived from the constant height measurements shown in figure 6.1. The resonance frequency shift is a direct consequence resulting from potential gradients between tip and sample. By integration the frequency shift is related to the potential energy [61]. (b) Interaction energy of a  $Pt_4$  cluster above the O site of a MgO surface (rectangles) and above an  $F^0$  defect center (crosses) calculated by DFT. The insets show the spill over of the electron charge density of an  $F^0$  center and the  $Pt_4$  cluster above the MgO surface.

the MgO surface the interaction energy with an oxygen site is nearly zero [0.04 eV, see figure 6.2(b)] and thus significantly smaller compared with the  $F^0$  site (0.31 eV) at 5.0 Å. With the tip-sample distance decreasing the interaction on both sites increase, but at the position of the defect the interaction is more strongly attractive. For a distance of 3.5 Å the interaction energy is 0.29 eV at a regular oxygen site while at the  $F^0$  center site it is 1.15 eV. At a distance of 2.5 Å when tip and surface are nearly in contact very strong interactions of 1.26 eV on the oxygen site and 2.67 eV at the  $F^0$  site occur. At this distance an electron transfer process occurs from the defect to the  $Pt_4$  cluster/tip, which becomes negatively charged (Bader analysis). The charge transfer process is an indication of a strong overlap of wave functions from the  $Pt_4$  cluster and the  $F^0$  center. Therefore the critical distance for the charge transfer to happen is about 3.0 Å.

However, the attractive interaction of metal cluster/tip and defect is already sensed about 5.0 Å above the position of the defect. The minima 1.7 eV and 4.1 eV of the interaction potential energy curves calculated for the tip-sample interaction are located at about 2.0 Å and 1.4 Å for the oxygen site and  $F^0$  site respectively. At closer distances the interaction rapidly becomes

repulsive. To clarify the influence of the tip structure on the interaction potential and the charge transfer a single Pd atom and an extended two layer Pt surface representing a large flat tip have been used, and their interaction potential with the MgO surface have been analyzed. The Pd atom was chosen because of its small electron affinity  $\approx 0.6$  eV [232] compared with  $\approx 2.5$  eV [233] for a Pt<sub>4</sub> cluster. It is obvious that the interactions for the different tip types and structures is totally different. The qualitative feature of a much stronger interaction with the F<sup>0</sup> site compared with the regular oxygen and magnesium sites is well reproduced and therefore supposed to be a general feature of F<sup>0</sup> centers [116]. Also for these two tips a charge transfer occurs at about 2.5 Å. It is important to note that the DFT calculations do not account for van-der-Waals interactions, however the chemical forces are clearly dominant over the dispersion forces.

The reason why the defect site is imaged in the FM-DFM mode at constant resonance frequency shift as a protrusion results from the difference in gradient of the interaction potential (0.39 eV/Å as computed with the Pt<sub>4</sub> cluster in the interval of 3.5 to 5 Å) and the long range characteristic of the interaction at the site of the defect. Recent calculations considered this effect [231], but with an oxide tip which leads to a much smaller gradient (0.1 eV/Å). However, they did not take electrostatic interaction into account.

## 6.3 Conclusion

FM-DFM measurements supported by supercell DFT calculations show a highly attractive tip-defect (F<sup>0</sup>) interaction which is quite long range in character. Due to the high local resolution and the used FM-DFM technique, the attractive interaction has been detected in a direct manner. This direct manner allows to probe electron trapping sites as preferred adsorption sites. The highly attractive interaction results from charge density of the two electrons trapped, protruding into the vacuum. The presented analysis underlines the role of trapped charges in important adsorption, nucleation and growth processes on surfaces.

# Chapter 7

## Conclusions and Outlook

One of the aims of this thesis was to investigate color centers on the surface of thin MgO films grown on Ag(001) to gain in understanding of their role in chemical reactions on the surface. Some of the properties of the color centers have been confirmed and extended. The natural concentration of color centers has been found to be quite low. By electron bombardment from the tunneling junction the concentration on the surface can be increased leading to defects preferentially located at steps, kinks and corners, since the formation energy is highly reduced at these surface sites. The charge state of the color centers could be determined from a characteristic shift in local potential. The shift in the local potential results in a shift in the saddle of the electrostatic tip-sample interaction. By performing local potential measurements with point defect resolution for the first time the charge state of single point defects has been analyzed by DFM. Furthermore,  $F^{2+}$  centers have been identified by DFM while their defect states are indistinguishable from divacancies by STS. The STS data of  $F^0$  and  $F^+$  centers have been confirmed by their defect states within the MgO band gap. The experimental data have been supported by DFT calculations and show a good correspondence.

Furthermore, the interaction of an  $F^0$  color center with a metal cluster mimicked by the DFM/STM metal tip has been investigated. On top of the defect the frequency shift as well as the tunneling current show a strong increase in signal. By investigations at different tip-sample distances it becomes obvious that the attractive interaction of the metal tip with the  $F^0$  center reaches quite far into vacuum and the defect is therefore already sensed by a metal cluster *far away* in comparison with the pristine MgO surface. Thus color centers are preferred adsorption sites for metal particles. Since the DFM is directly sensitive to forces these measurements present for the first time a direct prove of attractive metal cluster defect interactions. The attractive interaction trend broadly corresponds with DFT calculations.

---

The calculations by Gianfranco Pacchioni show that the metal tip strongly interacts with the two electrons trapped at the side of the defect.

The presence of the MgO layers on the Ag(001) support shifts the Ag work function. Since the work function is supposed to be one of the key parameters for charging adsorbates, the impact of different MgO film thicknesses on the work function has been analyzed. By employing three different methods, one referring to DFM and two to STM, work function shift has been observed and found to be almost fully established within the first MgO layer. For MgO films of 3 and 8 monolayers the work function is constant. From these measurements it has been concluded that the work function shift results from the interface since it is almost built up after one monolayer of MgO. Thus these work function shift measurements support theoretical work suggesting a reduction of the surface work function due to a decrease of the surface dipole since the Ag electrons cannot overspill into the vacuum as strongly as with a MgO film present.

All the measurements of the electrostatic tip-sample interaction were based on the analysis and characterization of the electrostatic tip-sample interaction in full parameter space. These investigations have been the starting point for the work function analysis and used to gain single point defect resolution in electrostatic force measurements.

The high real space resolution of the setup employed allows the analysis of MgO bulk systems, since DFM is not limited to conducting samples. Therefore in the future it should be possible to perform a detailed study of color centers on bulk MgO systems. The results derived from the thin films might be used as a reference for these measurements. The investigation of defects on bulk MgO would be another step away from model systems towards systems used in industry.

Another interesting possibility would be to adsorb molecules like benzene or pentacene on MgO. Once the molecules have been imaged on the surface, the electrostatic interaction at specific sites could be detected. Such measurements might correlate charge distributions of the molecule to electrostatic tip sample interactions.

In addition larger structures such as dislocations and domains can be investigated and their electrostatic contribution to the interaction analyzed. These special types of defects in the film are supposed to contribute to many adsorption processes and therefore in chemical reactions.

# Bibliography

- [1] H.-J. Freund. Metal-supported ultrathin oxide film systems as designable catalysts and catalyst supports. *Surf. Sci.*, 601:1438–1442, 2007.
- [2] G. Pacchioni. *Theory of point defects at the MgO surface*, chapter 3, pages 94–135. Elsevier, 2001.
- [3] G. Binnig, H. Rohrer, Ch. Gerber, and E. Weibel. Surface Studies by Scanning Tunneling Microscopy. *Phys. Rev. Lett.*, 49:57–61, 1982.
- [4] G. Binnig and H. Rohrer. Nobel lecture: Scanning tunneling microscopy - from birth to adolescence, 1986.
- [5] J. Tersoff and D. R. Hamann. Theory of the scanning tunneling microscope. *Phys. Rev. B*, 31:805–813, 1985.
- [6] S. Schintke and W.-D. Schneider. Insulators at the ultrathin limit: electronic structure studied by scanning tunnelling microscopy and scanning tunnelling spectroscopy. *J. Phys.: Condens. Matter*, 16:R49–R81, 2004.
- [7] X. Lin, N. Nilius, H.-J. Freund, M. Walter, P. Frondelius, K. Honkala, and H. Häkkinen. Quantum Well States in Two-Dimensional Gold Clusters on MgO Thin Films. *Phys. Rev. Lett.*, 102:206801, 2009.
- [8] N. Nilius, T. M. Wallis, and W. Ho. Development of One-Dimensional Band Structure in Artificial Gold Chains. *Science*, 297:1853–1856, 2002.
- [9] J. Repp, G. Meyer, S. M. Stojković, A. Gourdon, and C. Joachim. Molecules on Insulating Films: Scanning-Tunneling Microscopy Imaging of Individual Molecular Orbitals. *Phys. Rev. Lett.*, 94:026803, 2005.

- 
- [10] N. Nilius, M. V. Ganduglia-Pirovano, V. Brázdová, M. Kulawik, J. Sauer, and H.-J. Freund. Counting Electrons Transferred through a Thin Alumina Film into Au Chains. *Phys. Rev. Lett.*, 100:096802, 2008.
- [11] M. F. Crommie, C. P. Lutz, and D. M. Eigler. Confinement of Electrons to Quantum Corrals on a Metal Surface. *Science*, 262:218–220, 1993.
- [12] E. J. Heller, M. F. Crommie, C. P. Lutz, and D. M. Eigler. Scattering and absorption of surface electron waves in quantum corrals. *Nature*, 369:464–466, 1994.
- [13] N. Nilius, N. Ernst, and H.-J. Freund. Photon Emission Spectroscopy of Individual Oxide-Supported Silver Clusters in a Scanning Tunneling Microscope. *Phys. Rev. Lett.*, 84:3994–3997, 2000.
- [14] R. Berndt, J. K. Gimzewski, and P. Johansson. Inelastic tunneling excitation of tip-induced plasmon modes on noble-metal surfaces. *Phys. Rev. Lett.*, 67:3796–3799, 1991.
- [15] B. C. Stipe, M. A. Rezaei, and W. Ho. Single-Molecule Vibrational Spectroscopy and Microscopy. *Science*, 280:1732–1735, 1998.
- [16] H. J. Lee and W. Ho. Single-Bond Formation and Characterization with a Scanning Tunneling Microscope. *Science*, 286:1719–1722, 1999.
- [17] J. I. Pascual, J. J. Jackiw, Z. Song, P. S. Weiss, H. Conrad, and H.-P. Rust. Adsorbate-Substrate Vibrational Modes of Benzene on Ag(110) Resolved with Scanning Tunneling Spectroscopy. *Phys. Rev. Lett.*, 86:1050–1053, 2001.
- [18] J. I. Pascual, N. Lorente, Z. Song, H. Conrad, and H.-P. Rust. Selectivity in vibrationally mediated single-molecule chemistry. *Nature*, 423:525–528, 2003.
- [19] K. Tomatsu, K. Nakatsuji, T. Iimori, Y. Takagi, H. Kusunohara, A. Ishii, and F. Komori. An Atomic Seesaw Switch Formed by Tilted Asymmetric Sn-Ge Dimers on a Ge (001) Surface. *Science*, 315:1696–1698, 2007.
- [20] S. Heinze, M. Bode, A. Kubetzka, O. Pietzsch, X. Nie, S. Blugel, and R. Wiesendanger. Real-Space Imaging of Two-Dimensional Antiferromagnetism on the Atomic Scale. *Science*, 288:1805–1808, 2000.

- [21] O. Pietzsch, A. Kubetzka, M. Bode, and R. Wiesendanger. Observation of Magnetic Hysteresis at the Nanometer Scale by Spin-Polarized Scanning Tunneling Spectroscopy. *Science*, 292:2053–2056, 2001.
- [22] A. Wachowiak, J. Wiebe, M. Bode, O. Pietzsch, M. Morgenstern, and R. Wiesendanger. Direct Observation of Internal Spin Structure of Magnetic Vortex Cores. *Science*, 298:577–580, 2002.
- [23] G. Binnig, C. F. Quate, and Ch. Gerber. Atomic Force Microscope. *Phys. Rev. Lett.*, 56:930–933, 1986.
- [24] T. R. Albrecht, P. Grütter, D. Horne, and D. Rugar. Frequency modulation detection using high-Q cantilevers for enhanced force microscope sensitivity. *J. Appl. Phys.*, 69:668–673, 1991.
- [25] E. Henderson, P.G. Haydon, and D.S. Sakaguchi. Actin filament dynamics in living glial cells imaged by atomic force microscopy. *Science*, 257:1944–1946, 1992.
- [26] L. Chang, T. Kious, M. Yorgancioglu, D. Keller, and J. Pfeiffer. Cytoskeleton of living, unstained cells imaged by scanning force microscopy. *Biophys. J.*, 64:1282–1286, 1993.
- [27] K. A. Barbee, P. F. Davies, and R. Lal. Shear stress-induced reorganization of the surface topography of living endothelial cells imaged by atomic force microscopy. *Circ. Res.*, 74:163–171, 1994.
- [28] R. Lal and S. A. John. Biological applications of atomic force microscopy. *Am. J. Physiol.*, 266:C1, 1994.
- [29] H. J. Butt, K. H. Downing, and P. K. Hansma. Imaging the membrane protein bacteriorhodopsin with the atomic force microscope. *Biophys. J.*, 58:1473–1480, 1990.
- [30] D. L. Worcester, H. S. Kim, R. G. Miller, and P. J. Bryant. Imaging bacteriorhodopsin lattices in purple membranes with atomic force microscopy. *J. Vac. Sci. Technol. A*, 8:403–405, 1990.
- [31] F. J. Giessibl. Atomic Resolution of the Silicon (111)-(7×7) Surface by Atomic Force Microscopy. *Science*, 267:68–71, 1995.
- [32] Ch. Loppacher, M. Bammerlin, M. Guggisberg, S. Schär, R. Bennewitz, A. Baratoff, E. Meyer, and H.-J. Güntherodt. Dynamic force microscopy of copper surfaces: Atomic resolution and distance depen-

- dence of tip-sample interaction and tunneling current. *Phys. Rev. B*, 62:16944–16949, 2000.
- [33] T. König, G. H. Simon, H.-P. Rust, and M. Heyde. Atomic resolution on a metal single crystal with dynamic force microscopy. *Appl. Phys. Lett.*, 95:083116, 2009.
- [34] C. Barth and M. Reichling. Imaging the atomic arrangements on the high-temperature reconstructed  $\alpha$ -Al<sub>2</sub>O<sub>3</sub>(0001) surface. *Nature*, 414: 54–57, 2001.
- [35] M. Heyde, G. H. Simon, H.-P. Rust, and H.-J. Freund. Probing Adsorption Sites on Thin Oxide Films by Dynamic Force Microscopy. *Appl. Phys. Lett.*, 89:263107, 2006.
- [36] M. Heyde, M. Sterrer, H.-P. Rust, and H.-J. Freund. Frequency modulated atomic force microscopy on MgO(001) thin films: interpretation of atomic image resolution and distance dependence of tip-sample interaction. *Nanotechnology*, 17:S101–S106, 2006.
- [37] Y. Sugimoto, M. Abe, S. Hirayama, N. Oyabu, O. Custance, and S. Morita. Atom inlays performed at room temperature using atomic force microscopy. *Nature Mater.*, 4:156–159, 2005.
- [38] F. J. Giessibl. High-speed force sensor for force microscopy and profilometry utilizing a quartz tuning fork. *Appl. Phys. Lett.*, 73:3956–3958, 1998.
- [39] F. J. Giessibl. *Noncontact Atomic Force Microscopy*. Springer, 2002.
- [40] J. Israelachvili. *Intermolecular & Surface Forces*. Academic Press, 1991.
- [41] R. P. Feynman. Forces in Molecules. *Phys. Rev.*, 56:340–343, 1939.
- [42] C. J. Chen. *Introduction to Scanning Tunneling Microscopy*. Oxford University Press, Oxford, 2008.
- [43] F. London. Zur Theorie und Systematik der Molekularkräfte. *Z. Physik*, 63:245–258, 1930.
- [44] W. T. Lord Kelvin. Contact Electricity of Metals. *Phil. Mag.*, 46: 82–120, 1898.

- [45] R. Stomp, Y. Miyahara, S. Schaer, Q. Sun, H. Guo, P. Grütter, S. Studenikin, Ph. Poole, and A. Sachrajda. Detection of Single-Electron Charging in an Individual InAs Quantum Dot by Noncontact Atomic-Force Microscopy. *Phys. Rev. Lett.*, 94:056802, 2005.
- [46] R. Waser. *Nanoelectronics and Information Technology, Advanced Electronic Materials and Novel Devices*. Wiley, 2 edition, 2005.
- [47] V. Palermo, M. Palma, and P. Samorì. Electronic Characterization of Organic Thin Films by Kelvin Probe Force Microscopy. *Adv. Mater.*, 18:145–164, 2006.
- [48] M. Kiskinova, G. Pirug, and H.P. Bonzel. Coadsorption of potassium and CO on Pt(111). *Surf. Sci.*, 133:321 – 343, 1983.
- [49] M. Sterrer, T. Risse, U. Martinez Pozzoni, L. Giordano, M. Heyde, H.-P. Rust, G. Pacchioni, and H.-J. Freund. Control of the Charge State of Metal Atoms on Thin MgO Films. *Phys. Rev. Lett.*, 98:096107, 2007.
- [50] T. König, G. H. Simon, H.-P. Rust, G. Pacchioni, M. Heyde, and H.-J. Freund. Measuring the Charge State of Point Defects on MgO/Ag(001). *J. Am. Chem. Soc.*, 131:17544–17545, 2009.
- [51] H. Hölscher, W. Allers, U. D. Schwarz, A. Schwarz, and R. Wiesendanger. Interpretation of "true atomic resolution" images of graphite (0001) in noncontact atomic force microscopy. *Phys. Rev. B*, 62:6967–6970, 2000.
- [52] T. König, G. H. Simon, H.-P. Rust, and M. Heyde. Work Function Measurements of Thin Oxide Films on Metals-MgO on Ag(001). *J. Phys. Chem. C*, 113:11301–11305, 2009.
- [53] R. Eisenschitz and F. London. Über das Verhältnis der van der Waalsschen Kräfte zu den homöopolaren Bindungskräften. *Z. Physik*, 60:491–527, 1930.
- [54] A. Banerjea, J. R. Smith, and J. Ferrante. Universal aspects of adhesion and atomic force microscopy. *J. Phys.: Condens. Matter*, 2:8841–8846, 1990.
- [55] S. Ciraci, E. Tekman, A. Baratoff, and I. P. Batra. Theoretical study of short- and long-range forces and atom transfer in scanning force microscopy. *Phys. Rev. B*, 46:10411–10422, 1992.

- 
- [56] H. Hölscher and A. Schirmeisen. Dynamic Force Microscopy and Spectroscopy. *Adv. Imag. Electron. Phys.*, 135:41–101, 2005.
- [57] U. Dürig. Interaction sensing in dynamic force microscopy. *New J. Phys.*, 2:5, 2000.
- [58] H. Hölscher, B. Gotsmann, W. Allers, U. D. Schwarz, H. Fuchs, and R. Wiesendanger. Measurement of conservative and dissipative tip-sample interaction forces with a dynamic force microscope using the frequency modulation technique. *Phys. Rev. B*, 64:075402, 2001.
- [59] S. A. Ghasemi, S. Goedecker, A. Baratoff, T. Lenosky, E. Meyer, and H. J. Hug. Ubiquitous Mechanisms of Energy Dissipation in Noncontact Atomic Force Microscopy. *Phys. Rev. Lett.*, 100:236106, 2008.
- [60] F. J. Giessibl. Forces and frequency shifts in atomic-resolution dynamic-force microscopy. *Phys. Rev. B*, 56:16010–16015, 1997.
- [61] J. E. Sader and S. P. Jarvis. Accurate formulas for interaction force and energy in frequency modulation force spectroscopy. *Appl. Phys. Lett.*, 84:1801–1803, 2004.
- [62] U. Dürig. Relations between interaction force and frequency shift in large-amplitude dynamic force microscopy. *Appl. Phys. Lett.*, 75:433–435, 1999.
- [63] U. Dürig. Extracting interaction forces and complementary observables in dynamic probe microscopy. *Appl. Phys. Lett.*, 76:1203–1205, 2000.
- [64] F. J. Giessibl. A direct method to calculate tip-sample forces from frequency shifts in frequency-modulation atomic force microscopy. *Appl. Phys. Lett.*, 78:123–125, 2001.
- [65] O. Pfeiffer. *Quantitative dynamische Kraft- und Dissipationsmikroskopie auf molekularer Skala*. PhD thesis, 2004.
- [66] M. Abramowitz and I. A. Stegun. *Handbook of Mathematical Functions*. Dover, New York, 1975.
- [67] I. Giaever. Energy Gap in Superconductors Measured by Electron Tunneling. *Phys. Rev. Lett.*, 5:147–148, 1960.
- [68] J. Bardeen, L. N. Cooper, and J. R. Schrieffer. Theory of Superconductivity. *Phys. Rev.*, 108:1175–1204, 1957.

- [69] H. J. W. Zandvliet and A. van Houselt. Scanning Tunneling Spectroscopy. *Annu. Rev. Anal. Chem.*, 2:37–55, 2009.
- [70] J. Tersoff and D. R. Hamann. Theory and Application for the Scanning Tunneling Microscope. *Phys. Rev. Lett.*, 50:1998–2001, 1983.
- [71] C. J. Chen. Theory of scanning tunneling spectroscopy. *J. Vac. Sci. Technol. A*, 6:319–322, 1988.
- [72] V. A. Ukraintsev. Data evaluation technique for electron-tunneling spectroscopy. *Phys. Rev. B*, 53:11176–11185, 1996.
- [73] M. Passoni and C. E. Bottani. Transfer Hamiltonian analytical theory of scanning tunneling spectroscopy. *Phys. Rev. B*, 76:115404, 2007.
- [74] D. M. Eigler and E. K. Schweizer. Positioning single atoms with a scanning tunnelling microscope. *Nature*, 344:524–526, 1990.
- [75] K. Wandelt, W. Jacob, N. Memmel, and V. Dose. Inverse Photoemission of Adsorbed Xenon Multilayers on Ru(001): Refutation of Final-State Screening Effects. *Phys. Rev. Lett.*, 57:1643–1646, 1986.
- [76] X. Bouju, C. Joachim, C. Girard, and P. Sautet. Imaging and moving a xenon atom on a copper (110) surface with the tip of a scanning tunneling microscope: A theoretical study. *Phys. Rev. B*, 47:7454–7461, 1993.
- [77] D. M. Eigler, P. S. Weiss, E. K. Schweizer, and N. D. Lang. Imaging Xe with a low-temperature scanning tunneling microscope. *Phys. Rev. Lett.*, 66:1189–1192, 1991.
- [78] G. Doyen, D. Drakova, and M. Scheffler. Green-function theory of scanning tunneling microscopy: Tunnel current and current density for clean metal surfaces. *Phys. Rev. B*, 47:9778–9790, 1993.
- [79] G. Doyen, D. Drakova, J. V. Barth, R. Schuster, T. Gritsch, R. J. Behm, and G. Ertl. Scanning-tunneling-microscope imaging of clean and alkali-metal-covered Cu(110) and Au(110) surfaces. *Phys. Rev. B*, 48:1738–1749, 1993.
- [80] G. Doyen. *Scanning Tunneling Microscopy III*, volume 29 of *Springer Series in Surface Sciences*. Springer Berlin Heidelberg, 1993.

- [81] L. Bartels, G. Meyer, and K.-H. Rieder. Controlled vertical manipulation of single CO molecules with the scanning tunneling microscope: A route to chemical contrast. *Appl. Phys. Lett.*, 71:213–215, 1997.
- [82] J. A. Nieminen, E. Niemi, and K.-H. Rieder. Interference between competing tunneling channels and chemical resolution of STM. *Surf. Sci.*, 552:L47–L52, 2004.
- [83] T. N. Todorov, G. A. D. Briggs, and A. P. Sutton. Elastic quantum transport through small structures. *J. Phys.: Condens. Matter*, 5: 2389–2406, 1993.
- [84] J. B. Pendry, A. B. Pretre, and B. C. H. Krutzen. Theory of the scanning tunnelling microscope. *J. Phys.: Condens. Matter*, 3:4313–4321, 1991.
- [85] H. C. Galloway, P. Sautet, and M. Salmeron. Structure and contrast in scanning tunneling microscopy of oxides: FeO monolayer on Pt(111). *Phys. Rev. B*, 54:R11145–R11148, 1996.
- [86] L. Giordano, G. Pacchioni, J. Goniakowski, N. Nilius, E. D. L. Rienks, and H.-J. Freund. Interplay between structural, magnetic, and electronic properties in a FeO/Pt (111) ultrathin film. *Phys. Rev. B*, 76: 075416, 2007.
- [87] V. I. Anisimov, M. A. Korotin, and E. Z. Kurmaev. Band-structure description of Mott insulators (NiO, MnO, FeO, CoO). *J. Phys.: Condens. Matter*, 2:3973–3987, 1990.
- [88] E. D. L. Rienks, N. Nilius, H.-P. Rust, and H.-J. Freund. Surface potential of a polar oxide film: FeO on Pt(111). *Phys. Rev. B*, 71: 241404, 2005.
- [89] G. Kresse, M. Schmid, E. Napetschnig, M. S., L. Kohler, and P. Varga. Structure of the Ultrathin Aluminum Oxide Film on NiAl(110). *Science*, 308:1440–1442, 2005.
- [90] G. H. Simon, T. König, H.-P. Rust, M. Heyde, and H.-J. Freund. Atomic structure of the ultrathin alumina on NiAl(110) and its antiphase domain boundaries as seen by frequency modulation dynamic force microscopy. *New J. Phys.*, 11:093009, 2009.
- [91] W. Hebenstreit, J. Redinger, Z. Horozova, M. Schmid, R. Podlucky, and P. Varga. Atomic resolution by STM on ultra-thin films of alkali

- halides: experiment and local density calculations. *Surf. Sci.*, 424: L321–L328, 1999.
- [92] R. M. Feenstra. Tunneling spectroscopy of the (110) surface of direct-gap III-V semiconductors. *Phys. Rev. B*, 50:4561–4570, 1994.
- [93] S. Datta, W. Tian, S. Hong, R. Reifenberger, J. I. Henderson, and C. P. Kubiak. Current-Voltage Characteristics of Self-Assembled Monolayers by Scanning Tunneling Microscopy. *Phys. Rev. Lett.*, 79:2530–2533, 1997.
- [94] S. W. Wu, G. V. Nazin, X. Chen, X. H. Qiu, and W. Ho. Control of Relative Tunneling Rates in Single Molecule Bipolar Electron Transport. *Phys. Rev. Lett.*, 93:236802, 2004.
- [95] M. Sterrer, M. Heyde, M. Novicki, N. Nilius, T. Risse, H.P. Rust, G. Pacchioni, and H.-J. Freund. Identification of Color Centers on MgO(001) Thin Films with Scanning Tunneling Microscopy. *J. Phys. Chem. B*, 110:46–49, 2006.
- [96] G. Binnig and H. Rohrer. Scanning tunneling microscopy. *Helv. Phys. Acta*, 55:726–735, 1982.
- [97] K. H. Gundlach. Zur berechnung des tunnelstroms durch eine trapezförmige potentialstufe. *Solid-State Electronics*, 9:949–957, 1966.
- [98] H. M. Benia. *Spatially Resolved Optical Measurements on Supported Metal Particles and Oxide Surfaces with the STM*. PhD thesis, Berlin 2008.
- [99] O. Yu. Kolesnychenko, Yu. A. Kolesnichenko, O. I. Shklyarevskii, and H. van Kempen. Field-emission resonance measurements with mechanically controlled break junctions. *Physica B*, 291:246–255, 2000.
- [100] R. H. Fowler and L. Nordheim. Electron Emission in Intense Electric Fields. *Proc. R. Soc. Lond. A*, 119:173–181, 1928.
- [101] R. Gomer. *Field Emission and Field Ionization*. Harvard University Press, 1961.
- [102] M. Arita, K. Wakasugi, K. Ohta, K. Hamada, Y. Takahashi, and J.-B. Choi. Microstructure and electric property of MgO/Fe/MgO tri-layer films forming a nano-granular system. *Microelectron. Eng.*, 85:2445–2450, 2008.

- [103] I. Rungger, O. Mryasov, and S. Sanvito. Resonant electronic states and I-V curves of Fe/MgO/Fe(100) tunnel junctions. *Phys. Rev. B*, 79:094414, 2009.
- [104] S. Yuasa, T. Nagaham, A. Fukushima, Y. Suzuki, and K. Ando. Giant room-temperature magnetoresistance in single-crystal Fe/MgO/Fe magnetic tunnel junctions. *Nature Mater.*, 3:868–871, 2004.
- [105] P. L. J. Gunter, J. W. Niemantsverdriet, F. H. Ribeiro, and G. A. Somorjai. Surface Science Approach to Modeling Supported Catalysts. *Catal. Rev.-Sci. Eng.*, 39:77–168, 1997.
- [106] C. R. Henry. Surface studies of supported model catalysts. *Surf. Sci. Rep.*, 31:231–325, 1998.
- [107] H.-J. Freund. Clusters and islands on oxides: from catalysis via electronics and magnetism to optics. *Surf. Sci.*, 500:271–299, 2002.
- [108] A. Bongiorno and U. Landman. Water-Enhanced Catalysis of CO Oxidation on Free and Supported Gold Nanoclusters. *Phys. Rev. Lett.*, 95:106102, 2004.
- [109] M. S. Chen and D. W. Goodman. Ultrathin, ordered oxide films on metal surfaces. *J. Phys.: Condens. Matter*, 20:264013, 2008.
- [110] H.-J. Freund and G. Pacchioni. Oxide ultra-thin films on metals: new materials for the design of supported metal catalysts. *Chem. Soc. Rev.*, 37:2224–2242, 2008.
- [111] S. Siculo, L. Giordano, and G. Pacchioni. Adsorption of Late Transition Metal Atoms on MgO/Mo(100) and MgO/Ag(100) Ultrathin Films: A Comparative DFT Study. *J. Phys. Chem. C*, 113:16694, 2009.
- [112] N. Nilius. Properties of oxide thin films and their adsorption behavior studied by scanning tunneling microscopy and conductance spectroscopy. *Surf. Sci. Rep.*, 64:595–659, 2009.
- [113] G. Spoto, E. N. Gribov, G. Ricchiardi, A. Damin, D. Scarano, S. Bordiga, C. Lamberti, and A. Zecchina. Carbon monoxide MgO from dispersed solids to single crystals: a review and new advances. *Prog. Surf. Sci.*, 76:71–146, 2004.
- [114] L. N. Kantorovich, J. M. Holender, and M. J. Gillan. The energetics and electronic structure of defective and irregular surfaces on MgO. *Surf. Sci.*, 343:221–239, 1995.

- [115] R. Orlando, R. Millini, G. Perego, and R. Dovesi. Catalytic properties of F-centres at the magnesium oxide surface: hydrogen abstraction from methane. *J. Molec. Catal. A*, 119:253–262, 1997.
- [116] K. M. Neyman, C. Inntam, A. V. Matveev, V. A. Nasluzov, and N. Rösch. Single d-Metal Atoms on  $F_S$  and  $F_S^+$  Defects of MgO(001): A Theoretical Study across the Periodic Table. *J. Am. Chem. Soc.*, 127:11652–11660, 2005.
- [117] G. Pacchioni. Oxygen Vacancy: The Invisible Agent on Oxide Surfaces. *Chem. Phys. Chem.*, 4:1041–1047, 2003.
- [118] L. Giordano, U. Martinez, G. Pacchioni, M. Watkins, and A. L. Shluger. F and  $F^+$  Centers on MgO/Ag(100) or MgO/Mo(100) Ultrathin Films: Are They Stable? *J. Phys. Chem. C*, 112:3857–3865, 2008.
- [119] E. Giamello, M. C. Paganini, D. M. Murphy, A. M. Ferrari, and G. Pacchioni. A Combined EPR and Quantum Chemical Approach to the Structure of Surface  $F_s^+(H)$  Centers on MgO. *J. Phys. Chem. B*, 101:971–982, 1997.
- [120] M. Chiesa, E. Giamello, D. M. Murphy, G. Pacchioni, M. C. Paganini, R. Soave, and Z. Sojka. Reductive Activation of the Nitrogen Molecule at the Surface of Electron-Rich MgO and CaO. The  $N_2^-$  Surface Adsorbed Radical Ion. *J. Phys. Chem. B*, 105:497–505, 2001.
- [121] M. Sterrer, E. Fischbach, T. Risse, and H.-J. Freund. Geometric Characterization of a Singly Charged Oxygen Vacancy on a Single-Crystalline MgO(001) Film by Electron Paramagnetic Resonance Spectroscopy. *Phys. Rev. Lett.*, 94:186101, 2005.
- [122] M. Sterrer, E. Fischbach, M. Heyde, N. Nilius, H.-P. Rust, T. Risse, and H.-J. Freund. Electron Paramagnetic Resonance and Scanning Tunneling Microscopy Investigations on the Formation of  $F^+$  and  $F^0$  Color Centers on the Surface of Thin MgO(001) Films. *J. Phys. Chem. B*, 110:8665–8669, 2006.
- [123] M. Moseler, H. Häkkinen, and U. Landman. Supported Magnetic Nanoclusters: Soft Landing of Pd Clusters on a MgO Surface. *Phys. Rev. Lett.*, 89:176103, 2002.

- [124] L. Giordano, C. Di Valentin, J. Goniakowski, and G. Pacchioni. Nucleation of Pd Dimers at Defect Sites of the MgO(100) Surface. *Phys. Rev. Lett.*, 92:096105, 2004.
- [125] L. M. Molina and B. Hammer. The activity of the tetrahedral Au<sub>20</sub> cluster: charging and impurity effects. *J. Catal.*, 233:399–404, 2005.
- [126] B. Yoon, H. Häkkinen, U. Landman, A. S. Worz, J.-M. Antonietti, S. Abbet, K. Judai, and U. Heiz. Charging Effects on Bonding and Catalyzed Oxidation of CO on Au<sub>8</sub> Clusters on MgO. *Science*, 307:403–407, 2005.
- [127] S. Abbet, A. Sanchez, U. Heiz, W.-D. Schneider, A. M. Ferrari, G. Pacchioni, and N. Rösch. Acetylene Cyclotrimerization on Supported Size-Selected Pd<sub>n</sub> Clusters (1 ≤ n ≤ 30): One Atom Is Enough! *J. Am. Chem. Soc.*, 122:3453–3457, 2000.
- [128] J. Wang and B. Hammer. Oxidation state of oxide supported nanometric gold. *Top. Catal.*, 44:49–56, 2007.
- [129] L. Giordano, F. Cinquini, and G. Pacchioni. Tuning the surface metal work function by deposition of ultrathin oxide films: Density functional calculations. *Phys. Rev. B*, 73:045414, 2005.
- [130] S. Prada, U. Martinez, and G. Pacchioni. Work function changes induced by deposition of ultrathin dielectric films on metals: A theoretical analysis. *Phys. Rev. B*, 78:235423, 2008.
- [131] V. Simic-Milosevic, M. Heyde, N. Nilius, T. König, H.-P. Rust, M. Sterrer, T. Risse, H.-J. Freund, L. Giordano, and G. Pacchioni. Au Dimers on Thin MgO(001) Films: Flat and Charged or Upright and Neutral? *J. Am. Chem. Soc.*, 130:7814–7815, 2008.
- [132] B. Hallstedt. The Magnesium - Oxygen System. *CALPHAD*, 17:281–286, 1993.
- [133] L. S. Dubrovinski and S. K. Saxena. Thermal Expansion of Periclase (MgO) and Tungsten (W) to Melting Temperatures. *Phys. Chem. Min.*, 24:547–550, 1997.
- [134] P. Franke and D. Neuschütz. *Landolt-Börnstein - Group IV: Physical Chemistry*, volume 19B3, chapter Binary Systems. Part 3: Binary Systems from Cs-K to Mg-Zr. Springer Berlin Heidelberg, 2005.

- [135] B. Predel. *Landolt-Börnstein - Group IV: Physical Chemistry*, volume Volume 5H, chapter Mg-O (Magnesium-Oxygen). Springer-Verlag, 1997.
- [136] J. S. Corneille, J.-W. He, and D. W. Goodman. XPS characterization of ultra-thin MgO films on a Mo(100) surface. *Surf. Sci.*, 306:269–278, 1994.
- [137] Z. L. Wang, J. Bentley, E. A. Kenik, L. L. Horton, and R. A. McKee. In-situ formation of MgO<sub>2</sub> thin films on MgO single-crystal surfaces at high temperatures. *Surf. Sci.*, 273:88–108, 1992.
- [138] T. S. Duffy, R. J. Hemley, and H. K. Mao. Equation of State and Shear Strength at Multimegabar Pressures: Magnesium Oxide to 227 GPa. *Phys. Rev. Lett.*, 74:1371–1374, 1995.
- [139] V. E. Henrich. *The Chemical Physics of Solid Surfaces*, volume 9, chapter 1, pages 1–34. Elsevier, 2001.
- [140] E. Madelung. Das elektrische Feld in Systemen von regelmäßig angeordneten Punktladungen. *Physik. Zeitschr.*, 19:524–532, 1918.
- [141] Ch. Kittel. *Einführung in die Festkörperphysik*. R. Oldenbourg Verlag München Wien, 1988.
- [142] C. Noguera. *Physics and Chemistry at Oxide Surfaces*. Cambridge University Press, Cambridge, 1996.
- [143] P. P. Ewald. Die Berechnung optischer und elektrostatischer Gitterpotentiale. *Ann. Phys.*, 369:253–287, 1921.
- [144] J. Q. Broughton and P. S. Bagus. A study of madelung potential effects in the ESCA spectra of the metal oxides. *J. Electron Spectrosc. Relat. Phenom.*, 20:261–280, 1980.
- [145] V. E. Henrich and P. A. Cox. *The Surface Science of Metal Oxides*. Cambridge University Press, 1994.
- [146] C. Y. Fong, W. Saslow, and Marvin L. Cohen. Pseudopotential Calculation of the Optical Constants of MgO from 7-28 eV. *Phys. Rev.*, 168:992–999, 1968.
- [147] N. Daude, C. Jouanin, and C. Gout. Electronic band structure of magnesium and calcium oxides. *Phys. Rev. B*, 15:2399–2405, 1977.

- [148] C. Jun, L. Lin, T. Lu, and L. Yong. Electronic structure of F, F<sup>+</sup>-center in MgO. *Eur. Phys. J.*, 9:593–598, 1969.
- [149] S. Schintke, S. Messerli, M. Pivetta, F. Patthey, L. Libioulle, M. Stengel, A. De Vita, and W.-D. Schneider. Insulator at the Ultrathin Limit: MgO on Ag(001). *Phys. Rev. Lett.*, 87:276801, 2001.
- [150] D. Fritsch, H. Schmidt, and M. Grundmann. Pseudopotential band structures of rocksalt MgO, ZnO, and Mg<sub>1-x</sub>Zn<sub>x</sub>O. *Appl. Phys. Lett.*, 88:134104, 2006.
- [151] V. E. Henrich, G. Dresselhaus, and H. J. Zeiger. Energy-dependent electron-energy-loss spectroscopy: Application to the surface and bulk electronic structure of MgO. *Phys. Rev. B*, 22:4764–4775, 1980.
- [152] F. Didier and J. Jupille. Layer-by-layer growth mode of silver on magnesium oxide (100). *Surf. Sci.*, 307-309:587–590, 1994.
- [153] P. W. Tasker. The stability of ionic crystal surfaces. *J. Phys. C: Solid State Phys.*, 12:4977–4984, 1979.
- [154] C. Palache, H. Berman, and C. Frondel. *Dana's System of Mineralogy*. Wiley, New York, 1944.
- [155] O. Robach, G. Renaud, and A. Barbier. Very-high-quality MgO(001) surfaces: roughness, rumpling and relaxation. *Surf. Sci.*, 401:227–235, 1998.
- [156] M.-Ch. Wu, J. S. Corneille, C. A. Estrada, J.-W. He, and D. W. Goodman. Synthesis and characterization of ultra-thin MgO films on Mo(100). *Chem. Phys. Lett.*, 182:472–478, 1991.
- [157] P. Blöchl, G. P. Das, H. F. Fischmeister, and U. Schönberger. Electronic Structure of a Metal-Ceramic Interface: Ab Initio Calculations for MgO/Ag. Proc. of the Conf. on "Bonding, Structure and Mechanical Properties of Metal-Ceramic Interfaces", Santa Barbara, 1989.
- [158] J. Wollschläger, D. Erdös, and K. M. Schröder. The formation of mosaics during the reactive growth of MgO films on Ag(100). *Surf. Sci.*, 402-404:272–276, 1998.
- [159] S. A. Chambers, Y. Gao, and Y. Liang. The early stages of MgO epitaxy on lattice-matched Cr<sub>0.7</sub>Mo<sub>0.3</sub>(001). *Surf. Sci.*, 339:297–309, 1995.

- 
- [160] S. Benedetti, P. Torelli, S. Valeri, H. M. Benia, N. Nilius, and G. Renaud. Structure and morphology of thin MgO films on Mo(001). *Phys. Rev. B*, 78:195411, 2008.
- [161] G. Butti, M. I. Trioni, and H. Ishida. Electronic properties calculation of MgO thin films adsorbed on semi-infinite Ag(001). *Phys. Rev. B*, 70:195425, 2004.
- [162] M. Sgroi, C. Pisani, and M. Busso. Ab initio density functional simulation of structural and electronic properties of MgO ultra-thin adlayers on the (001) Ag surface. *Thin Solid Films*, 400:64–70, 2001.
- [163] C. Giovanardi, A. di Bona, T. S. Moia, S. Valeri, C. Pisani, M. Sgroi, and M. Busso. Experimental and theoretical study of the MgO/Ag(001) interface. *Surf. Sci.*, 505:L209–L214, 2002.
- [164] R. Smoluchowski. Anisotropy of the Electronic Work Function of Metals. *Phys. Rev.*, 60:661–674, 1941.
- [165] URL [www.webelements.com](http://www.webelements.com).
- [166] N. Lopez and S. Valeri. MgO/Ag(001) interface structure and STM images from first principles. *Phys. Rev. B*, 70:125428, 2004.
- [167] A. M. Flank, R. Delaunay, P. Lagarde, M. Pompa, and J. Jupille. Epitaxial silver layer at the MgO(100) surface. *Phys. Rev. B*, 53:R1737–R1739, 1996.
- [168] S. Altieri, L. H. Tjeng, and G. A. Sawatzky. Electronic structure and chemical reactivity of oxide-metal interfaces: MgO(100)/Ag(100). *Phys. Rev. B*, 61:16948–16955, 2000.
- [169] M. W. Finnis. The theory of metal - ceramic interfaces. *J. Phys.: Condens. Matter*, 8:5811–5836, 1996.
- [170] G. Bordier and C. Noguera. Electronic structure of a metal-insulator interface: Towards a theory of nonreactive adhesion. *Phys. Rev. B*, 44:6361–6371, 1991.
- [171] A. V. Matveev, K. M. Neyman, I. V. Yudanov, and N. Rösch. Adsorption of transition metal atoms on oxygen vacancies and regular sites of the MgO(001) surface. *Surf. Sci.*, 426:123–139, 1999.

- [172] G. Pacchioni. Quantum Chemistry of Oxide Surfaces: From CO Chemisorption to the Identification of the Structure and Nature of Point Defects on MgO. *Surf. Rev. Lett.*, 7:277–306, 2000.
- [173] Z. Yan, S. Chinta, A. A. Mohamed, J. P. Fackler, and D. W. Goodman. The Role of F-Centers in Catalysis by Au Supported on MgO. *J. Am. Chem. Soc.*, 127:1604–1605, 2005.
- [174] G. Barcaro, M. Causa, and A. Fortunelli. A comparison between the absorption properties of the regular and  $F_S$ -defected MgO (100) surface. *Theor. Chem. Acc.*, 118:807–812, 2007.
- [175] A. Sanchez, S. Abbet, U. Heiz, W.-D. Schneider, H. Häkkinen, R. N. Barnett, and U. Landman. When Gold Is Not Noble: Nanoscale Gold Catalysts. *J. Phys. Chem. A*, 103:9573–9578, 1999.
- [176] S. Abbet, E. Riedo, H. Brune, U. Heiz, A. M. Ferrari, L. Giordano, and G. Pacchioni. Identification of Defect Sites on MgO(100) Thin Films by Decoration with Pd Atoms and Studying CO Adsorption Properties. *J. Am. Chem. Soc.*, 123:6172–6178, 2001.
- [177] A. V. Matveev, K. M. Neyman, I. V. Yudanov, and N. Rösch. Adsorption of transition metal atoms on oxygen vacancies and regular sites of the MgO(001) surface. *Surf. Sci.*, 426:123–139, 1999.
- [178] K. M. Neyman, C. Inntam, V. A. Nasluzov, R. Kosarev, and N. Rösch. Adsorption of d-metal atoms on the regular MgO(001) surface: Density functional study of cluster models embedded in an elastic polarizable environment. *Appl. Phys. A*, 78:823–828, 2004.
- [179] G. Pacchioni and P. Pescarmona. Structure and stability of oxygen vacancies on sub-surface, terraces, and low-coordinated surface sites of MgO: an ab initio study. *Surf. Sci.*, 412-413:657–671, 1998.
- [180] P. V. Sushko, A. L. Shluger, and C. R. A. Catlow. Relative energies of surface and defect states: ab initio calculations for the MgO (001) surface. *Surf. Sci.*, 450:153 – 170, 2000.
- [181] A. M. Ferrari and G. Pacchioni. Electronic Structure of F and V Centers on the MgO Surface. *J. Phys. Chem.*, 99:17010–17018, 1995.
- [182] E. Scorza, U. Birkenheuer, and C. Pisani. The oxygen vacancy at the surface and in bulk MgO: An embedded-cluster study. *J. Chem. Phys.*, 107:9645–9658, 1997.

- [183] D. Ricci, G. Pacchioni, P. V. Sushko, and A. L. Shluger. Electron trapping at neutral divacancy sites on the MgO surface. *J. Chem. Phys.*, 117:2844–2851, 2002.
- [184] L. Ojamäe and C. Pisani. Theoretical characterization of divacancies at the surface and in bulk MgO. *J. Chem. Phys.*, 109:10984–10995, 1998.
- [185] A. M. Ferrari and G. Pacchioni. Surface reactivity of MgO oxygen vacancies: electrostatic mechanisms in the formation of  $O_2^-$  and  $CO^-$  species. *J. Chem. Phys.*, 107:2066–2078, 1997.
- [186] P. V. Sushko, J. L. Gavartin, and A. L. Shluger. Electronic Properties of Structural Defects at the MgO (001) Surface. *J. Phys. Chem. B*, 106:2269–2276, 2002.
- [187] A. I. Popov, E. A. Kotomin, and M. M. Kuklja. Quantum chemical calculations of the electron center diffusion in MgO crystals. *Phys. Stat. Sol. (b)*, 195:61–66, 1996.
- [188] A. De Vita, M. J. Gillan, J. S. Lin, M. C. Payne, I. Stich, and L. J. Clarke. Defect energetics in MgO treated by first-principles methods. *Phys. Rev. B*, 46:12964–12973, 1992.
- [189] D. J. Harris, G. W. Watson, and S. C. Parker. Vacancy migration at the 410/[001] symmetric tilt grain boundary of MgO: An atomistic simulation study. *Phys. Rev. B*, 56:11477–11484, 1997.
- [190] M. M. Abraham, Y. Chen, and W. P. Unruh. Formation and stability of  $V^-$  and  $V_{Al}$  centers in MgO. *Phys. Rev. B*, 9:1842–1852, 1974.
- [191] P. R. Underhill and T. E. Gallon. The surface defect peak in the electron energy loss spectrum of MgO (100). *Solid State Communications*, 43:9–11, 1982.
- [192] M. J. Norgett, A. M. Stoneham, and A. P. Pathak. Electronic structure of the V- centre in MgO. *J. Phys. C: Solid State Phys.*, 10:555–565, 1977.
- [193] Y. Chen and M. M. Abraham. Trapped-hole centers in alkaline-earth oxides. *J. Phys. Chem. Solids*, 51:747–764, 1990.
- [194] A. Gibson, R. Haydock, and J. P. LaFemina. Stability of vacancy defects in MgO: The role of charge neutrality. *Phys. Rev. B*, 50:2582–2592, 1994.

- [195] P. Baranek, G. Pinarello, C. Pisani, and R. Dovesi. Ab initio study of the cation vacancy at the surface and in bulk MgO. *Phys. Chem. Chem. Phys.*, 2:3893–3901, 2000.
- [196] private communication with G. Pacchioni.
- [197] M.-Ch. Wu, Ch. M. Truong, and D. W. Goodman. Electron-energy-loss-spectroscopy studies of thermally generated defects in pure and lithium-doped MgO(100) films on Mo(100). *Phys. Rev. B*, 46:12688–12694, 1992.
- [198] J. Kramer, W. Ernst, C. Tegenkamp, and H. Pfnür. Mechanism and kinetics of color center formation on epitaxial thin films of MgO. *Surf. Sci.*, 517:87–97, 2002.
- [199] C. Sousa, G. Pacchioni, and F. Illas. Ab initio study of the optical transitions of F centers at low-coordinated sites of the MgO surface. *Surf. Sci.*, 429:217–228, 1999.
- [200] D. Peterka, C. Tegenkamp, K. M. Schröder, W. Ernst, and H. Pfnür. Oxygen surplus and oxygen vacancies on the surface of epitaxial MgO layers grown on Ag(100). *Surf. Sci.*, 431:146–155, 1999.
- [201] Y. Chen, R. T. Williams, and W. A. Sibley. Defect Cluster Centers in MgO. *Phys. Rev.*, 182:960–964, 1969.
- [202] D. Domínguez-Ariza, C. Sousa, F. Illas, D. Ricci, and G. Pacchioni. Ground- and excited-state properties of M-center oxygen vacancy aggregates in the bulk and surface of MgO. *Phys. Rev. B*, 68:054101, 2003.
- [203] V. Zielasek, T. Hildebrandt, and M. Henzler. Surface color centers on epitaxial NaCl films. *Phys. Rev. B*, 62:2912–2919, 2000.
- [204] M. L. Knotek and P. J. Feibelman. Ion Desorption by Core-Hole Auger Decay. *Phys. Rev. Lett.*, 40:964–967, 1978.
- [205] M. L. Knotek and P. J. Feibelman. Stability of ionically bonded surfaces in ionizing environments. *Surf. Sci.*, 90:78 – 90, 1979.
- [206] P. E. Trevisanutto, P. V. Sushko, A. L. Shluger, K. M. Beck, M. Henyk, A. G. Joly, and W. P. Hess. A mechanism of photo-induced desorption of oxygen atoms from MgO nano-crystals. *Surf. Sci.*, 593:210–220, 2005.

- [207] C. S. A. Fang. Surface structural transition of adsorption of oxygen on Ag(100). *Surf. Sci.*, 235:L291 – L294, 1990.
- [208] G. Ertl, H. Knözinger, F. Schüth, and J. Weitkamp, editors. *Handbook of heterogeneous catalysis*, volume 2. 2008.
- [209] H.-J. Freund and M. W. Roberts. Surface chemistry of carbon dioxide. *Surf. Sci. Rep.*, 37:225–273, 1996.
- [210] G. Pacchioni, L. Giordano, and M. Baistrocchi. Charging of Metal Atoms on Ultrathin MgO/Mo(100) Films. *Phys. Rev. Lett.*, 94:226104, 2005.
- [211] D. Ricci, A. Bongiorno, G. Pacchioni, and U. Landman. Bonding Trends and Dimensionality Crossover of Gold Nanoclusters on Metal-Supported MgO Thin Films. *Phys. Rev. Lett.*, 97:036106, 2006.
- [212] P. Frondelius, H. Häkkinen, and K. Honkala. Adsorption of small Au clusters on MgO and MgO/Mo: the role of oxygen vacancies and the Mo-support. *New J. Phys.*, 9:339, 2007.
- [213] P. Frondelius, A. Hellman, K. Honkala, H. Häkkinen, and H. Grönbeck. Charging of atoms, clusters, and molecules on metal-supported oxides: A general and long-ranged phenomenon. *Phys. Rev. B*, 78:085426, 2008.
- [214] L. Giordano and G. Pacchioni. Charge transfer at metal/oxide interfaces: a DFT study of formation of  $K^{\delta+}$  and  $Au^{\delta-}$  species on MgO/Ag(001) ultra-thin films from deposition of neutral atoms. *Phys. Chem. Chem. Phys.*, 8:3335–3341, 2006.
- [215] M. Haruta, T. Kobayashi, H. Sano, and N. Yamada. Novel Gold Catalysts for the Oxidation of Carbon Monoxide at a Temperature far Below 0°C. *Chem. Lett.*, 16:405–408, 1987.
- [216] M. Haruta. Size- and support-dependency in the catalysis of gold. *Catal. Today*, 36:153–166, 1997.
- [217] H. Grönbeck. Mechanism for NO<sub>2</sub> Charging on Metal Supported MgO. *J. Phys. Chem. B*, 110:11977–11981, 2006.
- [218] G. A. Somorjai. *Introduction to Surface Chemistry and Catalysis*. John Wiley & Sons, Inc., 1994.
- [219] G. Binnig and H. Rohrer. Scanning tunneling microscopy. *Surf. Sci.*, 126:236–244, 1983.

- [220] N. D. Lang. Apparent barrier height in scanning tunneling microscopy. *Phys. Rev. B*, 37:10395–10398, 1988.
- [221] F. E. Olsson, M. Persson, J. Repp, and G. Meyer. Scanning tunneling microscopy and spectroscopy of NaCl overlayers on the stepped Cu(311) surface: Experimental and theoretical study. *Phys. Rev. B*, 71:075419, 2005.
- [222] L. Olesen, M. Brandbyge, M. R. Sørensen, K. W. Jacobsen, E. Lægsgaard, I. Stensgaard, and F. Besenbacher. Apparent Barrier Height in Scanning Tunneling Microscopy Revisited. *Phys. Rev. Lett.*, 76:1485–1488, 1996.
- [223] J. P. Perdew, J. A. Chevary, S. H. Vosko, K. A. Jackson, M. R. Pederson, D. J. Singh, and C. Fiolhais. Atoms, molecules, solids, and surfaces: Applications of the generalized gradient approximation for exchange and correlation. *Phys. Rev. B*, 46:6671–6687, 1992.
- [224] G. Kresse and J. Hafner. Ab initio molecular dynamics for liquid metals. *Phys. Rev. B*, 47:R558–R561, 1993.
- [225] G. Kresse and J. Furthmüller. Efficient iterative schemes for ab initio total-energy calculations using a plane-wave basis set. *Phys. Rev. B*, 54:11169–11186, 1996.
- [226] P. E. Blöchl. Projector augmented-wave method. *Phys. Rev. B*, 50:17953–17979, 1994.
- [227] M. Chelvayohan and C. H. B. Mee. Work function measurements on (110), (100) and (111) surfaces of silver. *J. Phys. C: Solid State Phys.*, 15:2305–2312, 1982.
- [228] L. Gross, F. Mohn, P. Liljeroth, J. Repp, F. J. Giessibl, and G. Meyer. Measuring the Charge State of an Adatom with Noncontact Atomic Force Microscopy. *Science*, 324:1428–1431, 2009.
- [229] F. Napoli, M. Chiesa, E. Giamello, E. Finazzi, C. Di Valentin, and G. Pacchioni. Partially Hydroxylated Polycrystalline Ionic Oxides: A New Route toward Electron-Rich Surfaces. *J. Am. Chem. Soc.*, 129:10575–10581, 2007.
- [230] C. Barth and C. R. Henry. Atomic Resolution Imaging of the (001) Surface of UHV Cleaved MgO by Dynamic Scanning Force Microscopy. *Phys. Rev. Lett.*, 91:196102, 2003.

- 
- [231] T. Trevethan and A. Shluger. Controlling electron transfer processes on insulating surfaces with the non-contact atomic force microscope. *Nanotechnology*, 20:264019, 2009.
- [232] *CRC Handbook of Chemistry and Physics*. CRC Press, 88th ed. edition, Boca Raton 2008.
- [233] N. Pontius, P. S. Betchold, N. Neeb, and W. Eberhardt. Femtosecond multi-photon photoemission of small transition metal cluster anions. *J. Electron Spectrosc. Relat. Phenom.*, 106:107, 2000.



# Appendix A

## Abbreviations

Abbreviation	Explanation
AES	auger electron spectroscopy
AFM	atomic force microscopy
CPD	contact potential difference
DB	diffusion barrier
DFM	dynamic force microscopy
DFT	density functional theory
ESD	electron stimulated desorption
EXAFS	extended x-ray-absorption fine structure
fcc	face centered cubic
FM-DFM	frequency modulation dynamic force microscopy
hcp	hexagonal closed packed
HREELS	high resolution electron energy loss spectroscopy
IE	ionization energy
LDA	local density approximation
LDOS	local density of states
LEED	low energy electron diffraction
LMTO	linearized muffin-tin orbital (theory)
MIGS	metal induced gap states
ML	monolayer
NC-AFM	noncontact-atomic force microscopy
STM	scanning tunneling microscopy
STS	scanning tunneling spectroscopy
TPD	temperature programmed desorption

UHV	ultrahigh vacuum
UPS	ultraviolet photoelectron spectroscopy
XPS	x-ray photoelectron spectroscopy

# Appendix B

## Publications and Conference Contributions

### Book contribution

Co-Author in: Noncontact Atomic Force Microscopy, Volume 2, Chapter 7, 143-167, Springer, 2009.

Study of Thin-Oxide Films with NC-AFM: Atomically Resolved Imaging and Beyond.

### Publications

1. T. König, G. H. Simon, L. Lichtenstein, L. Heinke, M. Heyde, H.-J. Freund.  
Electrostatic Forces in Dynamic Force Microscopy - Analysis of Electronic Surface Properties.  
To be submitted.
2. T. König, G. H. Simon, U. Martinez, L. Giordano, G. Pacchioni, M. Heyde, H.-J. Freund.  
Direct Measurement of the Attractive Interaction Forces on  $F^0$  Color Centers on MgO(001) by Dynamic Force Microscopy.  
ACS Nano, 4, 2510, 2010.
3. L. Heinke, L. Lichtenstein, G. H. Simon, T. König, M. Heyde, H.-J. Freund.  
Local Work Function Differences at Line Defects on Aluminium Oxide

---

on NiAl(110).

Accepted by Chem. Phys. Chem.

4. G.H. Simon, T. König, H.-P. Rust, M. V. Ganduglia-Pirovano, J. Sauer, M. Heyde, H.-J. Freund.  
Imaging of Individual Ad-Atoms on Oxide Surfaces by Dynamic Force Microscopy.  
Phys. Rev. B, 81, 073411, 2010.
5. T. König, G. H. Simon, H.-P. Rust, G. Pacchioni, M. Heyde, H.-J. Freund.  
Measuring the Charge State of Point Defects on MgO/Ag(001).  
J. Am. Chem. Soc., 131, 17544, 2009.
6. H.-P. Rust, T. König, G. H. Simon, M. Nowicki, V. Simic-Milosevic, G. Thielsch, M. Heyde, H.-J. Freund.  
A portable microevaporator for low temperature single atom studies by scanning tunneling and dynamic force microscopy.  
Rev. Sci. Instr., 80, 113705, 2009.
7. G. H. Simon, T. König, H.-P. Rust, M. Heyde, H.-J. Freund .  
Atomic Structure of the Ultrathin Alumina on NiAl(110) and its Antiphase Domain Boundaries as seen by Frequency Modulation Dynamic Force Microscopy.  
New J. Phys., 11, 093009, 2009.
8. T. König, G. H. Simon, H.-P. Rust, M. Heyde.  
Atomic Resolution on a Metal Single Crystal with Dynamic Force Microscopy.  
Appl. Phys. Lett., 95, 083116, 2009.
9. T. König, G. H. Simon, H.-P. Rust, M. Heyde.  
Work Function Measurements of Thin Oxide Films on Metals - MgO on Ag(001).  
J. Phys. Chem. C, 113, 11301, 2009.
10. V. Simic-Milosevic, M. Heyde, X. Lin, T. König, H.-P. Rust, M. Sterrer, T. Risse, N. Nilius, H.-J. Freund, L. Giordano, G. Pacchioni.  
Charge-induced formation of linear Au clusters on thin MgO films: Scanning tunneling microscopy and density-functional theory study.  
Phys. Rev. B, 78, 235429, 2008.

11. T. König, G. H. Simon, K.-H. Rieder, H.-P. Rust, M. Heyde.  
Superlattice structure of an Ar monolayer on Ag(111) observed by low-temperature scanning tunneling microscopy.  
Phys. Rev. B, 78, 201407, 2008.
12. G. H. Simon, T. König, M. Kulawik, H.-P. Rust, M. Heyde, H.-J. Freund.  
Atomically resolved force microscopy images of complex surface unit cells: Ultrathin alumina film on NiAl(110).  
Phys. Rev. B, 78, 113401, 2008.
13. K. Kinoshita, G. H. Simon, T. König, M. Heyde, H.-J. Freund, Y. Nakagawa, S. Suzuki, W.-J. Chun, S. T. Oyama, S. Otani, K. Asakura.  
A Scanning Tunneling Microscopy Observation of  $(\sqrt{3} \times \sqrt{3})$  R30° Reconstructed Ni<sub>2</sub>P (0001).  
Jpn. J. Appl. Phys., 47, 6088, 2008.
14. V. Simic-Milosevic, M. Heyde, N. Nilius, T. König, H.-P. Rust, M. Sterrer, T. Risse, H.-J. Freund, L. Giordano, G. Pacchioni.  
Au Dimers on Thin MgO(001) Films: Flat and Charged or Upright and Neutral?.  
J. Am. Chem. Soc., 130, 7814, 2008.

## Conference Contributions

1. T. König, G. H. Simon, H.-P. Rust, G. Pacchioni, M. Heyde, H.-J. Freund  
Point-Defect Characterisation and Identification on MgO/Ag(001) Studied by a Dual Mode FM-DFM/STM.  
International Workshop on Oxide Surfaces, (IWOX), Echigo-Yuzawa, Japan, 2010.
2. T. König, G. H. Simon, M. Heyde, H.-J. Freund.  
Work Function Determination of Different MgO Film Thicknesses Grown on Ag(001).  
International Conference on Nanoscience + Technology, (ICN+T), Keystone, Colorado, USA, 2008.
3. T. König, G. H. Simon, K.-H. Rieder, H.-P. Rust, M. Heyde, H.-J. Freund.  
Superlattice Structure of an Ar-monolayer Absorbed on Ag(111) Investigated by LT-STM.

- International Conference on Nanoscience + Technology, (ICN+T), Keystone, Colorado, USA, 2008.
4. T. König, G. H. Simon, H.-P. Rust, M. Heyde, H.-J. Freund.  
Dynamic Force and Scanning Tunneling Microscope investigations on Thin Oxide Films in Ultrahigh Vacuum at 5K.  
Center for Research on Interface Structures and Phenomena, CRISP, Yale University, New Haven, Connecticut, USA, 2008.
  5. T. König, G. H. Simon, M. Heyde, H.-J. Freund.  
Work function measurements with a combined AFM/STM setup under ultrahigh vacuum conditions at 5K on thin MgO films grown on Ag(001).  
Frühjahrstagung der Deutschen Physikalischen Gesellschaft, Berlin, Germany, 2008.
  6. T. König, G. H. Simon, M. Heyde, H.-J. Freund.  
Work function measurements of different MgO film thicknesses grown on Ag(001).  
Hauptversammlung der Deutschen Bunsen-Gesellschaft für Physikalische Chemie, (Bunsentagung), Saarbrücken, Germany, 2008.
  7. T. König, G. H. Simon, K.-H. Rieder, M. Heyde.  
Argon adsorbed on Ag(111).  
Frühjahrstagung der Deutschen Physikalischen Gesellschaft, Regensburg, Germany, 2007.

# Danksagung

Mein besonderer Dank gilt Herrn Professor Dr. Hans-Joachim Freund für die interessanten Forschungsprojekte, die hervorragenden Arbeitsbedingungen und für seine Zeit für Erklärungen und Diskussionen. Danke.

Herrn Professor Dr. Gianfranco Pacchioni möchte ich ganz herzlich danken für die Unterstützung dieser Arbeit durch DFT-Berechnungen und viele aufschlussreiche Diskussionen, sowie für seine schnellen Bearbeitungen unserer gemeinsamen Projekte. Danke.

Mein weiterer Dank gilt Herrn Professor Dr. Christian Thomsen für die Betreuung der Arbeit seitens der Technischen Universität Berlin. Danke.

Herrn Dr. Markus Heyde möchte ich ganz besonders danken für die Unterstützung der Arbeit, die freundschaftliche Arbeitsweise, die zahlreichen interessanten Diskussionen und seine stetige Hilfe bei allen Problemen. Danke.

Bei Herrn Dr. Hans-Peter Rust möchte ich mich für die schöne gemeinsame Zeit am FHI bedanken. Mit seinen Beiträgen hat er die Arbeit stets erleichtert und vorangebracht. Danke.

Herrn Dr. Martin Sterrer möchte ich für viele interessante Diskussionen und Hinweise danken. Danke.

Bedanken möchte ich mich auch bei meinen Kollegen aus der Arbeitsgruppe. Durch ihre Kollegialität wurden viele Ergebnisse erst ermöglicht. Danke.

Ein Dank geht auch an das Elektroniklabor und die Feinmechanikwerkstatt für die schnellen und präzisen Anfertigungen von Elektronikern und Bauteilen. Besonders danken möchte ich Herrn Klaus-Peter Vogelgesang für die akkuraten und schnellen Arbeiten. Danke.

Frau Misch und Frau Mehnert möchte ich für die perfekte Organisation von vielen Abläufen danken. Danke.

Bedanken möchte ich mich auch bei allen anderen Kollegen für das ausgezeichnete Arbeitsklima und ihren FHI-Spirit. Danke.

Ein besonderer Dank geht an Frau Marlies Hutten, für Ihre sprachlichen Anregungen und Vorschläge zu dieser Arbeit. Danke.

Ein riesengroßes Dankeschön geht an meine Familie, die es mir durch ihre Unterstützung erst ermöglicht hat, das Studium und die anschließende Doktorarbeit durchzuführen. Ganz besonders danken möchte ich Katrin, meinen Eltern Mechthild und Reinhard sowie Ruth und Christoph. Danke.

# Selbständigkeitserklärung

Hiermit erkläre ich, die vorliegende Arbeit selbständig ohne fremde Hilfe verfaßt und nur die angegebene Literatur und Hilfsmittel verwendet zu haben.

Thomas König  
Berlin, den